Investigations of the VMM readout chip for Micromegas Detectors of the ATLAS New Small Wheel Upgrade

Untersuchungen des VMM Auslesechips für Micromegas Detektoren des ATLAS New Small Wheel Upgrades

Masterarbeit an der Fakultät für Physik
der
Ludwig-Maximilians-Universität München

vorgelegt von
Maximilian Paul Rinnagel
geboren in München

München, den 08.05.2019

Gutachter: Prof. Dr. Otmar Biebel

Abstract

Modern micropattern gaseous detectors with their highly segmented anodes achieve spatial resolutions close to that of silicon detectors and become thus of great interest for particle physics experiments. Micromegas (MICROMEsh GAseous Structures) detectors are foreseen as precision trackers for the upgrade of the forward muon spectrometer of the ATLAS detector, the New Small Wheel (NSW). The huge number of readout strips and the accordingly rising background rate due to the steadily increasing luminosity of LHC require new readout electronics for these detectors.

The aim of this master thesis was to study the new VMM front-end readout chip, which was designed and produced in the scope of the ATLAS New Small Wheel Upgrade. The chip is digitally recording the charge and timing information of a particle interacting in the detector. The readout frequency required for the high luminosity upgrade of LHC will be reached by this chip.

With a 10x10 cm^2 Micromegas detector equipped with a preliminary version of the VMM chip, studies were conducted on pulse height, cluster multiplicity, and angular resolution using 22 MeV protons at the Tandem accelerator facility in Garching. The detector was hereby tilted to an angle of incidence of $(21 \pm 1)^\circ$. Pulse height and cluster multiplicity behaved very close to the prediction following Townsend's theory and the transverse diffusion. The incindence angle could be reconstructed with an angular resolution of $(^{+6^\circ}_{-4^\circ})$.

A large SM2 Micromegas module built by the German consortium was used for performance tests at CERN. Measured efficiencies and spatial resolutions were excellent using high-energy beams of 20-150 GeV muons (rate: $\mathcal{O}(Hz/cm^2)$) and pions (rate: $\mathcal{O}(kHz/cm^2)$) of the pre-accelerator SPS. These tests were performed in dependence of the configuration settings of the readout chip, the Ar:CO_2 gas mixtures (93:7 vol%, 85:15 vol%, 70:30 vol%) and the angle of incidence of the detector.

A more sophisticated position determination follows the idea of the time projection chamber (TPC). Using the drift time information of the electrons from ionization by muons or pions allows for reconstructing the track of the charged particles passing through the detector in case of tilted incidence angle. For this so called μTPC method this thesis will present first results using the new VMM electronics.

Tests of different Ar:CO_2 gas mixtures have been performed during the CERN test beam as well. A higher signal strength of ($\sim$ 10%) can be achieved for an increased proportion of the quenching gas CO_2. In general the detectors seem to be more stable against discharges at higher ratios of quenching gas.

For perpendicular tracks with a gas mixture of Ar:CO_2 93:7 vol% the best measured resolutions and efficiencies were $(116 \pm 2)\,\mu$m at (89 ± 0.2) % for the combined resolution of the two Stereo layers as well as $(135 \pm 3)\,\mu$m at (93.5 ± 0.1)% for the Eta_{Out} layer. These resolutions have been measured using three reference detectors with VMM electronics. Alternatively, the measurement using APV25 electronics equipped tracking detectors shows resolutions of $(110 \pm 12)\,\mu$m for Stereo and $(111 \pm 6)\,\mu$m for Eta_{Out}. As the reference detectors equipped with the well known APV25 electronics, used so far for the readout of Micromegas detectors, were resolving in two dimensions, rotation and tilt of the Micromegas under test could be corrected during the alignment of the detectors. Thus, the resolution in this experiment was further improved.

Kurzfassung

Moderne mikrostrukturierte Gasdetektoren mit ihrer stark segementierten Anodenstruktur erzielen eine Ortsauflösung nahe derer von Siliziumdetektoren und sind deshalb von großem Interesse für Teilchenphysikexperimente. Micromegas (MICROMEsh GAseous STRuctures) Detektoren sollen als Präzisonspurdetektor für das Upgrade des Myonspektrometers des ATLAS Detektors, das New Small Wheel (NSW), eingesetzt werden.

Das Ziel dieser Masterarbeit waren Studien mit dem VMM Auslesechip, welcher im Zuge des ATLAS New Small Wheel Upgrades entwickelt und produziert wurde. Die Besonderheit des Chips ist die vollständige digitale Auslese der Ladungs-und Zeitinformation eines den Detektor passierenden Teilchens. Die notwendige Ausleserate für das LHC Upgrade auf höhere Luminositäten wird der Chip erreichen.

Mit einem 10x10 cm^2 Micromegas Prototypen und einer vorläufigen Version des VMM Chips wurden Studien zur Pulshöhe, Clustermultiplizität und Winkelrekonstruktion am Tandem Beschleuniger in Garching mit 22 MeV Protonen bei einem Einfallswinkel von $(21 \pm 1)^\circ$ durchgeführt.

Das Ergebnis für die Pulshöhen und die Clustermultiplizität waren ein mit dem Townsend-Modell übereinstimmendes exponentielles Wachstum der Pulshöhe sowie die durch transversale Diffusion beeinflusste Clustermultiplizität. Der Winkel konnte mit einer Winkelauflösung von $(^{+6^\circ}_{-4^\circ})$ bestimmt werden.

Mit einem großflächigen, aus Kooperation deutscher Universitäten gebauten, SM2 Micromegas Modul und der fast endgültigen Version des VMMs konnten bei Funktionstests herrvoragende Effizienzen und Auflösungen unter Bestrahlung mit einem 20-150 GeV energiereichen Strahl von Myonen (Rate: $\mathcal{O}(\mathrm{Hz/cm^2})$) und Pionen (Rate: $\mathcal{O}(\mathrm{kHz/cm^2})$) des Beschleunigers SPS am CERN bestimmt werden.

Diese Tests wurden in Abhängigkeit der Einstellungen des Auslesechips, der Ar:CO$_2$ Gasmischungen (93:7 vol%, 85:15 vol%, 70:30 vol%) im Detektor sowie des Einfallswinkels der Teilchen in den Detektor durchgeführt.

Eine anspruchsvollere Rekonstruktionsmethode für die Teilchenposition liefert die μTPC Methode, welche dem Funktionsprinzip der Spurendriftkammer folgt. Die Driftzeitinformation der Elektronen, entstanden durch die Ionisation von Myonen/Pionen, erlaubt die Rekonstruktion der Spur eines geladenen Teilchens für den Fall einer schrägen Spur im Detektor. In dieser Arbeit werden erste Resultate für die μTPC Methode mit der neuen VMM Elektronik beschrieben.

Desweiteren wurden am CERN Studien zu unterschiedlichen Ar:CO$_2$ Messungen durchgeführt. Für unterschiedliche Gasmischungen wurde festgestellt, dass eine höhere Signalverstärkung ($\sim 10\%$) für einen erhöhten Anteil des Quenchergases CO$_2$ erreicht werden kann. Im Allgemeinen wirkt der Detektor stabiler gegen Entladungen bei einem höheren Anteil an Quenchergas.

Für senkrechten Einfall wurde bei Ar:CO$_2$ 93:7 vol% eine bestmögliche Auflösung von $(116 \pm 2)\,\mu$m bei (89 ± 0.2) % Effizienz für die kombinierte Auflösung der Stereolagen sowie $(135 \pm 3)\,\mu$m bei (93.5 ± 0.1)% Effizienz für die Eta$_{\mathrm{Out}}$-Lage bestimmt. Referenzdetektoren mit der vertrauten APV25 Elektronik, welche für Micromegas Detektoren bisher im Einsatz waren, ermöglichten durch eine zweidimensionale Ortsbestimmung, Drehungen und Verkippungen des getesten Micromegas Detektoren zu korrigieren. Dadurch konnte die Auflösung weiter verbessert werden.

Contents

Chapter 1

Introduction

1.1 The LHC and its High Luminosity Upgrade

The Large Hadron Collider (LHC) at CERN [1] is the currently largest particle collider in the world with 27 km in circumference, located close to Geneva, Switzerland.
The circular machine is most prominent for the discovery of the Higgs boson in 2012 after two years of data collecting at center of mass energies of 7 and 8 TeV.

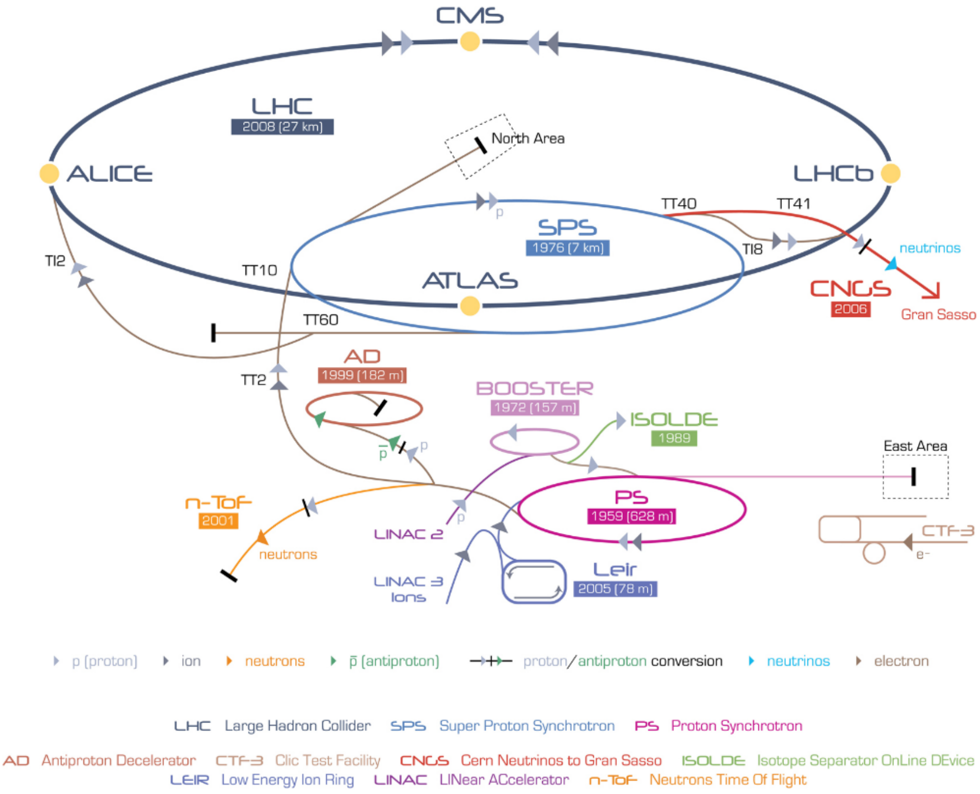

Figure 1.1: A sketch of the LHC tunnel, which is 175 meters beneath the France-Switzerland border. The main experiments are the shown ATLAS, ALICE, CMS and LHCb experiments at the four collision points. Particles are accelerated by preacceleratos e.g. the SPS before injecting them into the LHC. Figure taken from [Halkiadakis, 2011].

---

[1] Conseil européen pour la recherche nucléaire

The particle was independently discovered by the ATLAS and CMS experiments. The LHC houses four main experiments: ALICE, ATLAS, CMS and LHCb (see fig. 1.1). Theses detectors are located at the four collision points of the ring, where bunches of about 10^{11} protons are colliding with a frequency of 40 MHz. The particles are preaccelerated e.g. by the Super Proton Synchrotron (SPS) and then injected into the LHC. To keep them on a circular orbit, superconducting dipole magnets are used to bend the proton beams.

At the end of 2018 the accelerator was shut down for a two year long upgrade, increasing the instantaneous luminosity. The luminosity is a parameter describing the flux density of particle events at the collision points. The value is going to be increased by a factor of 10 to a number above $2 \times 10^{34}\,\mathrm{cm^{-2}s^{-1}}$ (see fig. 1.2). The goal is to have a higher amount of data in a shorter time thus creating higher statistics for rare particle decay channels. These channels can then be used e.g. for the search of supersymmetry or other extensions of the standard model.

As a higher luminosity leads to a higher frequency of particle events at the collision points, the detectors in the beamline of LHC require upgrades as well to run stable at high rates.

Figure 1.2: Upgrade schedule for the LHC. In Run 3 the energy is going to be increased to 14 TeV. Afterwards in Run 4, the integrated luminosity is increased by a factor of 10 in comparison to Run 3. For this reason, the ATLAS detector is being upgraded in two phases. Figure taken from [CERN website, 2016].

1.2 The ATLAS New Small Wheel Upgrade

The ATLAS detector is one of the largest detectors built for particle experiments. The detector features a cylindrical shape allowing particle reconstruction in a 4π enclosure.

It is possible to determine the momentum of a charged particle through reconstruction of its track in the detector. Parts of the muon trackers of the ATLAS detector (see fig. 1.4), are consisting of Monitored Drift Tubes (MDTs) with a single tube spatial resolution of 80 μm, Cathode Strip Chambers (CSCs) and for the trigger signals Resistive-Plate Chambers (RPCs) and small-strip Thin Gap Chambers (sTGCs), realized in two small wheels and two big wheels [ATLAS Collaboration, 2008].

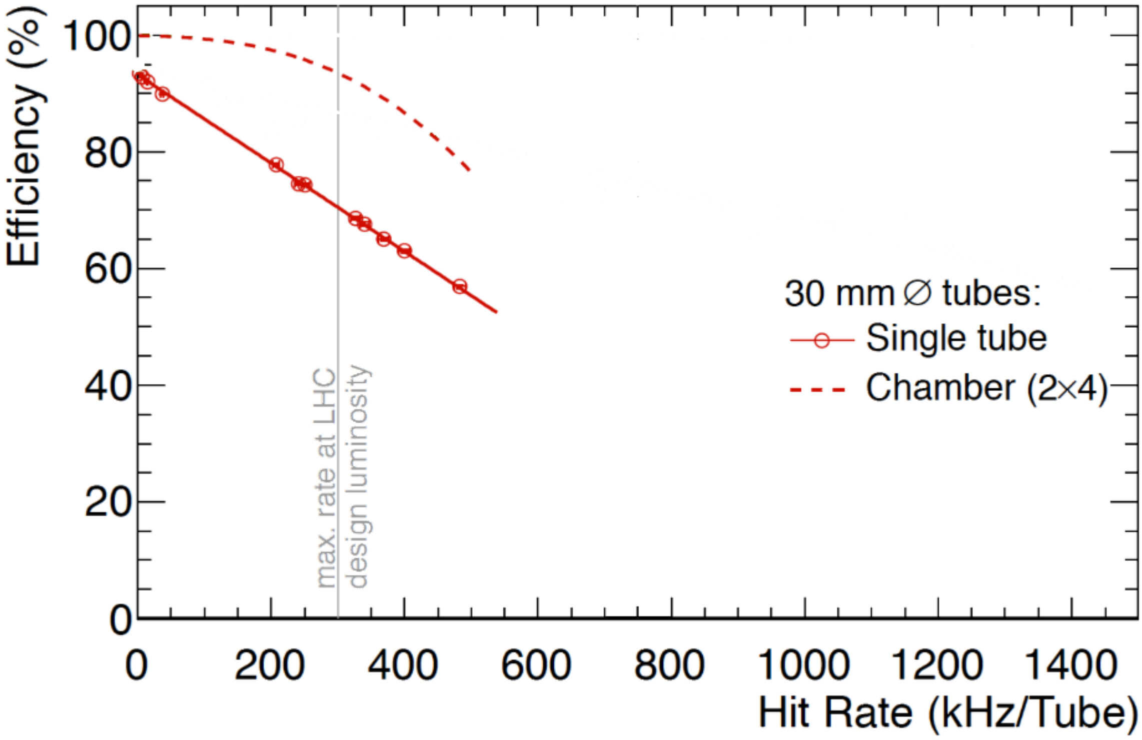

Figure 1.3: Efficiencies of the Monitored Drift Tubes as a function of the hit rate. The points are measured data from a single tube, while the dotted line represents extrapolated efficiencies for a chamber with two times four tube layers. Figure taken from [ATLAS collaboration, 2013].

For the design luminosity (at a hit rate of 300 kHz/tube) of the LHC the MDT detector's efficiency is above 90% and drops significantly for even higher frequencies (see fig. 1.3). The reason for these inefficiencies are ions that are created next to the central wire of the tube. These ions have to drift to the wall of the MDT and thus influence the electric field close to the wire for the electron drift velocity and the avalanche process. This leads to a wrong signal reconstruction especially at high rates which are expected after the high luminosity LHC upgrade.

The upgrade for the ATLAS detector during the long shutdown from 2019 to 2020 is called the phase 1 upgrade. It includes the exchange of the small wheel detectors as well as the exchange of the readout chain and front-end electronics of the small wheel. To operate the New Small Wheel (NSW) efficiently, a high rate stable front-end chip was specifically designed for the new detectors to cope with the challenge of an increased collision frequency.

The MDTs and CSCs are going to be replaced by sTGC and Micromegas [ATLAS collaboration, 2013], which are going to be used for the trigger system and for high precision track reconstruction. The Micromegas detectors for the NSW have trapezoidal shapes varying with the position in the small wheel and are sandwiched by the sTGC detectors (see fig. 1.6). These specific Micromegas allow for readout in two dimensions: The η-coordinate of the ATLAS detector, which can be reconstructed with a precision of around 70 μm for perpendicularly incident particles and the ϕ-coordinate with a precision in the order of mm [Flierl, 2018].

In this thesis tests are performed with the SM2 detector built in Germany by a cooperation of groups from the universities Freiburg, Mainz, Munich and Würzburg (see fig. 1.5).

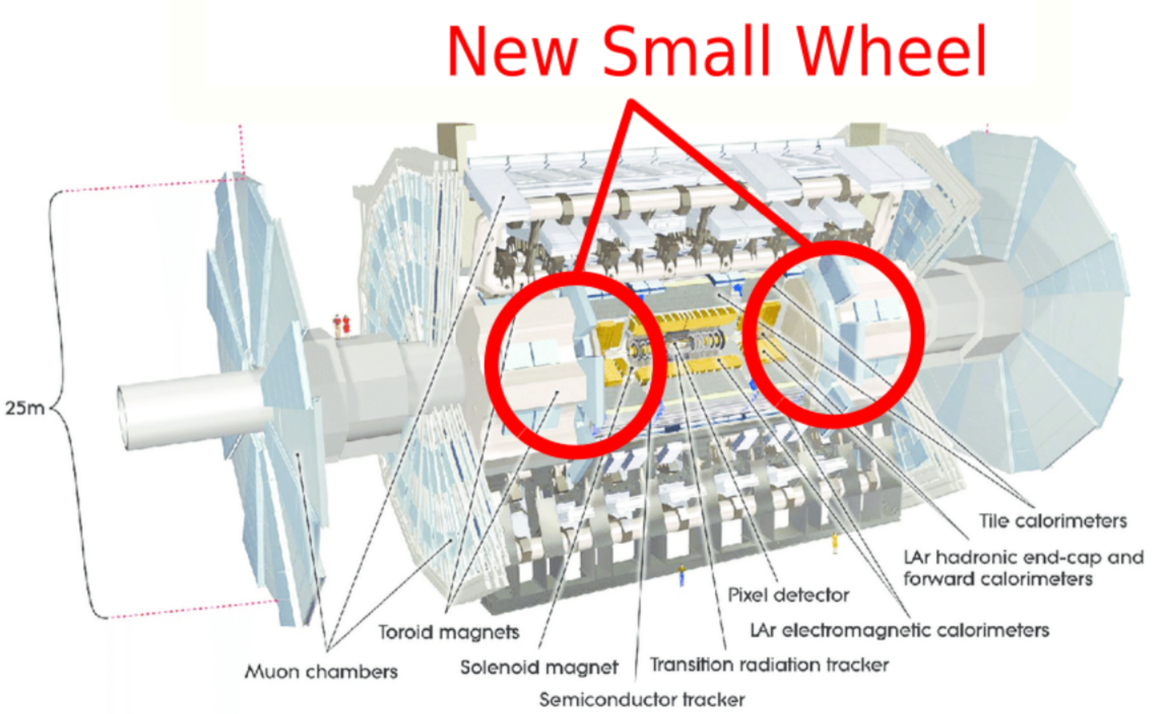

Figure 1.4: The ATLAS detector in a cross-sectional view. The detector itself consists of the inner barrel with pixel detectors, semiconductor trackers and transition radiation trackers located around the interaction point. The hadronic and electromagnetic calorimeters surrounding the inner barrel follow with scintillating material and absorbers. The TGCs and RPCs are used for the trigger system in the muon spectrometer, whereas the MDTs and CSCs are used for offline track reconstruction. These detectors are going to be replaced by the NSW with Micromegas and sTGCs technology. Figure taken from [ATLAS Collaboration, 2008].

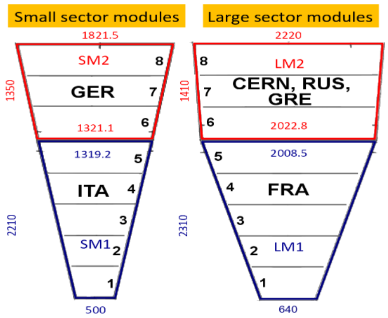

Figure 1.5: The Micromegas small and large sectors are built out of two smaller trapezoidal detectors. The sizes are given in mm and the countries responsible for the construction are indicated. Figure taken from [Lösel and Müller, 2015].

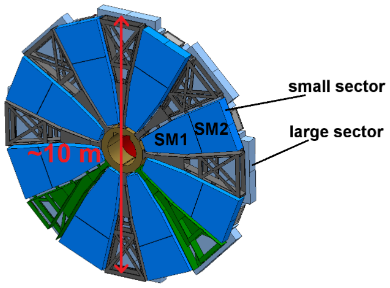

Figure 1.6: The NSW muon spectrometer consisting of small and large detector sectors. These sectors consist of Micromegas layers sandwiched by sTGCs. Figure taken from [Lösel and Müller, 2015].

1.3 The Micromegas Detector

The Micromegas (MICRO-MEsh GASeous detector) was developed by Georges Charpak and Ioannis Giomataris in 1992 as an evolution of the wire chamber [Giomataris et al., 1996]. It finds its main use in particle and nuclear physics, as well as in medical physics. Advantages are the short signal length of around 100 ns and a spatial resolutions below 100 μm with relatively low material budget.

1.3.1 Energy Loss of Charged Particles in Matter

The energy loss of a charged particle in matter is well described by the Bethe-Bloch formula (for parameters see table 1.1) [M. Tanabashi et al. (Particle Data Group), 2018]:

$$-\langle\frac{dE}{dx}\rangle = Kz^2\frac{Z}{A}\frac{1}{\beta^2}\left[\frac{1}{2}\ln\frac{2\gamma^2 m_e c^2\beta^2 T_{max}}{I^2}-\beta^2-\frac{\delta(\beta\gamma)}{2}-2\frac{C}{Z}\right]$$

The stopping power of a muon in copper is shown in figure 1.7. In Micromegas detectors, ionization of gas atoms according to the Bethe-Bloch formula is the detection mechanism. The most probable energy losses in the thin detector are distributed like a Landau distribution: In thin absorbers the energy loss can differ strongly from the mean value due to large energy transfer to target electrons. This leads to a maximum momentum transfer. For thicker layers the energy loss distribution approaches a Gaussian distribution [Grupen and Shwartz, 2008].

parameter	definition	value/unit
K	$2\pi\rho r_e^2 m_e N_A$	eV/m
ρ	mass density	g/m^3
$m_e c^2$	electron mass $\cdot c^2$	0.511 MeV
r_e	classical electron radius	$1.818\,10^{-15}$m
N_A	Avogadro constant	$6.022 * 10^{23}$ 1/mol
Z, A	atomic number, mass number	1
z	particle charge	1
$T_{max} = \frac{2m_e c^2\beta^2\gamma^2}{1+2\gamma\frac{m_e}{M}+(\frac{m_e}{M})^2}$	maximum kinetic energy transfer	eV
M	mass of the particle	kg
$\beta = \frac{v}{c}$	velocity of the particle c	1
$\gamma = \frac{1}{\sqrt{1-\beta^2}}$	Lorentz factor	1
δ	density correction	1
C	correction due to the atomic core	1

Table 1.1: Parameters of the Bethe-Bloch formula

In this thesis tests were performed with 22 MeV protons and 20-160 GeV muons and pions, which as charged particles, test two different regimes of the Bethe-Bloch formula.

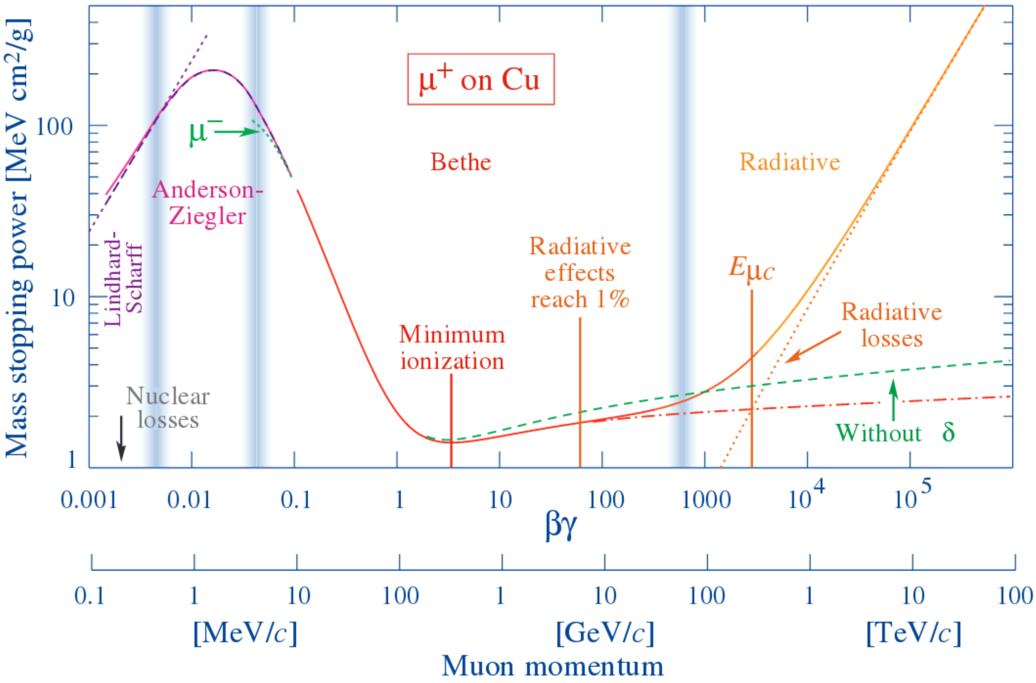

Figure 1.7: The stopping power for muons in copper for different values of $\beta\gamma$ and the muon momentum. For small $\beta\gamma$ at 0.0001 to 0.1 the particle shows high energy loss. At $\beta\gamma$ =3-4 the particle becomes minimum ionizing. At larger $\beta\gamma$ the particle is relativistic, radiative losses dominate. Figure taken from [M. Tanabashi et al. (Particle Data Group), 2018].

1.3.2 Working Principle of the Micromegas Detector

The Micromegas detector (see fig. 1.8), as previously stated, is a gaseous detector. For the gas mixture usally a noble gas (e.g. Argon) is used for ionization with a small addition of a quencher gas. Noble gases have the advantage, that their electronic shell is complete and electrons drifting through the active volume will not be attached to the atom. Furthermore, they are cheap and non-explosive.

The small admixture is a quencher with a broader excitation spectrum (e.g. CO_2) absorbing UV photons created in the amplification process, thus reducing the discharge probability. The detector has in principle three layers: A drift cathode with negative voltage applied, a grounded and gas-permeable micro-mesh and anode readout strips made of a layer of resistive strips. The mesh separates the Micromegas in two different regions: A 5 mm wide drift gap and a smaller amplification gap around 120 μm. Typical operational parameters are a drift voltage of -300 V at the cathode, an amplification voltage of 570 V as well as an Ar:CO_2 mixture of 93:7 vol.%. This leads to an electric field in the drift region of around 600 V/cm and for the amplification region of around 45 kV/cm.

A charged particle traversing the Micromegas detector ionizes gas atoms. The electrons drift towards the micro-mesh and thus to the amplification region and lead to the creation of Townsend avalanches through gas amplification. It is important that the mesh is transparent for the drifting electrons to reach the amplification region.

This transparency depends on the fraction $\xi = \frac{E_{amp}}{E_{drift}}$ between amplification and drift region. For high values of this ratio the transparency can reach values close to 100%. This is required as the ionization electrons alone would not create a measurable signal in the used readout electronics.

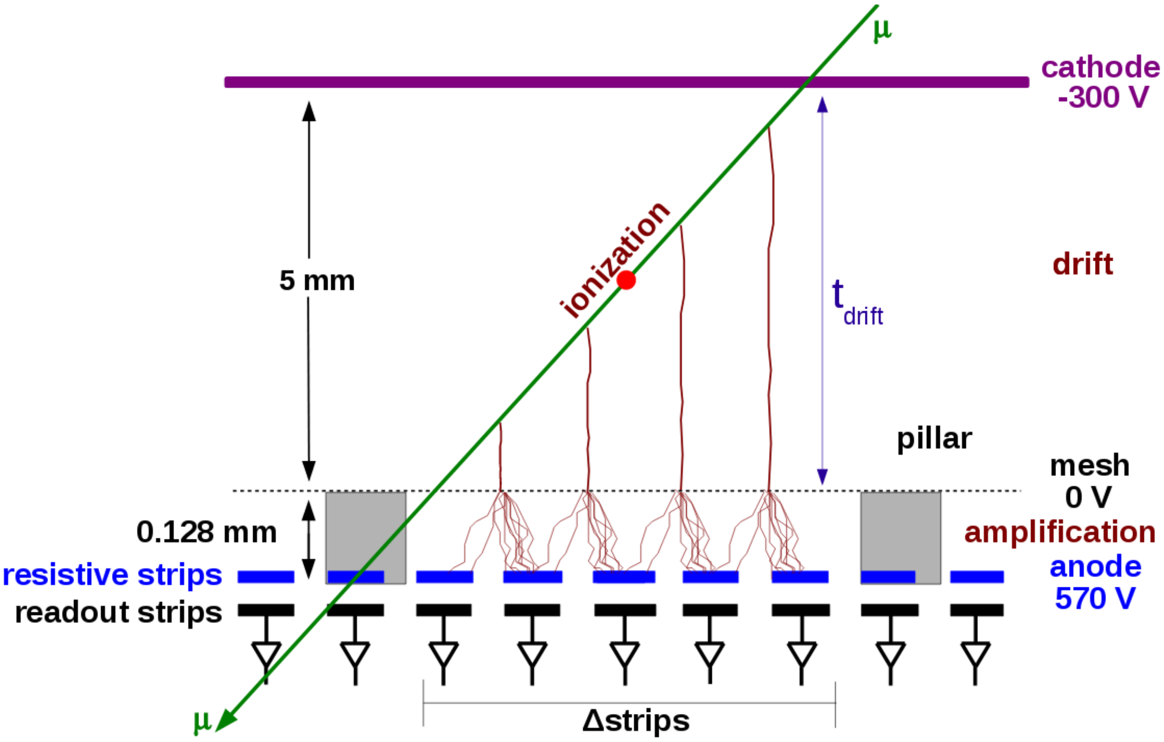

Figure 1.8: Sketch of a resistive strip Micromegas detector. It consists of a drift gap and a amplification region with a high electric field separated by a thin, conductive micro-mesh. A traversing particle will ionize the gas. The electrons drift to the amplification gap creating avalanches which are then collected at the readout strips. Taken from [Lösel, 2017].

The number of multiplication steps depends on the free path length which also depends on the atom density and the cross section for ionization σ_i

$$\lambda = 1/(N\sigma_i) = 1/\alpha$$

The first Townsend coefficient α describes the number of electron-ion pairs created per length dx [Kleinknecht, 1992]:

$$dn(x) = n(x)\alpha\, dx$$

The gas amplification gain $G = e^{\alpha x}$ of the Micromegas detectors is around 10^2 to 10^4.
The electrons created by the Townsend avalanches are then collected by the anode strips. The charge deposited on the strips allows to reconstruct energy loss and position of a traversing particle. If the number of electrons in an avalanche exceeds the Raether limit ($\sim 10^8\, e^-$) a plasma is created in the amplification region and thus equalizing the potential difference between mesh and anode leading to discharges [Raether, 1964]. No amplification can occur preventing the detection of particles. To counteract this, resistive strips are printed on a Kapton foil on top of the anode strips, which are aligned with respect to each other. The highly resistive material ($\sim M\Omega$/cm) limits the equalization of the potential between the anode and mesh to a small area [Alexopoulos et al., 2011].

1.3.3 Design of the NSW SM2 Micromegas Detectors

The NSW modules consist of five panels, two readout anodes and three cathode panels. The panels are honeycomb sandwiches combined with sheets of FR4 [2], carrying either the cathode

---

[2] FR4 is a composite material consisting out of fiberglass and is flame resistant. It is commonly used for printed circuit boards.

or the anode strips (see fig. 1.9).

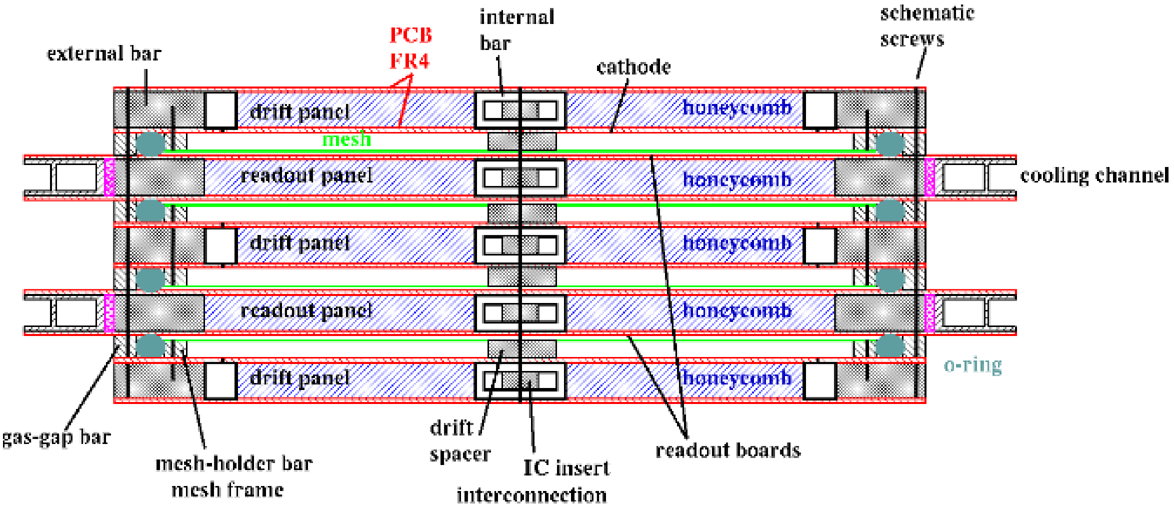

Figure 1.9: Scheme of a SM2 quadruplet. The detector consists of five sandwiches. Two readout panels have anode strips on both sides each. Three drift panels carry the mesh above the cathode plane. The readout strips of the second readout panel are rotated by ± 1.5 ° to the first readout panel to achieve a resolution in regions of millimeters in a non-precision coordinate. The cooling channels are used for the front-end electronics. Figure taken from [Herrmann, 2016].

Each readout panel consists of six adjacent PCBs sandwiching a honeycomb. The alignment of the readout PCBs and panels has to be performed with μm precision. To achieve high stability and planarity the panels are compressed by screws at internal and external bars [Herrmann, 2016].

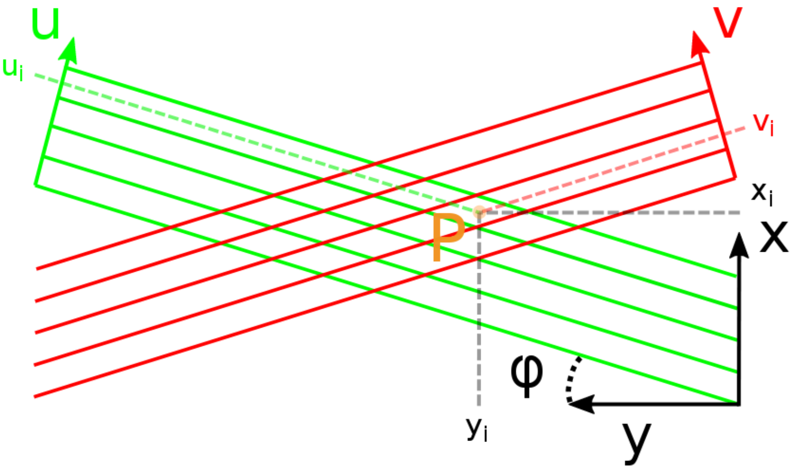

Figure 1.10: The readout strips of the stereo planes are tilted with respect to the Eta strips by ±1.5 ° allowing for a readout in the non-precision coordinate, whereas the readout strips of the Eta layers are parallel in respect to each other. Figure is taken from [Flierl, 2018].

The two readout panels differ by the strip geometry: the readout layers of the Eta panel called Eta$_{in}$ and Eta$_{out}$. Their anode strips are parallel. The strips of the stereo layers are tilted by ±1.5 ° relative to the Eta strips (see fig. 1.10) allowing also for a coarse hit position in the perpendicular direction at a reduced spatial resolution.

A combined position can be calculated in both directions such that the resolution is improved also in the precision coordinates:

$$x_i = \frac{u_i - v_i}{2\cos\phi}$$

$$y_i = \frac{u_i + v_i}{2\cos\phi}$$

.

The position information of the particle in the u, v stereo planes are used to calculate the precision coordinate x_i and the non precision coordinate y_i with the strip inclination $\phi = \pm 1.5°$ [Flierl, 2018].

1.4 Readout Chain of the ATLAS New Small Wheel

As the ATLAS detector has many detector components continuously generating a high amount of data, trigger roads are used to filter out noise and prevent false hit reconstruction. The trigger logic analyses there the fast, but rather coarse trigger information given by the differen detector technology and seachres for tracks pointing to the interaction point of the p-p collisions. For this reason the trigger chain iterates in several steps, which are explained in the following. The focus lies on the Micromegas readout part.

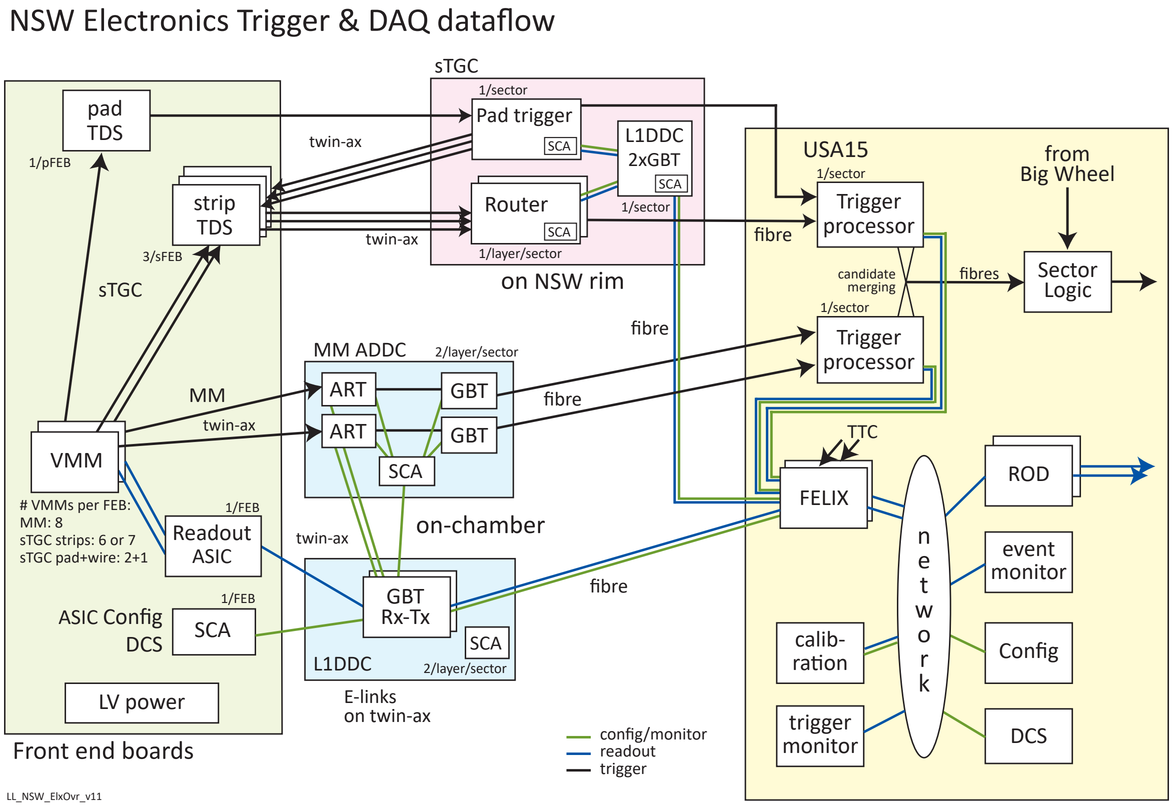

Figure 1.11: The data acquisition and trigger chain of the NSW for one wedge. The VMM front-end readout chip sends the hit data to on-chamber processing chips for both the sTGC and the Micromegas (MM). The chips then send the trigger data as a time stamp and hit address to the trigger processor deciding whether an event is recorded or not. The distribution of the data over a network is then handled through the FELIX interface. Figure taken from [ATLAS collaboration, 2013].

The sTGC detector will act as the main triggering device, however, also the Micromegas detectors are used as redundant triggers.

The first step in the readout chain begins in the VMM front-end readout chip. As soon as a hit is received, zero-suppressed strip data is sent through the Readout ASIC to the Level-1 Data Driver Card (L1DDC) (see fig. 1.11). The trigger information in form of the first responding strip is then sent to the ART data driver card (ADDC) card, which adds a time stamp (address in real time) to the hit information.

The auxiliary chips e.g. the Slow Control Assistant (SCA) are used for the monitoring and configuration of the front-end electronics. The GigaBit Transceiver (GBT) is used for data format conversion.

The data is then sent to the trigger processor and the Front End LInk eXchange (FELIX) interface which handles the readout and works as the router between the front-end links and the network. The interface also handles the distribution of Timing, Trigger and Control (TTC) signals to the front-end boards, that are used for activating test pulses or the data acquisition of the VMMs [ATLAS collaboration, 2013].

Chapter 2

Readout Electronics

In this chapter the relevant readout electronics used during the studies in this thesis is described with a focus on the investigated VMM front-end readout chip. The operating principle, readout modes and calibration methods for the VMM chip are explained.

2.1 The APV25 Readout Chip

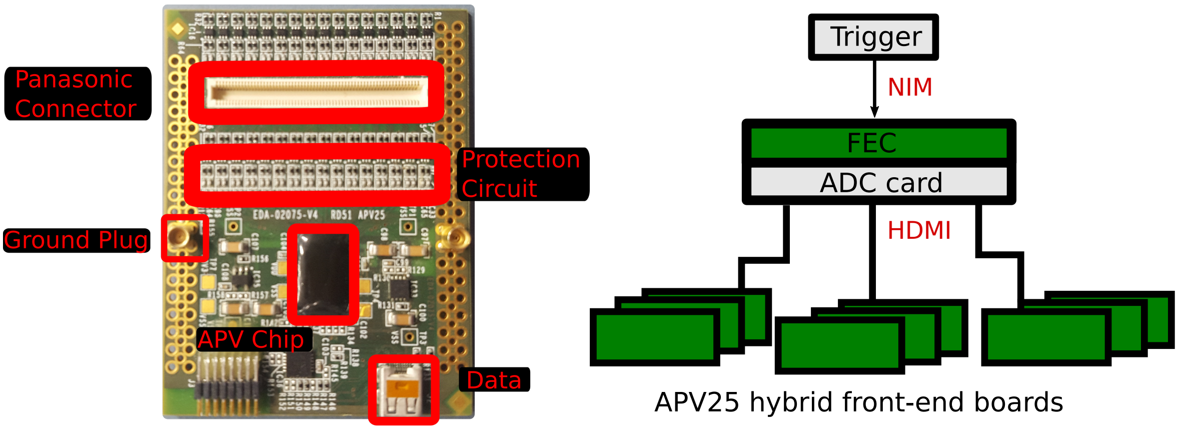

Figure 2.1: Left: The front-end hybrid board carrying one APV25 chip. Right: Example for the readout chain of an SRS-APV25 hybrid. The ADC converts an analog signal from the APV to a digital signal. The FEC is used for synchronization.

The APV25 readout chip is a low-power (1.15 mW), low-noise analog ASIC (Application-Specific Integrated Circuit) originally designed for silicon micro strip detectors of the CMS detector and has been adapted for Micromegas detectors [Jones et al., 1999]. The chip consists of 128 channels which are connected via a 130 pin Panasonic connector to the detector. After accepting a trigger signal the data of all 128 channels is transferred via a HDMI cable to a analog-to-digital converter (ADC) adapter card. The card digitizes the analog signals of the APV25 into a digital signal and transfers it to the front-end concentrator card (FEC). The FEC synchronizes the APV25 readout and is connected to a data acquisition computer collecting the processed signals with 1 GBit Ethernet via UDP protocol (see fig. 2.1, right). The front-end board (see fig. 2.1, left), is an SRS-APV25 hybrid.
The SRS (scalable readout system) allows the user to have a high degree of flexibility for small and large experiments, as for a variable number of FECs and APV25 hybrids the same data aquisition procedure can be applied.

To prevent damage caused by high currents flowing into the ASIC, caused by discharges, the front-end board includes a network of protection diodes and resistors. The APV is also grounded with MMCX plugs to the detector ground. [Zibell, 2014].

Focusing now on the APV25 readout channels, each of them consists of a preamplifier, shaper and a 192 cell deep analog pipeline. The preamplifier consists of a single-ended folded cascode amplifier with 150 fF feedback capacitor. The polarity of the preamplifier can be either chosen to be positive or negative depending on the detector signal. The shaper is the main contribution of noise for the chip at around $246\,e^- \pm 36\,e^-/\text{pF}$ [Jones et al., 1999].

During the data acquisition the APV25 collects the charge and timing information of an incoming detector signal at every channel. The timing is sampled in up to 27 times 25 ns bins which is equal to the bunch crossing clock of the LHC. The pipeline of each channel is used as a buffer for every time bin. The buffer awaits a trigger signal to either transfer the data or overwrite it continuously once the buffer is full. A register in the APV25 accommodates for the trigger latency, when the trigger signal arrives at the ASIC after a p-p collision. The pipeline cell containing an event corresponding to the trigger timing is then flagged for readout [Zibell, 2014].

The number of time bins that are being read out is adjustable. This limits, however, the maximum trigger frequency. For one time bin the maximum trigger frequency can be calculated by the width of a time bin (25 ns) and the number of clock cycles (c.c.) needed for the data protocol UDP (140 c.c.) [Jones et al., 1999]:

$$f_{max} = \frac{1}{140\,c.c. \cdot 25\,\text{ns/c.c.}} = 285\,kHz/\text{timebin}$$

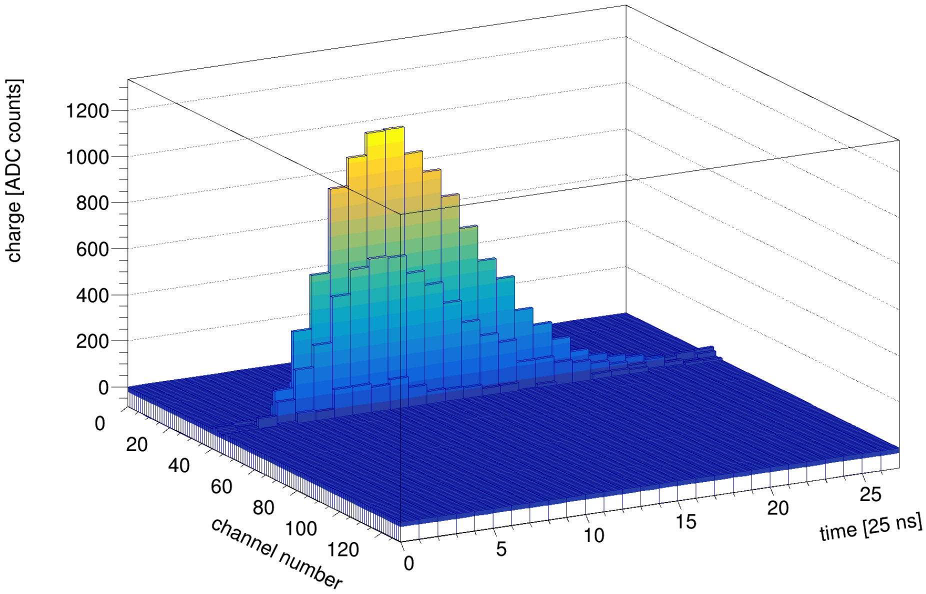

Figure 2.2: A typical base-line subtracted, common-mode noise and zero-suppressed signal of a 20 MeV proton event detected with a small sized Micromegas equipped with a APV25 hybrid: The chip samples charge and timing information of each readout strip. The timing information is binned in 25 ns.

As for one event all of the APV25 channels output time and charge data during the data aquisition, the trigger rate of the APV25 chip is limited because of the 1GBit network bandwidth. The strip signal of the APV25 can be fit to collect the peak of the charge and timing. This information can then be used to reconstruct a hit position of the traversing particle (see fig. 2.2).

The SRS-APV25 hybrid was not designed for Micromegas and other micro-pattern gas detectors, but can be used for the research and developement on it, e.g. to investigate the signal formation of these detector. Because of the high expected rate of the High Luminosity LHC a digital, zero-suppressing chip is required, as the bandwidth of GBit ethernet could not sustain the output of a APV25 readout on the large scale of the ATLAS experiment.

2.2 The VMM Readout Chip

The front-end ASIC specifically designed for the detectors of the ATLAS NSW upgrade is the VMM. This readout chip consists of 64 channels. The charge and timing information is converted into digital, zero-suppressed data.

The core feature of the VMM is the peak detector which records the peak value and its timing of an incoming charge signal, exceeding a threshold. This leads to a reduced amount of data rate compared to the APV25 with a theoretically possible simultaneous readout frequency of up to 1 MHz/channel and 4 MHz/channel in the contineous mode [Polychronakos et al., 2017].

The production of the VMM went through three iterations [De Geronimo et al., 2017] the VMM1 containing only the analog part of the final design, the VMM2 with a digital readout mode not utilizing a specific buffer used for the NSW (see sec. 2.2.3) and the VMM3 with the ATLAS specific L0 mode. Some minor adjustments e.g. in the ADCs were however performed concluding in the VMM3a which is going to be integrated into the NSW. In this thesis the focus lies on the VMM3.

This ASIC is also being implemented into the SRS system to replace the APV25 chip [Lupberger et al., 2018]. Due to the multitude of settings of the VMM readout chip, the chip can be used for variable Micro-Pattern Gaseous Detectors in a variety of applications. One example is the use of this chip for the readout of Floating Strip Micromegas detectors in high-rate medical imaging applications [Klitzner, 2019].

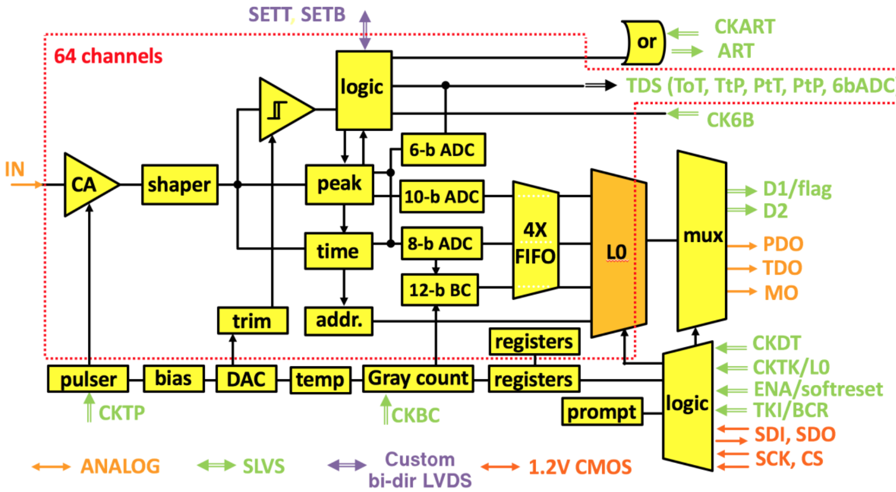

Figure 2.3: Schematic of a single VMM3 channel. An incoming pulse is processed by a charge amplifier and shaper. A discriminator unit accepts signals over a certain threshold and sends it to the neighbor logic unit and afterwards to the Micromegas trigger processor. The peak finder and time detector find the maximum of the charge and its timing, which is then stored in analog memory. Depending on the readout mode the data is then digitized by 6-bit, 10-bit and 8-bit ADCs and stored in the L0 buffer. The VMM2 is missing the L0 buffer and the VMM1 is missing the ADCs and L0 buffer. Taken from [Polychronakos et al., 2017].

2.2.1 Scheme of the VMM Readout Chip

As the VMM is a complex ASIC, the schematic is discussed in detail in the following [Polychronakos et al., 2017]. Each channel of the ASIC uses a low-noise charge amplifier with adaptive feedback, test capacitor and adjustable polarity, chosen negative for Micromegas detectors. The gain can be chosen from eight values between 0.5 - 16 mV/fC (see fig. 2.3).
After the amplifying stage the detector signal or a test pulse from the internal pulser is sent through a shaper. This shaper has an adjustable peak time changing the time of charge integration over the signal. The shaper has a higher resolution at input capacitances smaller than 200 pF.

The amplification and shaping stage is followed by the peak detector, the time detector and a sub-hysteresis discriminator with neighbor logic. The discriminator which has a global as well as a per channel adjustable threshold will forward a signal that is higher than a certain threshold.
The neighbor logic then allows to read out the channels adjacent to the hit one even though it did not cross the channel specific threshold. This is also communicated across different chips via a bidirectional signal. The output is then sent to the ART (Address in Real Time) Data Driver Card which receives the hit VMM channels as well as their timing and sends the data to the Micromegas trigger processor.
The peak finder detects the peak of a detector signal or test pulse (PDO) and stores it first into analog memory. The linear voltage ramp of the time-to-amplitude converter (TAC) is then activated after crossing a or at the time of the peak. The TAC is stopped at the next bunch crossing clock, which counts in 25 ns bins (see fig. 2.4).

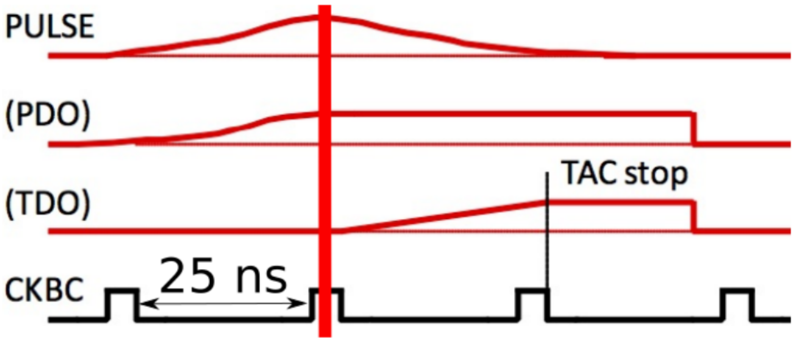

Figure 2.4: Sketch for the working principle of the peak detector output (PDO) and time detector output (TDO). The peak finder of a VMM channel scans a test pulse or detector signal for its peak. As soon as the peak was found, the TDO is linearly ramped up. The ramp up is stopped at the next bunch crossing clock (CKBC) and saved as the TDO. The CKBC always counts in 25 ns steps. Figure taken from [Polychronakos et al., 2017].

The rampup duration of the TAC rampup can be chosen as either 60 ns, 100 ns, 350 ns and 650 ns resulting in a smaller/broader TDO width. The bunch crossing clock counts (BCID) act as the coarse time of the VMM and the digitized amplitude as the fine timing (< 25 ns). The digitized fine timing (TDO) has to be calibrated from ADC channels to nanoseconds.

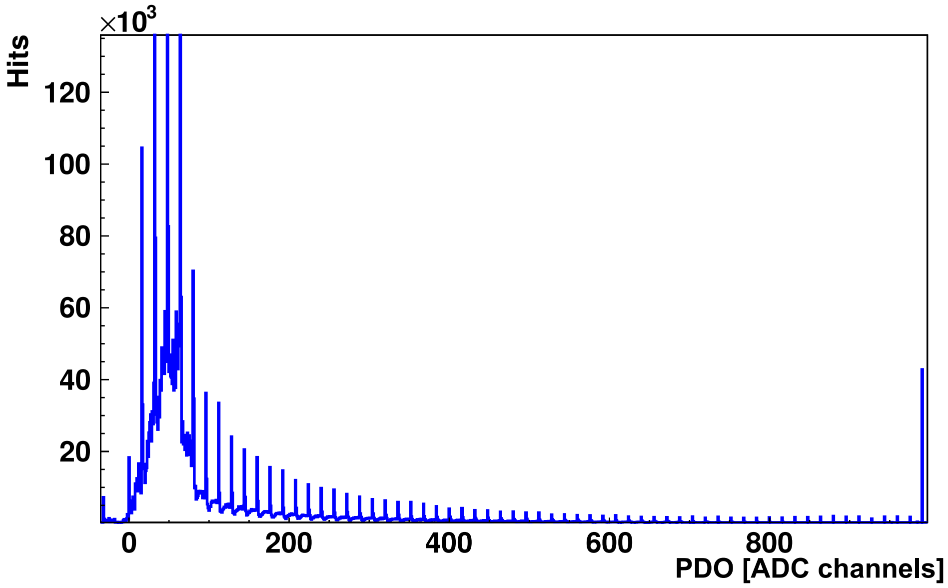

Figure 2.5: A typical strip charge distribution of a SM2 layer equipped with eight VMMs for 120 GeV muons. The charge distribution exhibits periodic bin peaks due to a mismatch in the ADC bit code.

Depending on the readout mode, the data of the peak finder and the timing information are digitized by a 6-bit, 10-bit and 8-bit ADC [Polychronakos et al., 2017]. In the PDO distribution which has a range of 1023 ADC channels due to the 10-bit ADC, periodic charge accumulation of the ADCs is visible (see fig. 2.5). This is due to a known bit mismatch (see De Geronimo et al. [2017]).

2.2.2 Internal and external Readout Modes of the VMM

As previously mentioned different readout modes for the VMM exist. In the VMM2 a continuous non-ATLAS specific mode was implemented, which still exists in the VMM3. In both cases it is possible to choose between an external mode and an internal mode designed for test pulses.

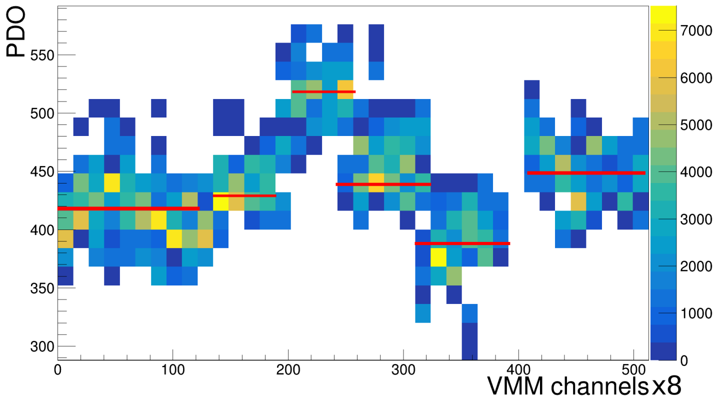

Figure 2.6: A typical measurement with a 300 Digital-Analog-Converter (DAC) counts high test pulses fed to the input of eight VMM3. The baseline changes for each VMM and can be corrected for via a register in DAQ software. The test pulses can be used for calibration of the VMM chip e.g. of the baselines of the VMMs indicated in red.

It can be configured in the settings of the VMM readout software called VERSO [Iakovidis, 2017]. The software allows the readout and configuration process of the VMMs on a front-end board making it possible to set each register option. This is realized through UDP protocol. It saves the settings in an FPGA (Field Programmable Gate Array) as long as the VMM adapater card is not power cycled (see sec. 2.2.7). Also the different readout modes require a different FPGA firmware as the onboard FPGA awaits a clock from e.g. a Clock and Trigger generator and Fan-out (CTF) card in the external mode [Sekhniaidze, 2017].
The CTF card is used for measurements runs generating the VMM clock and synchronization between multiple boards. This card processes an incoming NIM trigger signal and has outputs for four mini-SAS (point-to-point serial protocol) with the current-mode logic 1.2 V signal format. It converts the trigger signal to the VMM format and sends it to the FPGA including an additional clock. It is also possible to send a reset signal to the VMM front-end card.
The internal readout mode is used for sending test pulses to the individual channels, enabling calibrations e.g. for the baselines of the VMM described in a later section (see sec. 2.6). The DAC amplitude in units mV is adjustable and changes the amplitude of the test pulse. One can however also use this mode to use the VMM in a triggerless mode attached to a detector.

2.2.3 Non-ATLAS Specific Continuous Readout Mode

The mode not utilizing the L0 buffer that was implemented in the VMM2/3 is not used in the ATLAS NSW. The data acquisition is started by the FPGA sending a flag (ENA in fig. 2.7) to the VMMs. Similar to the APV25, events are buffered into FIFOs of the VMM after digitization.
With the arrival of a trigger signal or an internal signal at the VMMs, the data is flagged with the token clock CKTK with variable frequency (see fig. 2.7). During the readout of the digitized data (each 19-bit) the CKDT is then activated for 19 clock cycles.

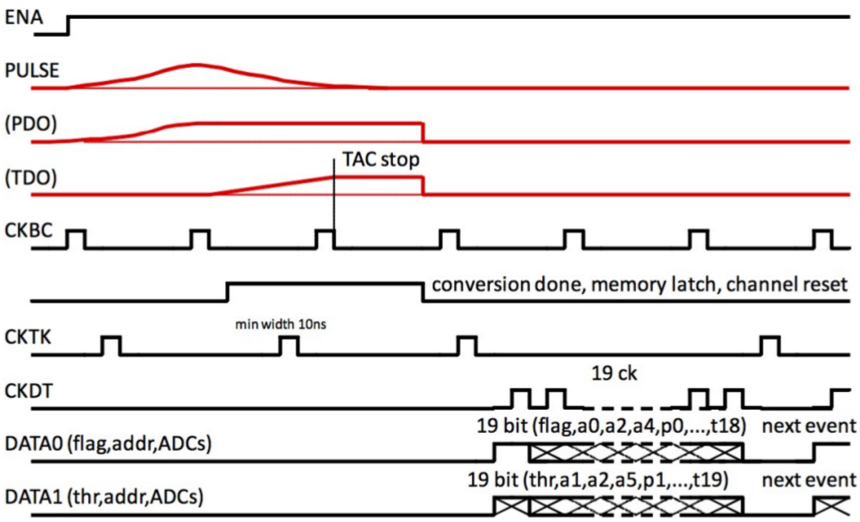

Figure 2.7: Principle of the data acquisition with the continuous mode. The data acquisition is enabled by the ENA signal and records PDO and TDO of the input signal. After digitization of the data in two 19-bit packets, they are sent out in parallel during 19 counts of the data clock CKDT. The token clock CKTK queries for the data. Figure taken from [Polychronakos et al., 2017].

The FIFOs are then emptied and send flagged events to the data acquisition computer. These events are sent in two 19-bit long data packets resulting in an effective data packet of 38-bit [Polychronakos et al., 2017].
The data packet's first bit is a flag always set to 1 and the second bit shows if the event is due to a neighbor logic signal. Then follows the channel number in 6-bit, the PDO data in 10-bit, the TDO in 8-bit and the BCID in 12-bit (see fig. 2.8).

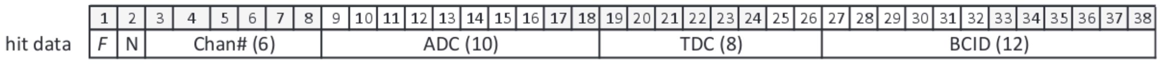

	1	2	3	4	5	6	7	8	9	10	11	12	13	14	15	16	17	18	19	20	21	22	23	24	25	26	27	28	29	30	31	32	33	34	35	36	37	38
hit data	F	N	Chan# (6)						ADC (10)										TDC (8)								BCID (12)											

Figure 2.8: The 38-bit long output of the VMM's FIFOs. The word consists out of a flag (F), activated neighbor logic (N), the channel number, the PDO, the fine and coarse timing. Figure taken from [Polychronakos et al., 2017].

2.2.4 NSW Specific Readout Mode

Due to the requirements of the NSW, additional L0 buffering on the VMM is required. It runs through the same steps as the continuous mode, however, adding the L0 buffer in the chain. One reason is the expected high rates in areas of the sTGCs and Micromegas for example (expected up to 1 MHz per channel in Phase 2). The buffer (B) following the 4-deep FIFOs is a 64-deep FIFO basically used for latency. It can store the data for a period of 16 μs with a readout frequency of 4 MHz (see fig. 2.9). The data is reduced to 32-bit words due to cutting the channel number away, as each channel features such a FIFO. The channel information is added again during the L0 event building [Polychronakos et al., 2017].

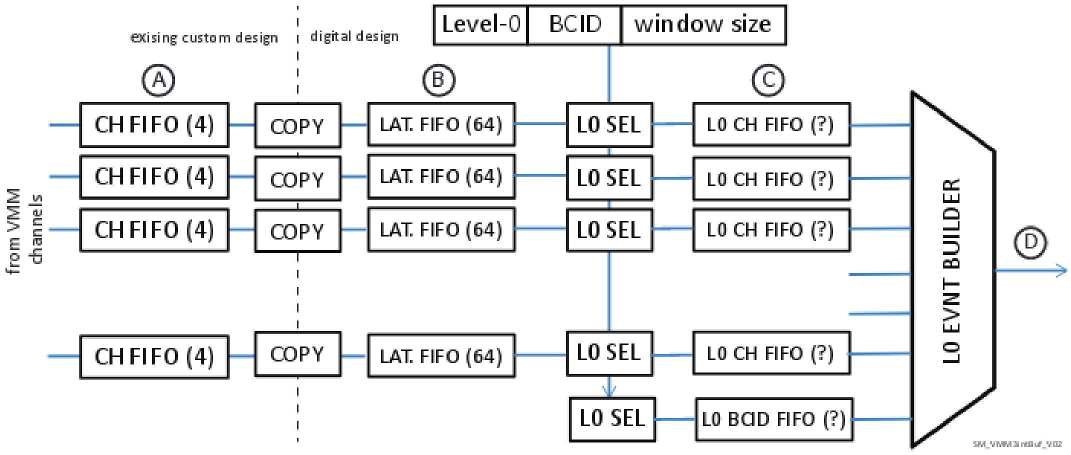

Figure 2.9: Schematic of the VMM buffering. The 4-deep FIFOs (A) follow latency FIFOs (B), a L0 selector and a L0 buffer FIFO, which selects events for readout on the basis of the BCID. Figure taken from [Polychronakos et al., 2017].

The core feature of this mode is the L0 event selector, which can be used to filter e.g. noise through selecting only events in a certain BCID window of maximum eight counts width, chosen by the user.

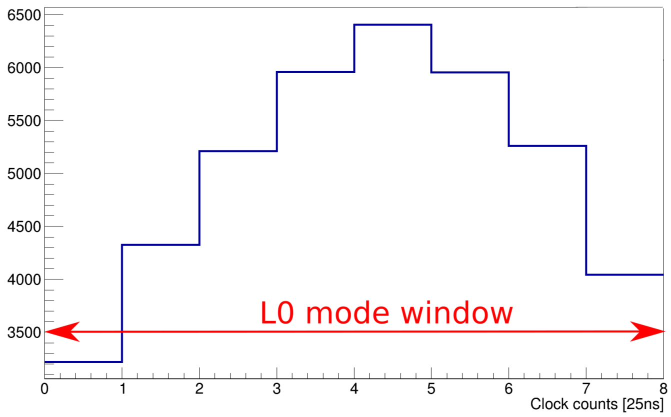

Figure 2.10: The BCID relative to the L0 latency (via the rollover register) is the readout window and can be set to at most 8 counts. If the difference between the L0 registers and the trigger latency matches, a maximum of the distribution is in the center of the BCID window.

In this time window only one hit per VMM channel is possible, as the minimal dead time of each VMM channel is at 250 ns and the window size of the BCID is 200 ns at most (see fig. 2.10) [Iakovidis et al., 2015]. The L0 signal is asserted by the FPGA or Readout ASIC and the L0 readout time is defined by the registers L0 offset and rollover which have to be matched with the trigger latency with respect to the integration time/peak time.

2.2.5 Calibration of the Timing Information

The total timing relative to the trigger signal can be calculated by using the relative BCID to the L0 signal as the coarse timing in 25 ns steps and the fine timing (TDO) which, as previously mentioned, is the ramp up at the peak to the next bunch crossing clock. As it is delivered in ADC counts, it has to be converted into ns.

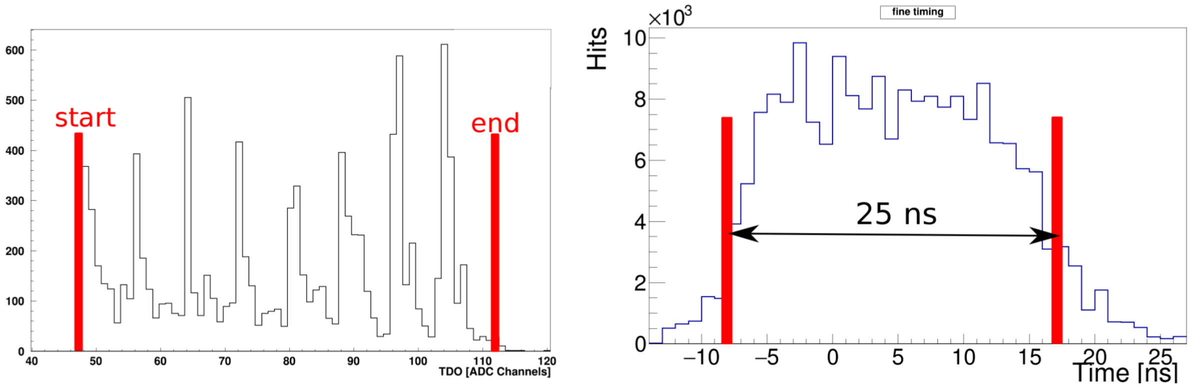

Figure 2.11: Left: Raw TDO for one VMM channel. Right: Calibrated fine timing by self-calibration. The TDO of a raw channel has to be converted to a fine timing to reconstruct the hit timing. Similar to the PDO the TDO shows periodic bin peaks due to a known ADC mismatch (see De Geronimo et al. [2017]). The width of the fine timing histogram should be equal to 25 ns. In this case the TDO was calibrated by using physics data. The outliers are due to noisy strips.

For the time calibration there exist two equivalent methods: calibration by physics data and calibration by the internal pulser. The calibration via physics data (self-calibration) is done by taking the start and end value of the channel's TDO and using the following formula [Scholer, 2018]

$$\mathrm{T_{fine}} = (\frac{\mathrm{TDO} - \mathrm{start}}{\mathrm{end} - \mathrm{start}}) \cdot 25\,\mathrm{ns}\,.$$

This will result in a box-like fine timing distribution with a width that is expected to be equal to the timing of the bunch crossing clock (see fig. 2.11). The outliers in the distribution are due to noisy strips recognized as the first/last strip in the timing distribution by the calibration. This leads to an overestimation of the timing.

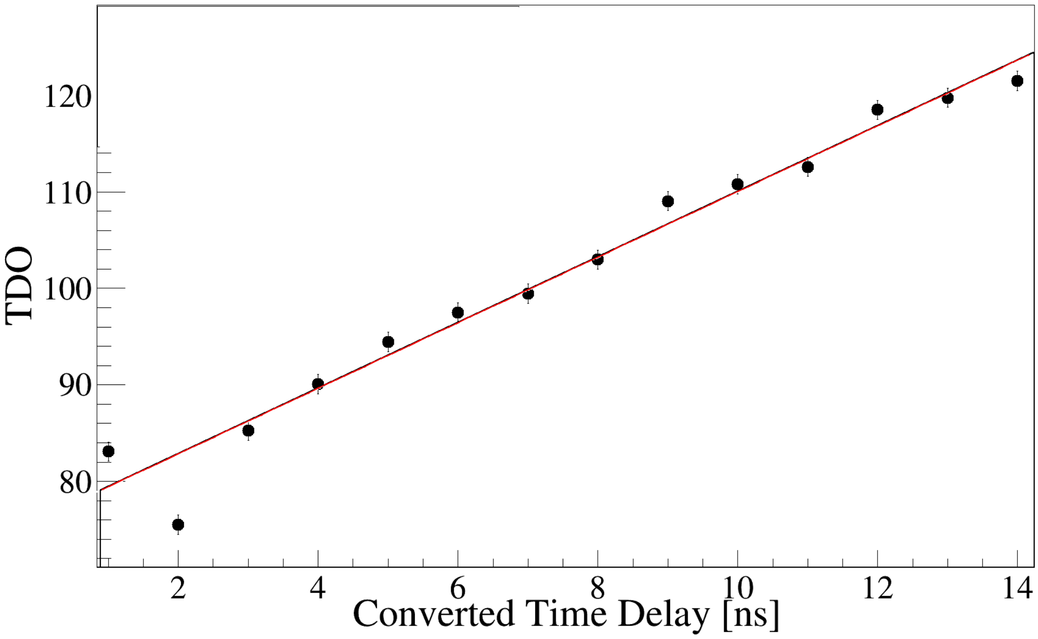

Figure 2.12: The timing of the test pulse can be delayed relative to the bunch crossing clock. A line fit determines the relation between the ADC counts and ns of the TDO. The slope and intercept of the line fit is used to calibrate the TDO of each channel.

The alternative calibration uses the test pulses of the VMM. This is done by shifting the test pulse relative to the bunch crossing clock in nanosecond steps resulting in a linear dependency of test pulse displacement (tpSkew) and TDO. Fitting this with a linear function for each channel individually will give an offset and a slope. The first is subtracted from the TDO while the later is multiplied by the offset corrected TDO.

Both methods will produce the hit time that can be calculated by $\mathrm{t_{hit}} = 25\,\mathrm{ns} \cdot \mathrm{BCID} - \mathrm{T_{fine}}$, as the TDO is recorded at the moment of the peak until the next bunch crossing. For the (overall) time information in the range of the L0 mode window (see fig. 2.10), a box-like distribution is expected with a range $8 \cdot \mathrm{BCID} = 8 \cdot 25\,\mathrm{ns} = 200\,\mathrm{ns}$ (with a periodicity of 25 ns for the bunch crossing clock), as the hits in the drift gap are homogeneously distributed. However, the hit time calculated with the test pulse approach has gaps at 25 ns periodicity meaning that the fit for the testpulse calibration (see fig. 2.13, left) underestimates the timing. The self-calibration (see fig. 2.13, right) shows peaks at the bunch crossing clock periodicity thus suggesting an overestimation of the timing. Thus the readout electronics contributed to the non-optimal time calibration [Koulouris, 2019].

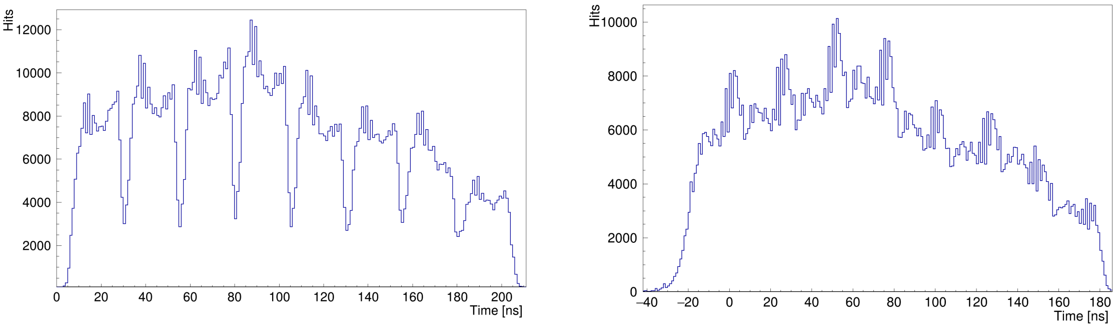

Figure 2.13: Left: Overall time distribution for the calibration via test pulses. Right: Overall time distribution for the calibration via data collected in a test beam with 150 GeV muon. The test pulse calibration shows gaps due to underestimation of the channel TDO.

2.2.6 Calibration of the Charge Information

Similar to the TDO, the PDO can be calibrated into units of fC. The calibration accounts for the gain and pedestal of each individual channel. The channel-to-channel variation can be accounted for by setting the corresponding channel registers as well as the offset for the individual chips. This is done by scanning through different DAC values in mV i.e. different pulse height for the test pulses. From this follows a linear relation between DAC counts and PDO (see fig 2.14) [Iakovidis, 2014].
For the VMM3 due to the digitization the values of the ADCs are fitted for different values of DAC counts to convert the digital PDO into DAC counts and finally into a charge in units of fC.

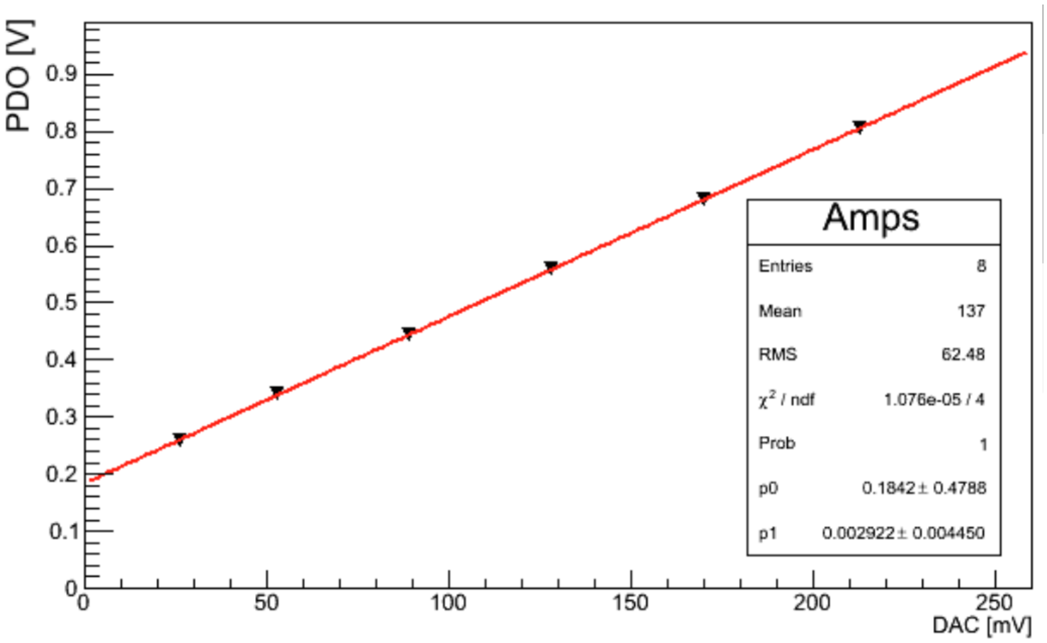

Figure 2.14: The PDO of each channel is measured for different DAC values and can then be converted into fC. The data shown here were recorded with the analog VMM1 for this reason the PDO is not digitized. Figure taken from [Iakovidis, 2014].

2.2.7 The Micromegas Front-end Board (MMFE8)

For the connection between the NSW Micromegas detectors and the ASIC an interface card is required which comes in the form of the Micromegas front-end board (MMFE8).

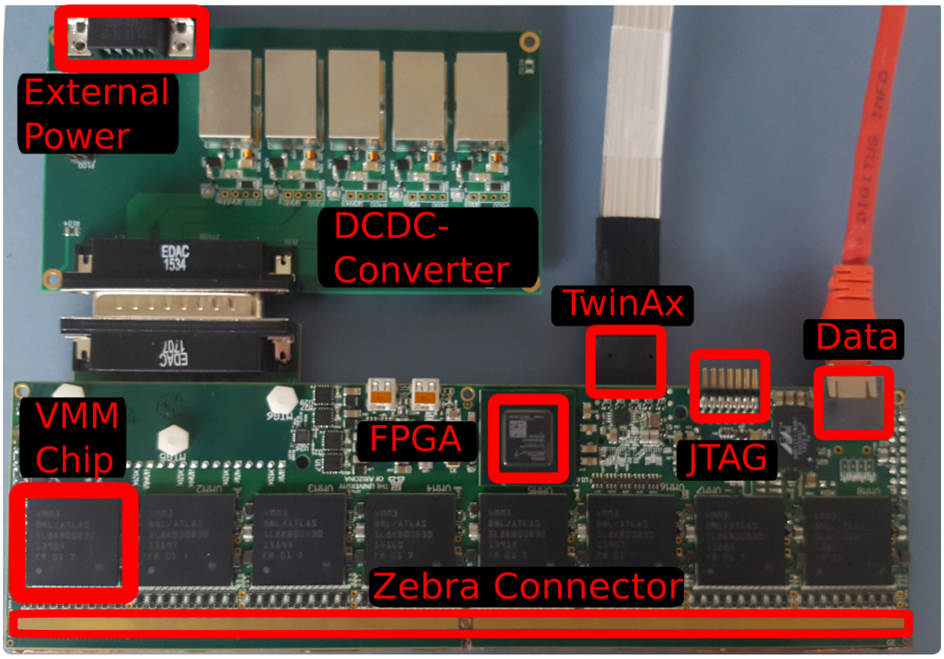

Figure 2.15: A demonstrator MMFE8 front-end board equipped with eight VMM3s. It consists of a connection to Micromegas detectors, an external DCDC converter for power distribution, a FPGA for readout and configuration as well as ports for Ethernet output to a data acquisition computer and trigger input via mini-SAS.

Eight VMMs are mounted onto the MMFE8 board (see fig 2.15) which connects 512 anode strips via a Zebra connector to the channels of the VMM. On the back side of the MMFE8 connector is an analog ground to be connected to the detector.
For the demonstrator cards used during this thesis a field programmable gate array (FPGA) handles the configuration, readout and GBit Ethernet output to a data acquisition computer via UDP protocol. Depending on the used readout mode, e.g. using an external trigger or using the internal pulser, the firmware of the FPGA has to be adapted.
In the NSW the FPGA is going to be replaced by the Readout ASIC and the Slow Control ASIC. In comparison to the FPGA the Readout ASIC will have an output vie E-Link and not a GBit Ethernet output. The Slow Control ASIC allows to monitor and to configure individual chips of a board.
The voltage is distributed to the different ASICs with a DC-to-DC converter which acts as a voltage divider and smoothes current spikes. It transforms the power and voltage to the VMM with 1.2 V digital and 1.5 V analog power. For an input voltage of 6.7 V the whole board's power consumption is estimated to be around 10.6 W. Due to this high power consumption active cooling is necessary in the NSW. The temperature of the VMMs should not exceed 50°C but preferably stay between 30-40° otherwise the life time of the VMMs degrade. After 20 minutes of operation around 52° are reached stabily without active cooling [Polychronakos et al., 2017].
The SAS port is used for receiving a trigger and synchronized clock signal either from a CTF card or in the NSW from an ART Data Driver Card. These cards allow for the readout, synchronization and trigger of multiple MMFE8 cards. It is connected with a MiniSAS cable, which was chosen due to its good signal transmission beyond 200 meters distance.

Chapter 3

Signal Analysis Methods

In this chapter the analysis methods for the data produced by the VMM is explained. A merging script was used combining VMM and APV25 events during the tests with the SM2 module. As only the maximum pulse height and the time of the maximum charge (see fig. 2.2) are used as in APV25 data, it is saved in the VMM format to simplify the analysis. The script is explained in chapter 5.

3.1 Raw Data Signals

A typical strip-charge plot for 100000 20-150 GeV muon events in the Eta_{in} layer of SM2 is shown in fig. 3.1. The plot shows the distribution of the strip PDO on each readout channel. The readout channels are 1:1 mapped to the detector strips. The counting convention for the strip number is as shown in fig. 3.1 to start counting at the 0th VMM and add 64 to the channel number for each adjacent VMM. For the reconstruction of a particle hit position, adjacent strips are merged forming a cluster. The cluster position determined either by the centroid or μTPC method (explained in sec. 3.3 and in sec. 3.4.3) defines the hit position of an incident particle. The data show the beam spot of the incident particles in the range of the first to third VMM (ranging from VMM channel 120 to 200). The channels of the outer most VMMs (VMM 0/7) only show noise as the outer region of the detector SM2 is far off around the beam spot. These VMMs are excluded from the analysis of SM2 as the 10x10 cm^2 Micromegas chambers with 256 strips, do not cover this region.

The PDO has an offset of 32 ADC counts due to an offset in the peak and time detector following the conversion ADCs. It is subtracted at this stage. Depending on the VMM gain/threshold setting and detector setup the strip charge is required to exceed a threshold of 30 to 40 ADC channels. Otherwise the strips are excluded from the analysis.

The timing is required for the reconstruction of inclined particle tracks (see sec. 3.4.3), which is shown in fig. 3.2. Most of the hits in the beam spot are in between the third and fifth bunch crossing clock count such that the hits causing a trigger signal are centered around the middle of the BCID window. The calibrated time (by test pulse calibration) shows empty lines with a periodicity of 25 ns, which is because of the underestimation of the fine timing (see fig. 2.13). Also visible are the channel-to-channel variations at 25 ns intervals. For the timing information it is required to lie in the range of eight relative bunch crossing clock signals around the trigger signal.

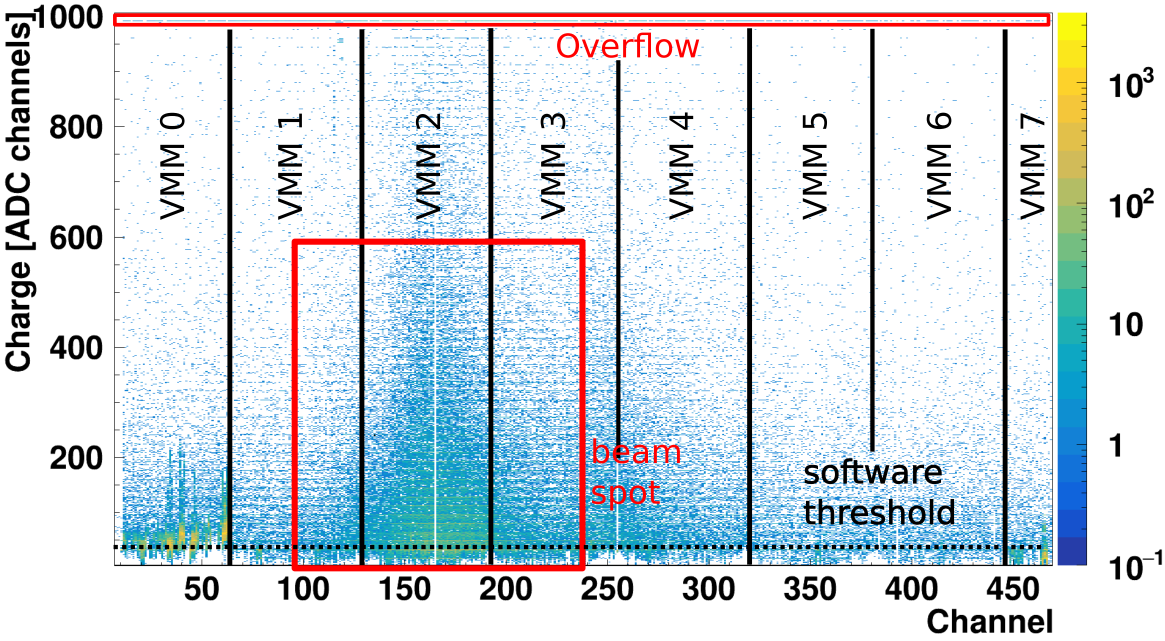

Figure 3.1: The PDO (strip charge) against channel number of the VMM after subtracting an ADC offset of 32 for Eta_{In} from 100000 muon events. The beam spot is located in the region between channels 120 and 240 (red). The two outer most VMMs show only noise. The charge bin 991 is the overflow bin, which is cut during the analysis (red). The VMM channels 155 and 252 are likely not connected or damaged, as they don't show any charge data. A cut is applied to reject strips with charge below the PDO threshold of 30 ADC counts.

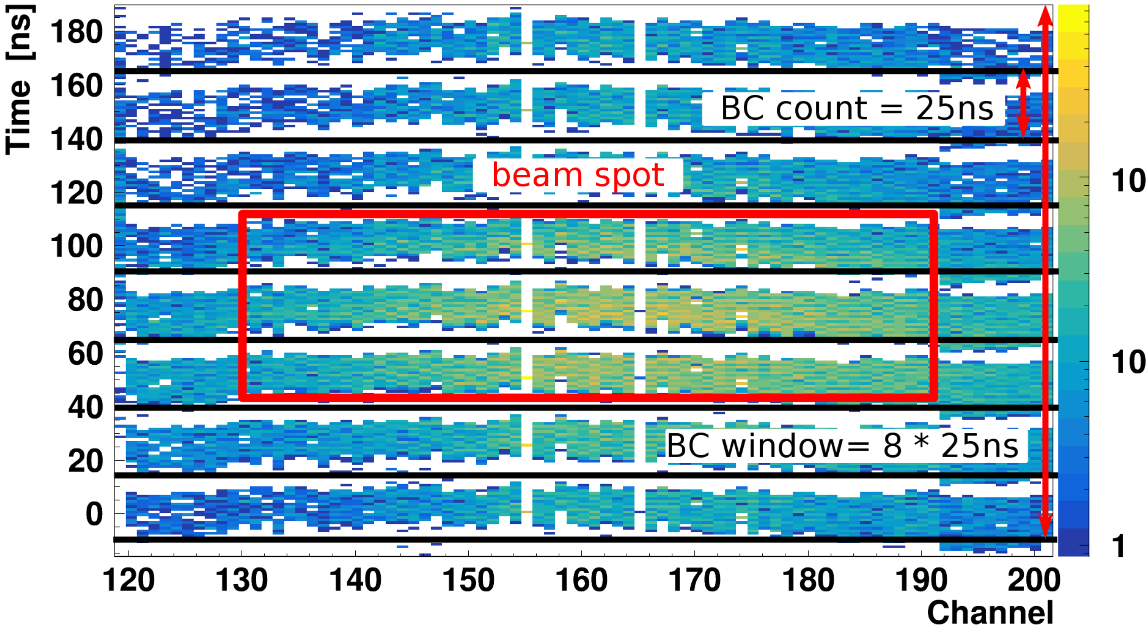

Figure 3.2: Time against channel number of the VMM (calibrated via the test pulse approach) for $\mathrm{Eta}_{\mathrm{In}}$ from a muon measurement with a logarithmic scale on the z-axis. The beam spot is centered around the middle of the BCID window (y-axis). Gaps exist due to the underestimation of the TDO signal during the calibration.

3.2 Cluster Formation

Clusters are adjacent strips which can be identified as the signal of an incident particle. To prevent the inclusion of noise the strips have to be above a certain charge threshold. This is done during data taking with the corresponding VMM registers, but also in the analysis, due to channel-to-channel variations (see fig. 3.1). The cluster charge is proportional to the energy deposited in the drift gap by a traversing particle. Depending on the angle up to three consecutive strips below threshold are allowed in the cluster building algorithm.
A Landau distribution is expected for the charge distribution of the leading cluster (the cluster with the highest charge) (see fig. 3.3) in the thin gasesous detector, as explained in sec. 1.3.1. For higher values of the amplification voltage U_{amp} the number of avalanches in the amplification region increases and with that also the most probable value (MPV) of the Landau distribution shifts to higher charges.
An additional requirement is the cluster size or strip multiplicity of a cluster. For particles at perpendicular incidence it has to be greater than one strip to filter noise hits and greater than two for inclined tracks otherwise a timing fit is only defined by two points (see sec. 3.4).

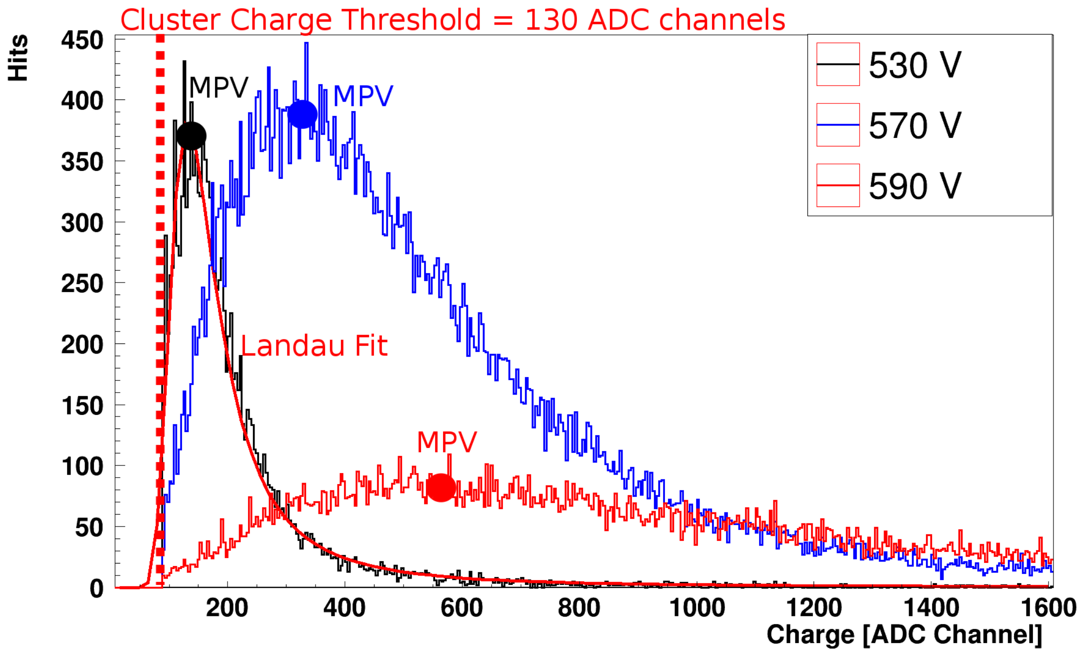

Figure 3.3: Cluster charge distributions for a varying number of muon events at 160 GeV of $\mathrm{Eta_{In}}$ for a perpendicular track with a most probable value (MPV) of 137±6 ADC ch. for U_{amp} = 530 V, 327±1 ADC ch. for U_{amp} = 570 V and 563±3 ADC ch. for U_{amp} = 590 V determined by a fit with a Landau functions. The minimally allowed cluster charge in this run is at 130 ADC channels. It was taken with a drift voltage U_{drift} = 300 V and a gas mixture of Ar:CO_2 93:7 vol% for $\mathrm{Eta_{In}}$.

3.3 Centroid Hit Position Reconstruction

To reconstruct the hit position in the detector different approaches exist using the strip number and charge/timing information of the detector. The centroid method is performing well for perpendicular tracks or inclined tracks with an incident angle smaller than 10° [Bortfeldt, 2014]. The charge-weighted mean can be calculated by:

$$x_{cen} = \sum_{i_{strip}} \frac{i_{strip} \cdot Q_{strip}}{Q_{cluster}} \, ; Q_{cluster} = \sum_{i_{strip}} Q_{strip}$$

where i_{strip} resembles the readout strip number in the detector, Q_{strip} is the strip charge and $Q_{cluster}$ is the cluster charge (sum of all adjacent strips).

For inclined tracks a charge-weighted hit position reconstruction is not ideal, as it will lead to a limited spatial resolution. This is due to the fact that the energy deposits from particles is not homogeneous along the track in the drift region, leading to a false hit position reconstruction during the clustering, due to a non-Gaussian-like charge distribution over the strips (see fig. 3.4).

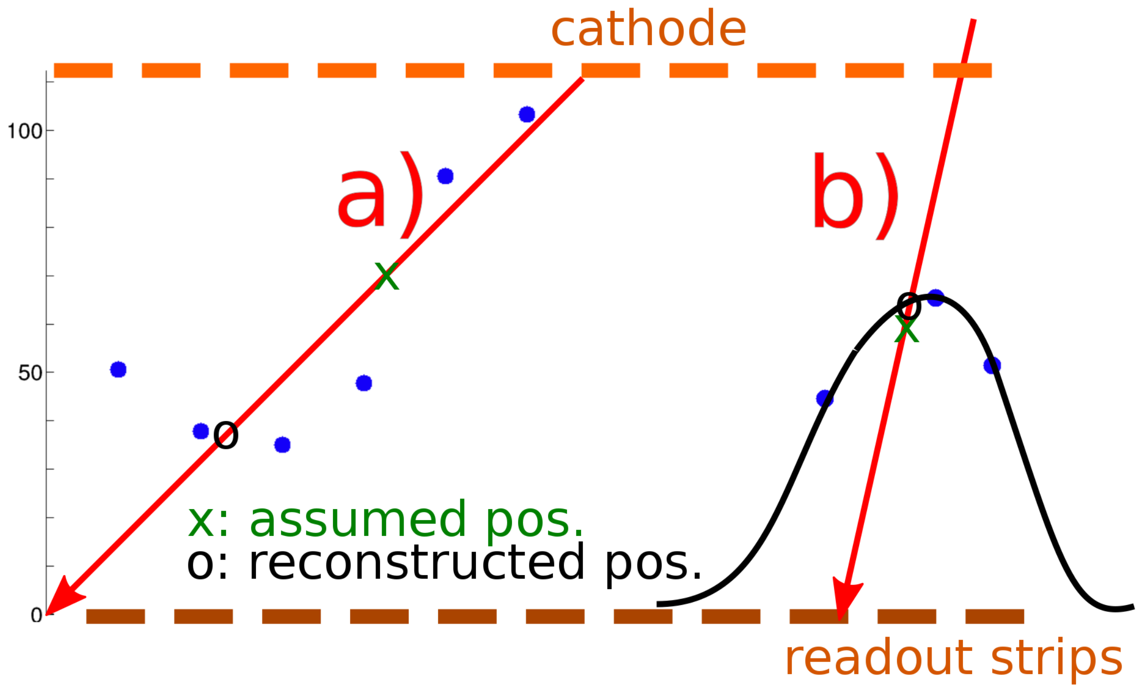

Figure 3.4: Data for the strip-charge of raw muon events in $\mathrm{Eta_{In}}$ at $U_{amp} = 580\,V$, $U_{drift} = 300\,V$.Ar:CO_2 93:7 vol% for a) 30° inclination and b) inclination $<$ 10°. In the case of b) the charge on the strips is Gaussian distributed, which is not the case for a) leading to a wrong hit position reconstruction via the charge-weighted approach.

3.4 μTPC-like Reconstruction

3.4.1 Incident Angle

The μTPC approach uses the timing information in a way similar to a time-projection chamber, which was invented by [Nygren, 1974]. As ionization electrons created at the cathode travel longer than electrons created near the mesh, the drift time difference of the ionization electrons in the drift gap can be measured. A fit to the strip time data points is used to reconstruct the incident angle and hit position (see fig. 3.5).

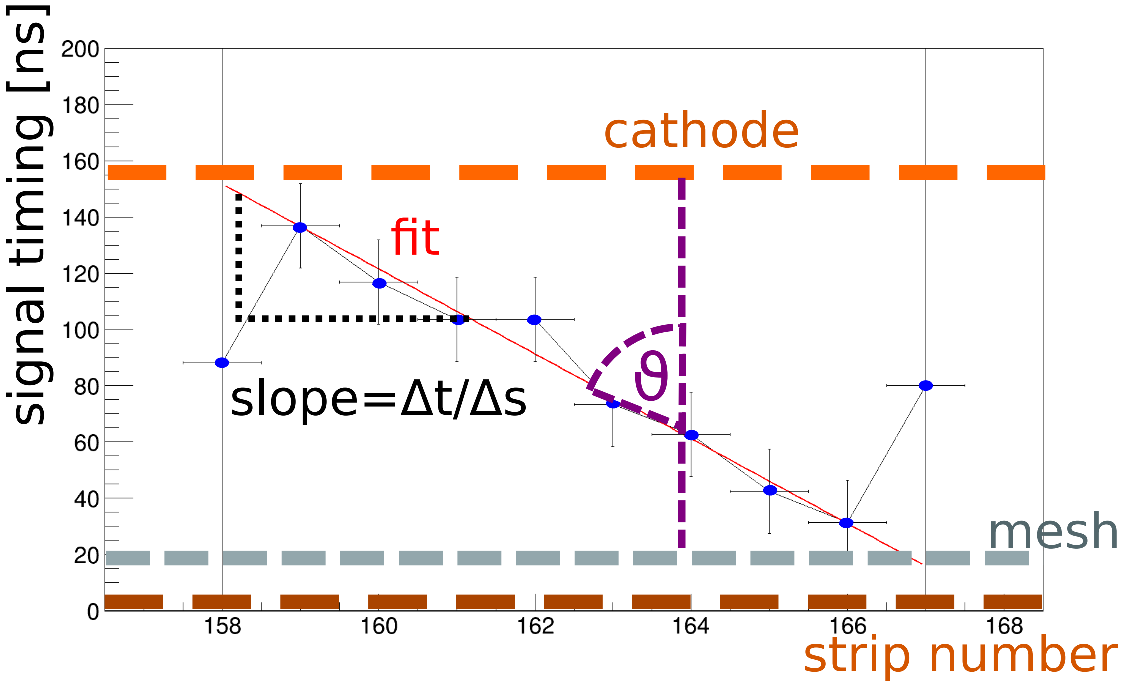

Figure 3.5: Track reconstruction of a pion traversing the $\mathrm{Eta}_{\mathrm{In}}$ layer of SM2 at a 30° angle. A fit to the strip-data can be used to calculate the position and angle of the particle. Data is taken from a measurement. Mesh and strips are indictaed in the drawing schematically. In reality ionization electrons are creatd at the mesh have drit times below 1 ns.

The incident angle of the particle can then be calculated by

$$\theta = \arctan(\frac{p_s}{a \cdot v_d}) \, ,$$

where the pitch p_s and slope a are known and the drift velocity is simulated or measured directly (see sec. 3.4.2). A typical angle distribution is shown in fig. 3.6 for the Eta_{in} layers with muons at 30° inclination. To extract the angular spatial resolution the distribution is fit using a piece wise Gaussian function [Bortfeldt, 2014].

Typical for the distribution is a tail to bigger reconstructed angles because of capacitve coupling between neighboring strips and uncorrelated detector noise. For particles traversing the detector at an angle relative to the readout plane the particle creates more primary electrons than for a perpendicular incident particle leading also to a higher variation of charge and timing information across the strips.

If capacitve coupling occurs between neighboring VMM channels, this directly leads to a wrong track reconstruction due to the spread of the time information across the channels.

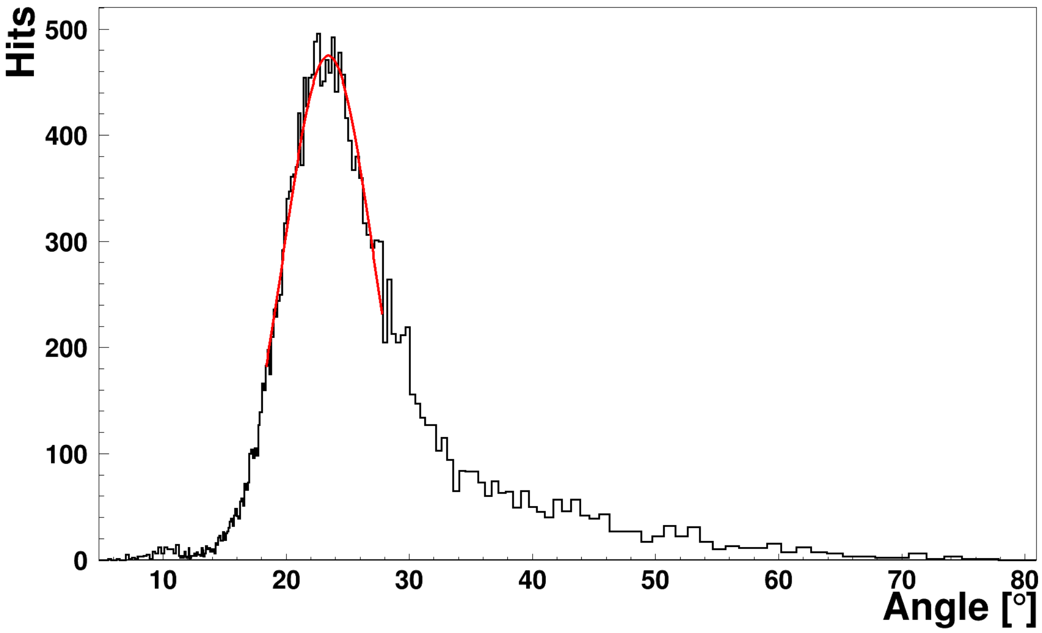

Figure 3.6: An example for the angle distribution for a 10x10 cm^2 Micromegas (Ar:CO$_2$ 93:7 vol%, U$_{\mathrm{amp}}$ = 480 V, U$_{\mathrm{drift}}$ = 250 V) recorded with protons of 20.6°. A Gaussian fit determines the most probable angle $\theta_{max} = 23.4 \pm 0.5$. Two Gaussian fits below and above this value determine the angular spatial resolution.

To account for the capacitve coupling at the edges of the cluster and thus including a false time information in the μTPC fit, the first/last strip of a cluster are discarded, when its PDO is below half that of the neighboring strip's PDO (see fig. 3.7).

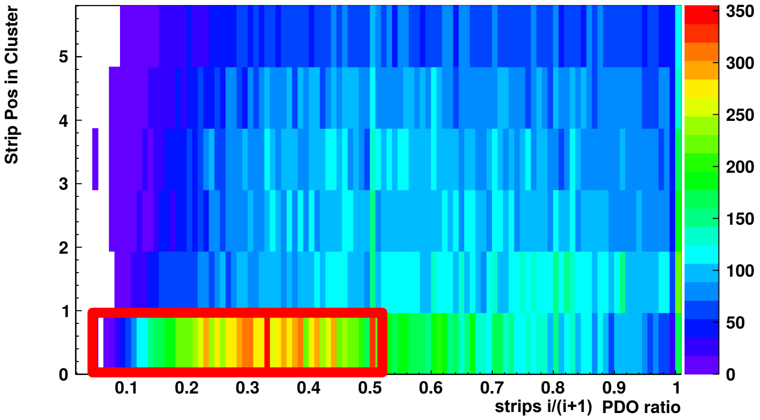

Figure 3.7: The ratio of the PDO between a strip i and its neighbor i+1 against the strip position in the cluster. For the first strip in the cluster the distribution differs from the remaining strips hinting at crosstalk.

Also the strip is excluded from the fit, if the fine timing is not in between 0-25 ns meaning that the time calibration for this hit has failed. To discard events that reconstruct a bad angle or hit position due to the quality of the fit χ^2-minimization is applied in the analysis with $\chi^2 < 0.2$

3.4.2 Determination of the Drift Velocity

If the angle is known, it is possible to calculate the drift velocity of the primary electrons with the pitch p_s and slope a by:

$$v_d = \frac{p_s}{a \cdot \tan(\theta)} \,.$$

Alternatively it can be calculated via the time difference of the first and last responding strip Δt obtained by a Gaussian fit of the drift time (see fig. 3.8) and from the distance d between the drift gap and mesh:

$$v_d = \frac{d}{\Delta t} \,.$$

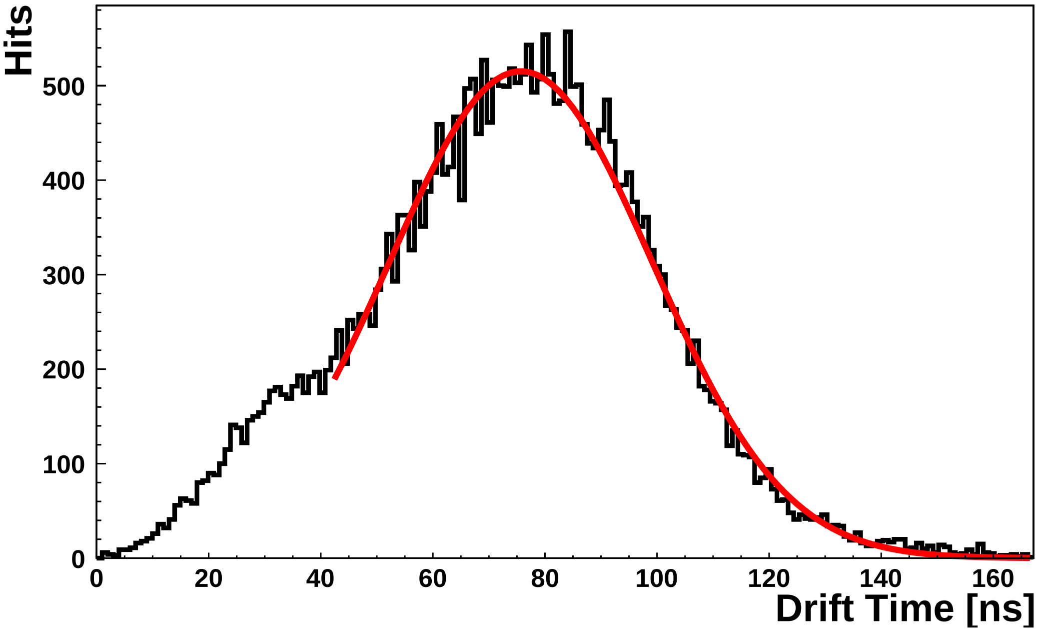

Figure 3.8: The drift time for 50000 proton events with a 10x10 cm^2 Micromegas detector at $U_{\mathrm{drift}} = 500\,\mathrm{V}$. A Gaussian fit is used to determine the drift time $\Delta t = (75.7 \pm 0.2)\,ns$ this leads for a 5 ±1 mm drift gap to a drift velocity of 66±13 $\frac{\mu m}{ns}$ for Ar:CO$_2$ 93:7 vol%.

3.4.3 μTPC Hit Position

In the same way as the incident angle the μTPC position $x_{\mu TPC}$ can be extrapolated via the line fit as a position that is independent of the charge distribution and thus independent of inhomogeneous ionization along the track.
For $x_{\mu TPC}$ the time of the electron passing through half of the drift gap $t_{\frac{1}{2}}$ defines a charge independent hit position (in fig. 3.9)

$$x_{\mu TPC} = \frac{t_{mid} - b}{a} \,.$$

According to Flierl [2018] the time t_{mid} is determined by the dependence of the difference between a predicted hit position and the measured hit position of the detector with the slope of the track fit (see fig. 3.10).

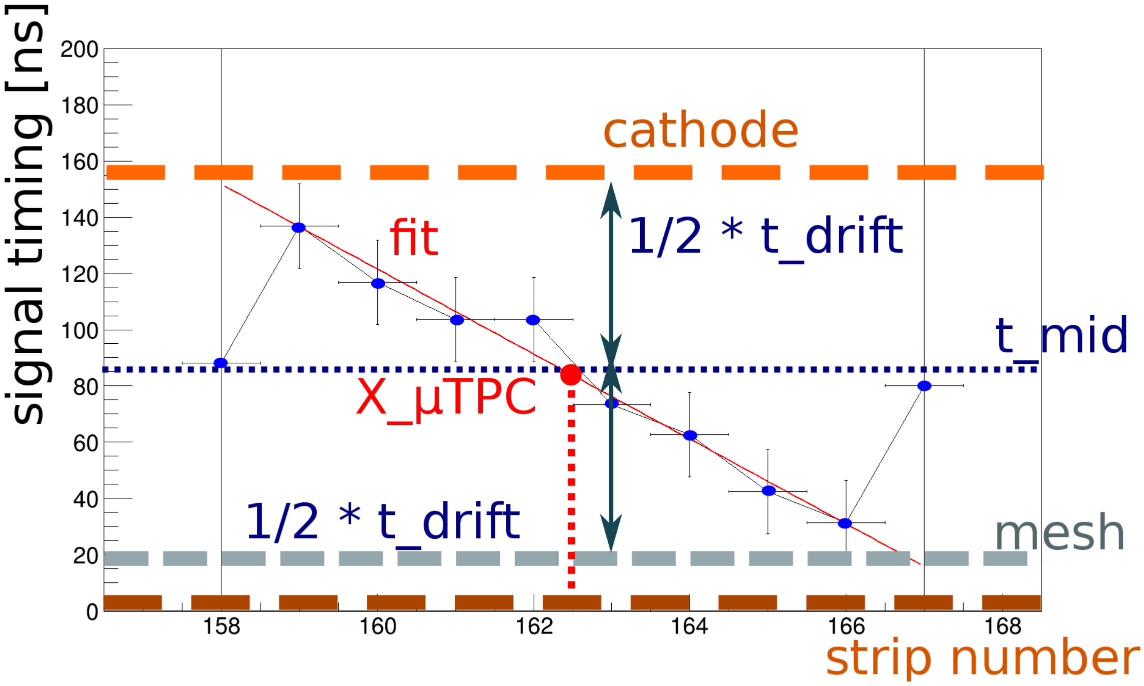

Figure 3.9: Track reconstruction for a 120 GeV pion traversing the $\mathrm{Eta_{In}}$ layer of SM2 at an inclined angle. Indicated is the drift time $t_{mid} = \frac{1}{2} \cdot t_{\text{drift}}$ which is the time a particle requires to travel half the drift gap.

A time t_{mid} differing from the actual value leads to displaced tracks for different particle events. If the timing of t_{mid} was determined correctly all inclined particle pass through this point.

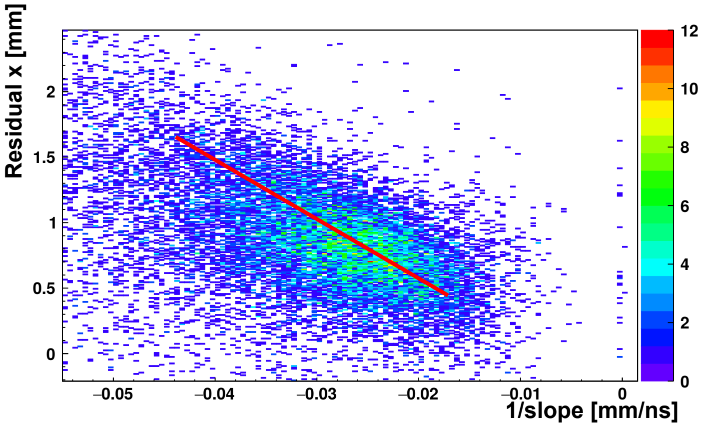

Figure 3.10: Differences of $\mathrm{x}_{\mu TPC}$ against the inverted line fit slope to determine the $t_{\frac{1}{2}}$ with an exemplary fit indicated here. The fit parameters are $p_0 = (0.26 \pm 0.01)\,\mathrm{mm}$ and $p_1 = (-19.7 \pm 0.3)\frac{ns}{mm^2}$, which leads to $t_{\frac{1}{2}}$ =19.7 ns in the analysis.

3.5 Track Reconstruction and Efficiency Calculation

In this section the methods for the spatial resolution and efficiency calculation are explained.

3.5.1 Residual from two Detector Layers

For two detector layers of equal characteristics the spatial spatial resolution can be directly calculated by the hit position difference $\Delta x = x_2 - x_1$, if the incident beam is perpendicular to the readout layer. This will then result in a residual distribution Δx as shown in fig. 3.11

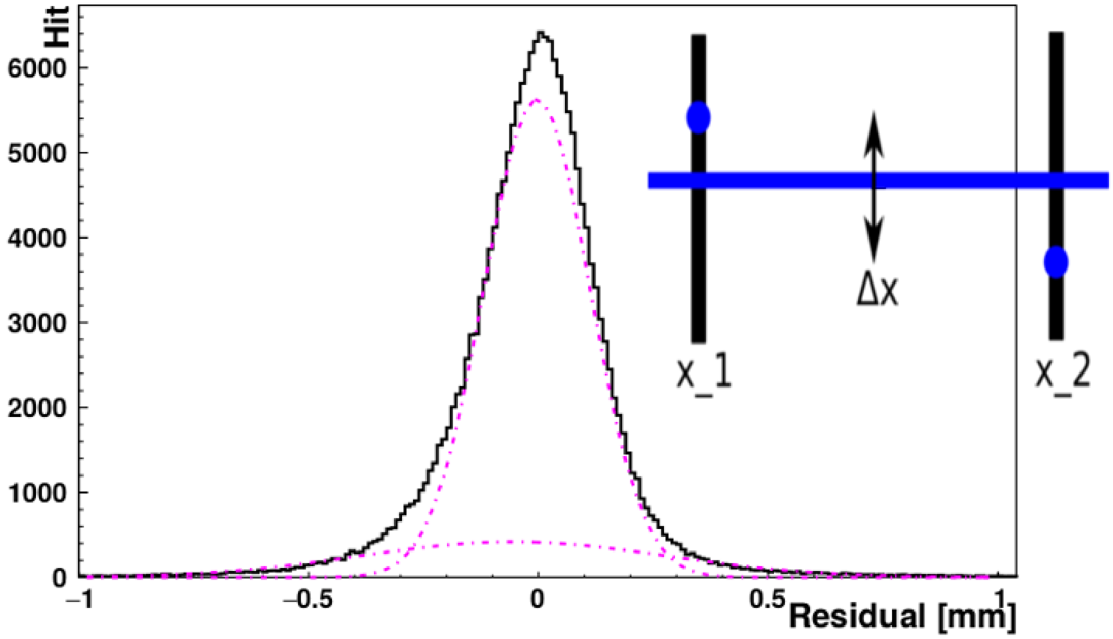

Figure 3.11: Back to back residual distribution of both Eta layers for 500000 muon events with a sketch of the detectors that are compared in their hit position. The asymmetry is due to a rotation about the x-axis and can be eliminated using the information of the 2-dimensional tracking detectors used for this measurement. The width of the distribution can be calculated by weighting the two Gaussian fits. The weighted residual $\sigma_{res} = 84\mu m$ and the spatial spatial resolution can then be estimated as $\sigma_{SR} = \frac{\sigma_1}{\sqrt{2}} = 59\mu m$ (see main text)

The residual distribution in fig. 3.11 is fit with a double Gaussian function with a combined spatial resolution. The core Gaussian describes the intrinsic spatial resolution of the detector, while the tail Gaussian also includes background like high energetic delta electrons, which received a high kinetic energy from the collision with the incident particle. These electrons cause a higher deviation in the residual of the detector. The residual of both detector layers is determined by the following parameters: w_i is the number of events covered by each fitted Gaussian and σ_i is the width of the respective Gaussian:

$$\sigma_{res} = \frac{\sigma_0^2 \cdot w_0 + \sigma_1^2 \cdot w_1}{w_0^2 + w_1^2}$$

As the two Gaussian distributions of the detectors are folded to another Gaussian, their individual residual width is determined by: $\sigma_{res} = \sqrt{\sigma_0^2 + \sigma_1^2}$

If both detectors are of equal design i.e. have the same spatial resolution $\sigma = \sigma_1 = \sigma_2$ the spatial resolution is then:

$$\sigma_{SR} = \frac{\sigma_1}{\sqrt{2}}$$

This can be assumed for the Eta layers of SM2. Due to beam divergence not all of the tracks through the detector are strictly perpendicular relative to the anode plane, σ_{res} thus is an upper limit for the spatial resolution of the detector.

3.5.2 Track Reconstruction and Efficiency definition

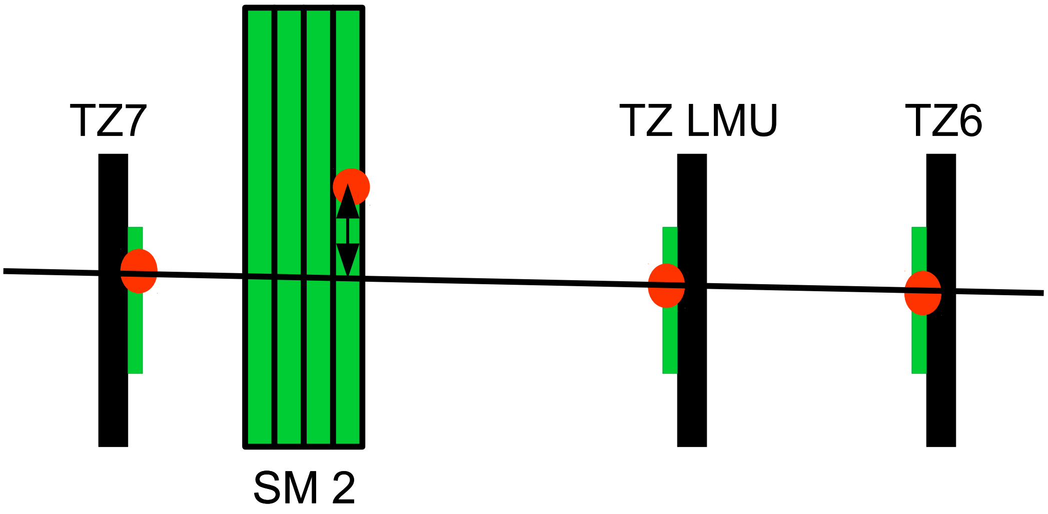

Figure 3.12: A sketch of the tracking fit and residual determination. The SM 2 detector is investigated for spatial resolution and efficiency, while the others are used for tracking. A line is fit through the hits in the detector, which is interpolated into the SM2 detector. The predicted residual is defined as the predicted position subtracted from the measured hit position.

If the particle hit position is measured several times along the beam line, a track can be defined through these detectors. The interpolated position of a detector is then compared to the measured hit position by the investigated detector to calculate a spatial resolution and efficiency (see fig. 3.12).

Because of the internal spatial resolution of the tracking detectors the accuracy of the track fit is limited. A hit is counted for the efficiency, if it is within 5σ of the residual fit. For the number of hits detected by the tracking telescope N_{tracker} and for the number of hits seen by the investigated detector N_{inv}, the efficiency is then:

$$\epsilon_{\%} = \frac{\text{hits}_{\text{inv}}}{\text{hits}_{\text{tracker}}}$$

3.5.3 Geometric Mean Method

For the following method it is necessary that all tracking detectors have the same operational parameters. The track spatial resolution for the tracking chambers was calculated by the geometric mean method that is independent of the distances relative to the detectors and gives a measure for the intrinsic spatial resolution [Carnegie et al., 2005].

$$\sigma_{SR} = \sqrt{\sigma_{in} \cdot \sigma_{ex}}$$

This is done via geometrical mean determination of the width of the residual distribution once including the detector under test in the fit (σ_{in}) and once excluding it from the fit (σ_{ex}).

3.5.4 Track Extrapolation Method

For the investigation of a detector with varying properties like gas, U_{amp} and U_{drift} the geometric mean method is not valid anymore, as the detectors do not have the same spatial resolution $\sigma_1 \neq \sigma_2$.
The exclusive residual width is determined from the weighted width of a double Gaussian (σ_{res}), with correcting for the track acuracy of the tracking telescope (σ_{track})

$$\sigma_{SR} = \sqrt{\sigma_{res}^2 - \sigma_{track}^2}$$

.

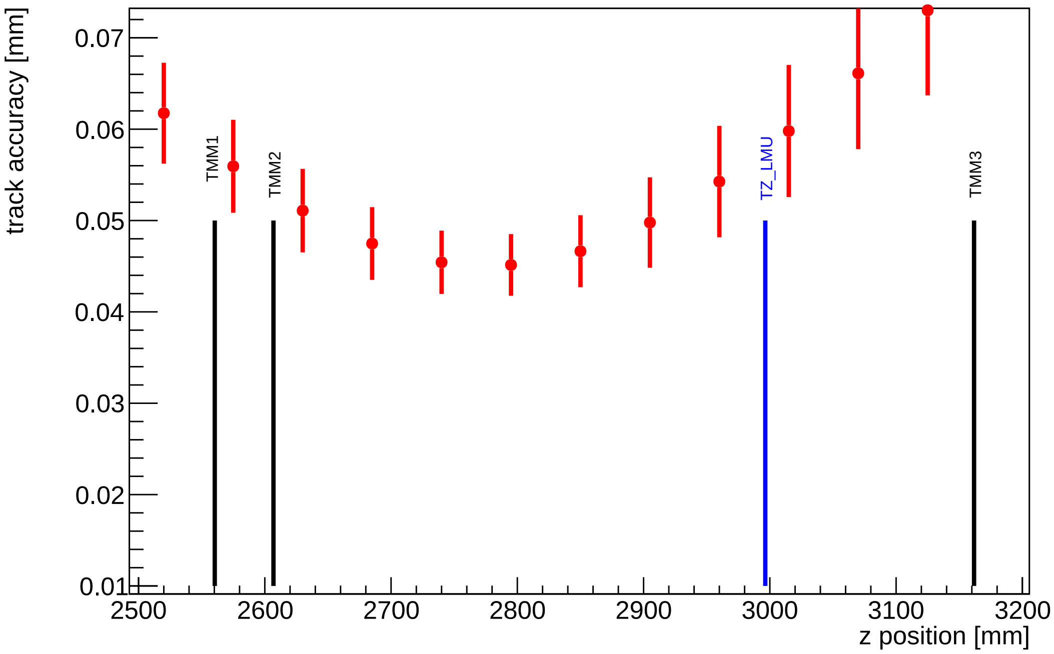

Figure 3.13: Calculation of the track accuracy [Horvat, 2005] (red) during the SPS test beam in June 2018. The track accuracy was determined with three resistive strip Micromegas (TMMs with black bars) with an internal spatial resolution $\sigma_{SR} = 78\mu m$. This results in an accuracy of $\sigma_{track} = 55\mu m$ at the position of the TZ_{LMU} (blue) which is a resistive strip chamber with zebra connectors.

In fig. 3.13 a calculation for the track accuracy for data of the SPS test beam in June 2018 is shown. The track accuracy has been determined at the position of the TZ_{LMU} chamber from the spatial resolution of the TMM chambers, which has previously been determined with the Geometric Mean method. It is calculated following a χ^2-minimization approach [Horvat, 2005].

3.6 Detector Alignment

For extendend experimental studies like for the SPS test beam (see chapter 5) with seven Micromegas detectors, it is hardly possible to position all of these detectors with mm precision in a short time. For this reason software alignment corrections are applied. In this thesis the x-coordinate is defined as direction along the precision coordinate of SM2, whereas the y-axis defined along the non-precision coordinate of SM2. The z-axis is the direction along the beamline.

3.6.1 Translation along X- or Y-Coordinate

The translation of two detector along x-and y-axis can be corrected by calculating the residual distribution between both. The mean of the distributions $\overline{x}$. can be directly interpreted as the shift between the detectors x_{diff}/ y_{diff}:

$$x_{diff} = \overline{x},\ y_{diff} = \overline{y}$$

3.6.2 Rotational Alignment along the Y- or X-Axis

A rotation between detector layers can be calculated via comparing the hit position to the residual distribution of a detector. For a rotation along the y-direction the hit position and residual in x will show a dependency (see fig. 3.14) and for rotations about the x-direction a dependency is found in y. If a linear correlation between the hit position and residual exists, the arctan(m) of the slope m has to be subtracted from the assumed angle. The correction Θ is thus given by

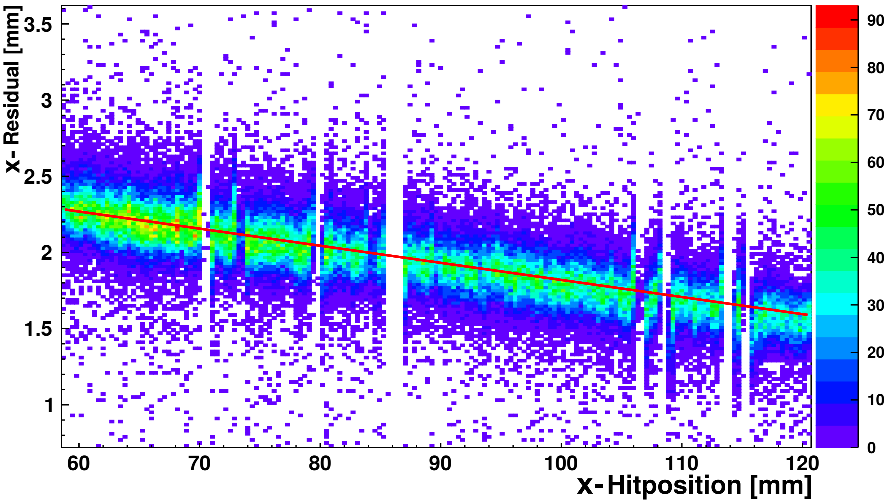

Figure 3.14: Hit position in$x$ plotted against the residual in x is shown for Eta_{In} for 100000 muons. The detector shows a dependence along the x-axis due to a rotation around the y-axis. The fit returns $m = 0.01 \pm 0.01$ and $p_0 = 3 \pm 2$. The rotation calculated is $\theta = 0.63°$.

$$\Theta = \arctan(m).$$

3.6.3 Displacement along the Z-Coordinate

A displacement m along the beam line leads to a correlation between the slope of the tracking telescope $\mathrm{a}_x(\mathrm{a}_y)$ and the residual Δx (Δy)

$$\Delta x_i(a) = m \cdot a_x + t.$$

If the detector is not displaced, the plot is independent of the slope predicted by the trackers as shown in figure 3.15.

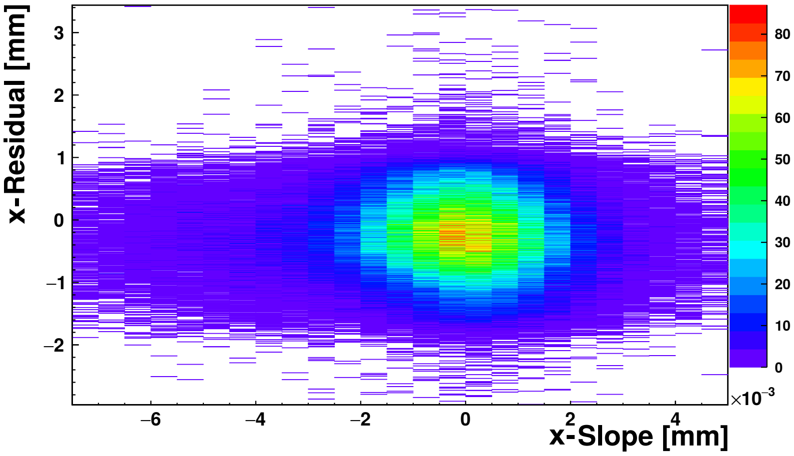

Figure 3.15: Residual in x as a function of the predicted track slope for the $\mathrm{Eta}_{\mathrm{In}}$ layer of SM2, which has been aligned correctly along the z-axis and does not show any dependency.

Chapter 4

Investigation of a 10x10 cm^2 Micromegas using 22 MeV Protons

This chapter describes tests that were performed with a 10x10 cm^2 sized Micromegas chamber equipped with a VMM3 MMFE8 card and filled with Ar:CO$_2$ 93:7 vol% at the Tandem accelerator facility situated in Garching. Measurements have been performed with 22 MeV protons. A low material budget GEM (Gas Electron multiplier) detector [Sauli, 1997] was used to trigger the acquisition as the protons can pass through the low material budget detector. Amplification and drift voltage scans were performed at an inclination of $(21 \pm 1)^\circ$.

4.1 Experimental Setup

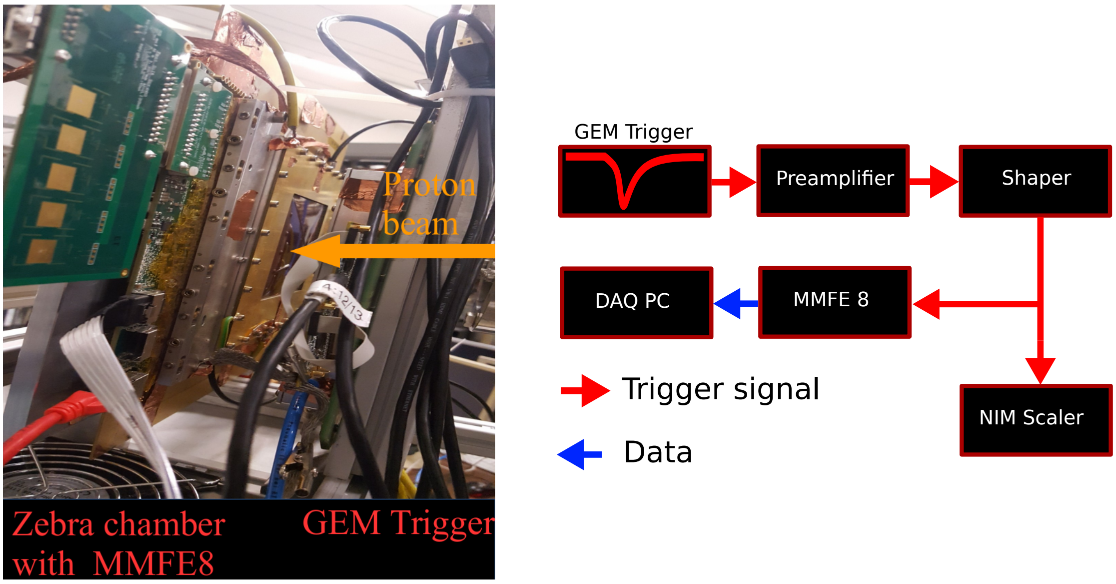

Figure 4.1: Left: The detector setup. The 10x10 cm^2 Micromegas is equipped with a VMM3 MMFE8 board. Right: The trigger setup during the test beam. The GEM is used for triggering.

The setup of the test beam is shown in fig. 4.1. The charge signal of the GEM detector is fed into a preamplifier, which converts the pulse into a voltage signal with a fast rise ($\mathcal{O}(100\,ns)$) and a slow exponential return tail to the baseline ($\sim 75\,\mu$s). The shaper changes the voltage signal to a pulse with well defined amplitude and timing.
A low threshold discriminator converts the charge pulse into a NIM-standard logic pulse, if it exceeds a certain threshold. In the last stage the signal is extended to 10 μs. The signal is then fed into the MMFE8 board as trigger.
For the VMM setting a gain of 6 fC/mV, a peak time of 200 ns and a threshold of 200 DAC counts were used.
The readout was performed with the L0 mode (see sec. 2.2.4). The L0 rollover was chosen as 4040 and the trigger window as 4095. The neighbor logic was activated. This gives a total difference between the trigger arrival and signal arrival at the VMM chip of 55 cts·25 ns= 1375 ns. It is important to set this time difference correctly. If the time of the trigger arrival and the signal arrival differs too greatly ($\mathcal{O}(100\,\text{ns})$) the data are discarded by the L0 buffer, as it is outside of the L0 acceptance window (see sec. 2.2.4).
For the readout with the MMFE8 a bulk resistive strip Micromegas chamber was used. It has an amplification gap width of 105 μm and a drift gap width of 5 mm.

4.2 Cluster Charge Dependence

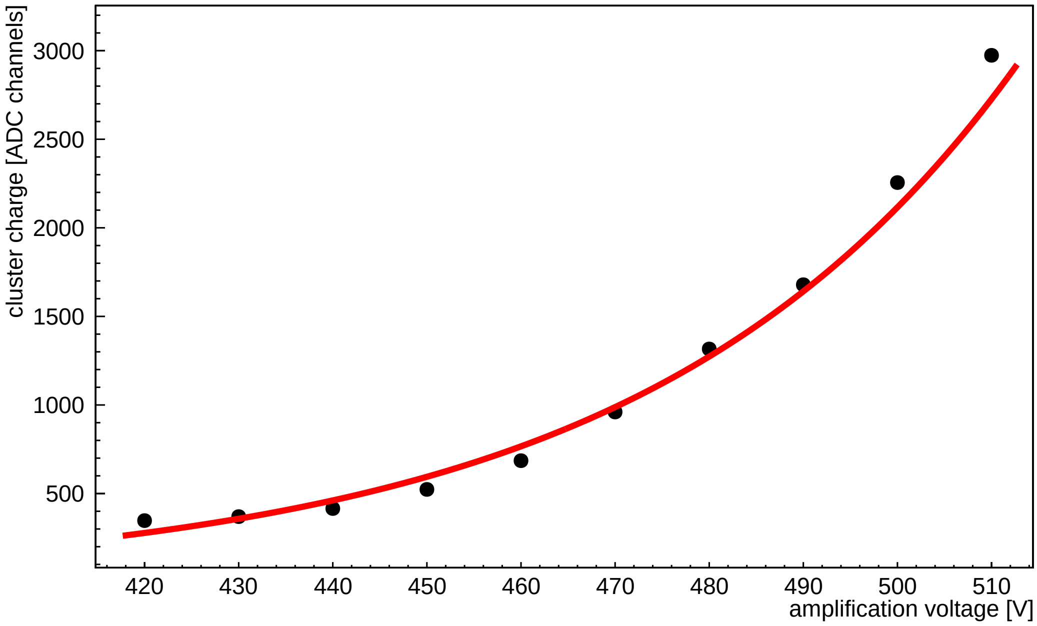

Figure 4.2: The MPV of the cluster charge distribution as a function of the bulk chamber's amplification voltage. As theoretically predicted the amplification voltage shows an exponential increase due to the by Townsend predicted avalanches. The parameters of the exponential fit $\exp(c + ax)$ are for the constant $c = -5.03 \pm 0.02$ ADC counts and for the slope $a = (2.538 \pm 0.006) \cdot 10^{-2}$ ADC counts/V. The error bars are not visible as the error is in the orders of 10 ADC channels.

The MPV of the cluster charge for the amplification scan determined as demonstrated in sec. 3.2 via a Landau fit is shown in fig. 4.2. As expected from theory the cluster i.e. the gain rises exponentially with the amplification field.

The pulse height/ cluster charge is proportional to the gas gain $G = \exp(\alpha \cdot d)$, with

$$\alpha = A_0 \cdot n \cdot \exp(-\frac{B_0 * n}{E_{\mathrm{amp}}}) .$$

A_0 and B_0 are parameters of the gas, n is the particle density in the gas and E_{amp} is the electric field in the amplification gap [Townsend, 1910] and [Adloff et al., 2009].
For $\mathrm{U}_{\mathrm{amp}} = 510\,\mathrm{V}$ the cluster charge distribution (see fig. 4.3) is more deformed towards a Gaussian shape, where the distribution for 500 V is more Landau-like. It is possible that events with a high cluster charge also feature strips with a high charge. These strips eventually exceed the dynamic range of the VMM.

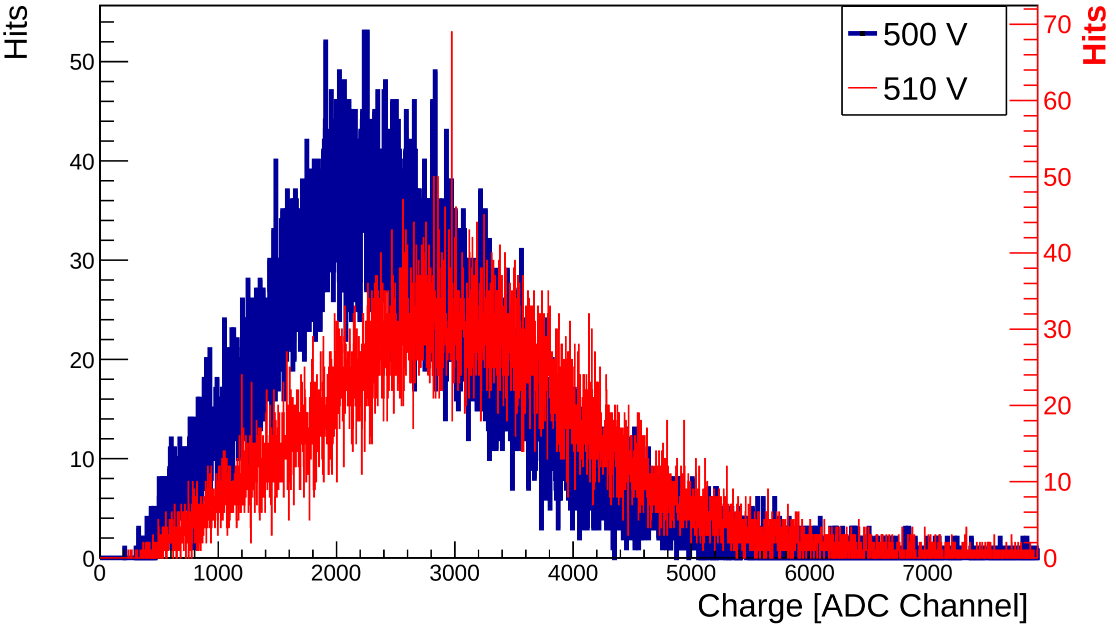

Figure 4.3: The cluster charge for amplification voltages of $\mathrm{U}_{\mathrm{amp}} = 500\,\mathrm{V}$ and 510 V. For 500 V a Landau distribution is visible, which transforms more into a Gaussian shape for 510 V.

This hypothesis is supported also by observing the number of entries in the overflow bin of the strip charge distribution (see table 4.1) i.e. a larger fraction where the strip charge exceeded the dynamic range of the ADC of the chip. Between $\mathrm{U}_{\mathrm{amp}} = 500\,\mathrm{V}$ and 510 V the number of hits in the overflow are more than doubled.

$\mathrm{U}_{\mathrm{amp}}$ [V]	Hits	Hits in the overflow	% of overflow hits
490	295 k	4 k	1.4
500	300 k	12 k	4.0
510	330 k	31 k	9.3

Table 4.1: Number of detected strips and fraction of the strips marked as overflow by the VMM chip during data taking.

Another important property of the cluster is the strip multiplicity. It is dependings on the angle of inclination as well as the diffusion of the detector gas mixture. The mean of the strip multiplicity (see fig. 4.4) increases starting at 4.1 strips at 420 V to 7 strips at 500 V. For higher amplification voltages (above 500 V) the strip multiplicity reaches 7 strips/cluster.

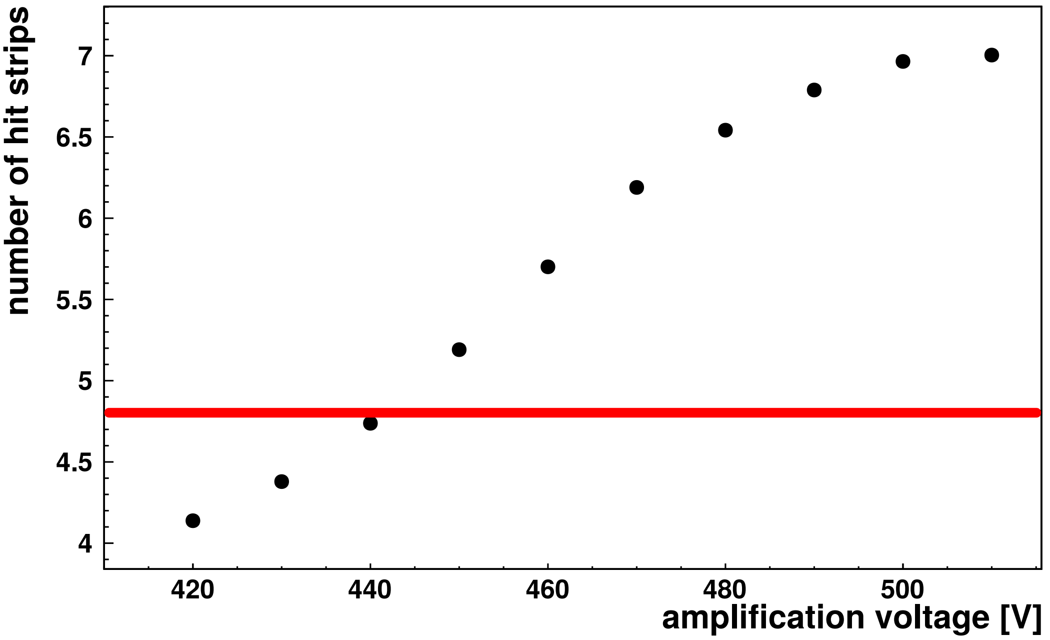

Figure 4.4: Mean number of strips in the leading cluster as a function of the amplification voltage. A plateau is reached for $U_{amp} \geqq 500$ V. The geometrically calculated cluster multiplicity of 4.8±1.2 strips is indicated by a red line.

The hit multiplicity n in a cluster can be calculated using the length of the drift gap $d = (5 \pm 0.2)\,\text{mm}$, the incident angle $\theta = (21 \pm 1)^\circ$ and the pitch $p_s = 0.4\,\text{mm}$:

$$n = \frac{d}{p_s} \cdot \tan(\theta) = \frac{5\,mm}{0.4\,mm} \cdot \tan(21^\circ) = 4.8 \pm 0.4$$

As the reconstructed cluster multiplicity differs by around two strips from the expectation, capacitive coupling leads to a higher amount of strips than calculated by the formula above. Capacitive coupling at the borders of the cluster virtually increases the multiplicity, if the strip is read out via the neighbor logic even though it did not cross the channel specific threshold. This leads to two more strips/cluster reconstructed by the measurement (7) on average than calculated (4.8 ± 0.4).

4.3 Angular resolution

The reconstructed angles and angular resolutions of the detector and the readout electronics can be determined by using the μTPC method as explained in sec. 3.4.3. The drift velocity for the chosen drift fields has been simulated with MAGBOLTZ and have been measured directly (see fig. 4.5).

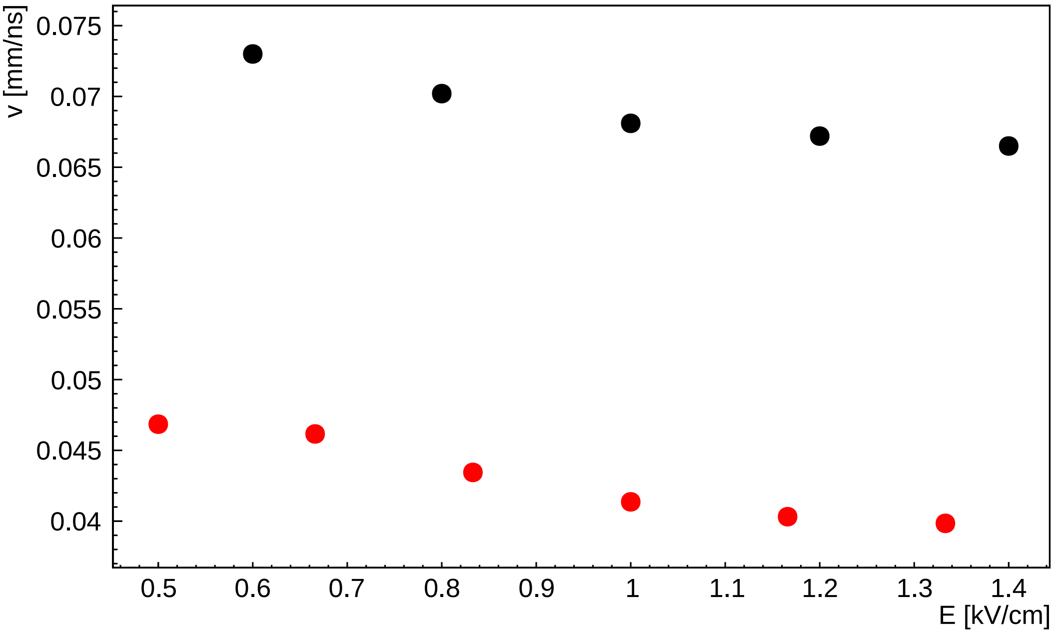

Figure 4.5: The measured drift velocity for Ar:CO_2 93:7 vol% as a fit of the drift voltage, measured (black) and simulated drift velocities (red). The trend is the same for both velocities, but a difference of $0.025 \frac{mm}{ns}$ exists. The data points of the simulation differ slightly on the x-axis.

The measured drift velocity shows the same behavior as the simulated one. However, the measured drift velocity is about $25 \frac{mm}{ns}$ higher than the simulated drift velocity. The drift velocity depends on the drift time of the electrons Δt and the drift gap d. Deviations of more than 0.5 mm for the drift gap are unlikely, as then the geometrically calculated cluster multiplicity 4.8 strips/cluster would differ too much from the measured one. Also considered were simulations of small gas admixtures of H_2O and O_2. The impact of the simulated deviation for the drift velocity, however, is not comparable for small admixture below 10% to the measured drift velocity. It is probable that the time was calibrated in the wrong manner.
For the scan of amplification and drift voltages the reconstructed angle and angular resolutions were determined (see fig. 4.6 and fig. 4.7). The incidence angle was adjusted to $(21\pm1)^\circ$. At the first two values $U_{\mathrm{amp}} = 420\,\mathrm{V}$, $430\,\mathrm{V}$ with $U_{\mathrm{drift}} = 250\,\mathrm{V}$ the reconstruction yields a value of $\theta = (26^{+10}_{-6})^\circ$. At these values the number of reconstructed events is few, $\mathcal{O}(2000)$, leading to a high error and low angular resolution because the signals are too small. The reconstructed angle decreases to 24° with a better angular resolution of $(^{+6^\circ}_{-4^\circ})$. For the drift scan with an amplification voltage $U_{\mathrm{amp}} = 470\,\mathrm{V}$ the angular resolution stays constant at an angular resolution of $(^{+6^\circ}_{-4^\circ})$. The reconstructed angle however increases to 25° in comparison to the adjusted angle of 21°, as the drift velocity used is wrong.
The most probable angle is strongly depending on the drift velocity for the electrons (see sec. 3.4.3).

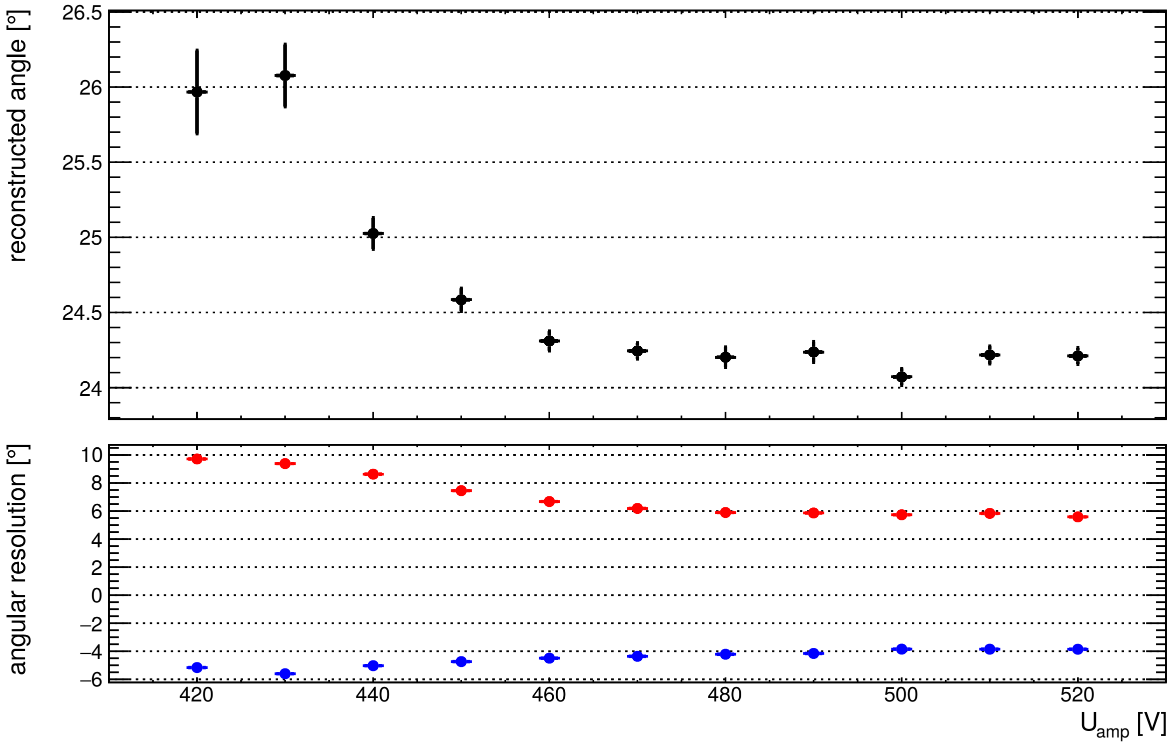

Figure 4.6: Angular resolutions for the amplification scan for an angle of (21±1)°. The reconstructed angle and angular resolution decrease and reach a plateau at $U_{\mathrm{amp}} = 470\,\mathrm{V}$ with $\theta = (24^{+6}_{-4})^\circ$.

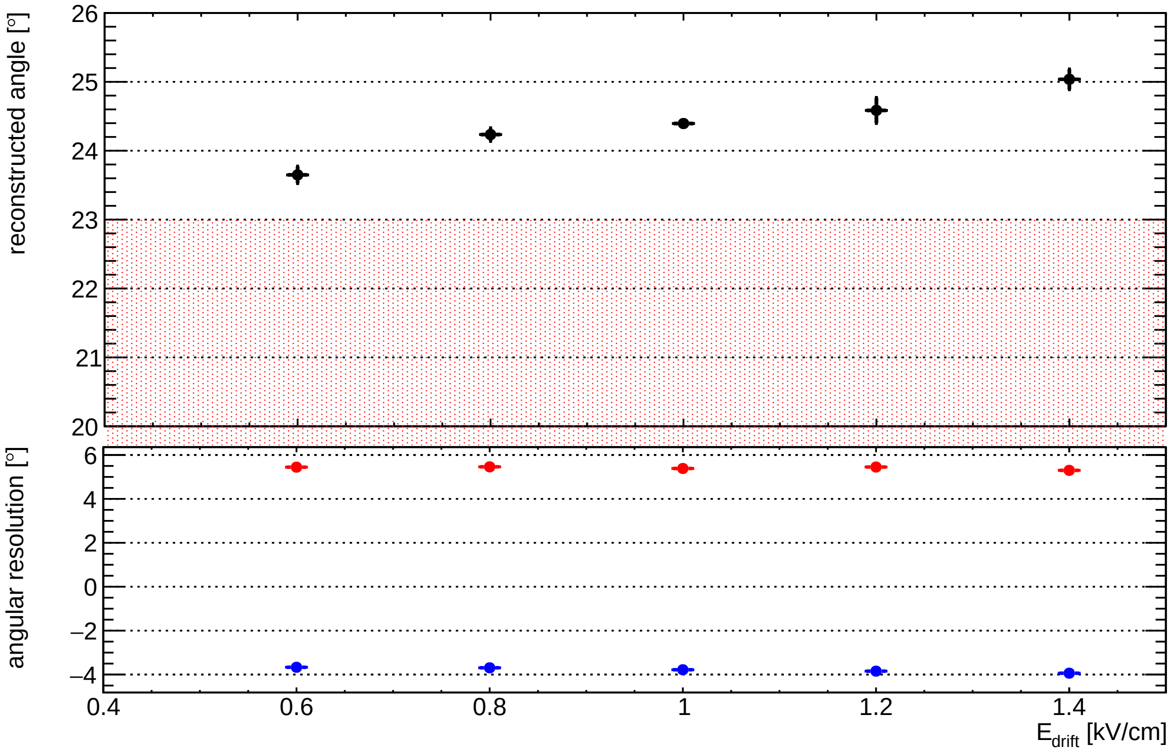

Figure 4.7: The angular resolution for an angle of (21±1)° as a function of the electrical field in the drift gap. The upper plot shows the reconstructed angle and the plot below shows the small and large σ of a Gaussian fit used for the determination of the angular resolution. For large drift fields the angle increases to a value of $(25^{+6}_{-4})^\circ$. The angular resolution stays constant.

As clearly visible the measured drift velocity differs greatly from the simulated velocities, and thus this difference in the reconstrcuted angle can be understood (see fig. 4.5). For variation of the drift voltage the reconstructed most probable angles were compared using the simulated drift velocities and the measured values for the drift velocities (see fig. 4.8).

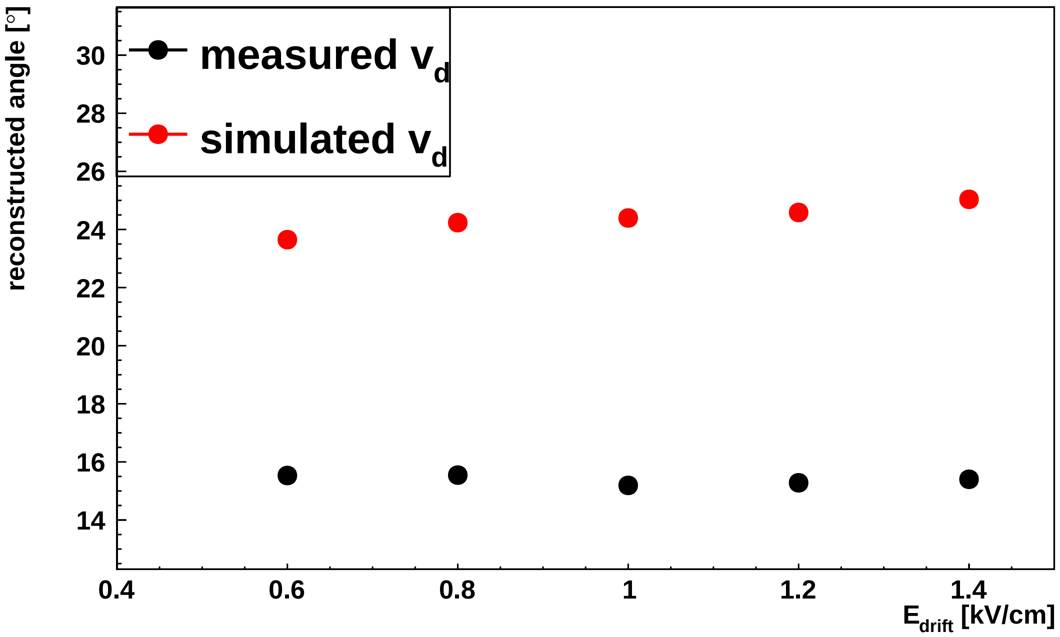

Figure 4.8: The reconstructed angle as a function of the drift field using simulated and measured drift velocities V_d. Both drift velocities lead to a wrong reconstruction for the experimental angle $\theta = (21 \pm 1)°$.

Both methods produce angles, that are not in agreement with the experimentally determined angle of 21°. As the measured drift velocity is determined at an angle $\theta = 15°$, it is possible that the time calibration fails to determine the right drift time for the electrons. The simulated drift velocity v_d reconstructs a most probable angle much closer to the measured angle $\theta = (21 \pm 1)°$ than the measured value. This is expected due to capacitive coupling and thus strips sharing charge at the borders of a cluster and thus influencing the μTPC track reconstruction. This leads to an increased reconstructed angle.

4.4 Summary

The main motivation for the studies in this chapter was to investigate the operating principle of the VMM on a 10x10 cm^2 Micromegas detector. The studies performed at the Tandem accelerator produced exponentially rising pulse heights in agreement with the theory. The cluster multiplicity tends to be too high by 2 strips per cluster (expected: 4.8±0.4, reconstructed: 7.12±0.02) because of the neighbor logic of the chip.
The drift voltage scan shows a minimum reconstucted angle of 23°, which is out of the range of the adjusted angle $(21 \pm 1)°$ because a too low drift velocity was used to calculate the angle with the μTPC approach. For the angular resolution satisfying values of $(^{+6°}_{-4°})$ can be achieved with the small 10x10 cm^2 Micromegas from a 5 mm drift gap. The reconstruction for the angular resolution, thus, worked very well.

The reconstructed angles for the drift scan exhibited major differences between the experimental angle and the ones determined by the measured/simulated drift velocities. The reconstruction of to high angles with the simulated drift velocities can be explained by capacitive coupling.

For the measured drift velocity this effect is not yet understood. Also considered were humidity and pollution of gases. These are not a valid explanation, as H_2O would decrease the drift velocity. An admixture of air would, indeed, lead to an increase of the drift velocity. However, as the simulated and measured velocities differ by nearly double the drift velocity, a small fraction of pollution can not explain this behavior.

Chapter 5

Investigation of a 2 m^2 Micromegas Quadruplet using 20 to 150 GeV Muons and Pions

In June 2018 the performance of the SM2 Module 1 was investigated in combination with close to final NSW front-end electronics at the Super Proton Synchrotron (SPS) H8 Beam Line at CERN (see fig. 5.1). The SPS is a preaccelerator of the LHC injecting accelerated protons of energies of $E_{SPS} = 450\,\mathrm{GeV}$ into the LHC or the Northern Area H8 beam line used for detector performance tests [CERN, 2019].
The studies performed included the determination of cluster multiplicity, cluster charge, spatial resolution and efficiency. The varying parameters of the NSW module were different Ar:CO_2 gas mixtures, different inclination angles in respect to the SM2 readout plane and different amplification/drift voltages.

5.1 Setup

The setup consisted of four 9x10 cm^2 scintillators, which were used to generate the trigger signal for the readout electronics. The tracking detectors were three bulk Micromegas chambers (TZ) equipped with MMFE8 boards and three 2D resistive strip Micromegas (TMM) equipped with APV25 hybrids boards interfaced by the SRS.
The majority of the measurements were recorded using the MMFE8 detectors only. The detector properties are listed in table 5.1. The TMMs feature an amplification gap of 100μm and a drift gap of 5 mm. The nominal amplification voltage for TMMs was 550 V and for the TZ chamber 530 V. The nominal drift voltages were chosen 300 V.
The readout with the APVs allowed for a 2D information from the trackers. All of the detectors other than SM2 were operated using an Ar:CO_2 93:7 gas mixture. An event is accepted, if three tracking detectors have registered a hit consecutively.

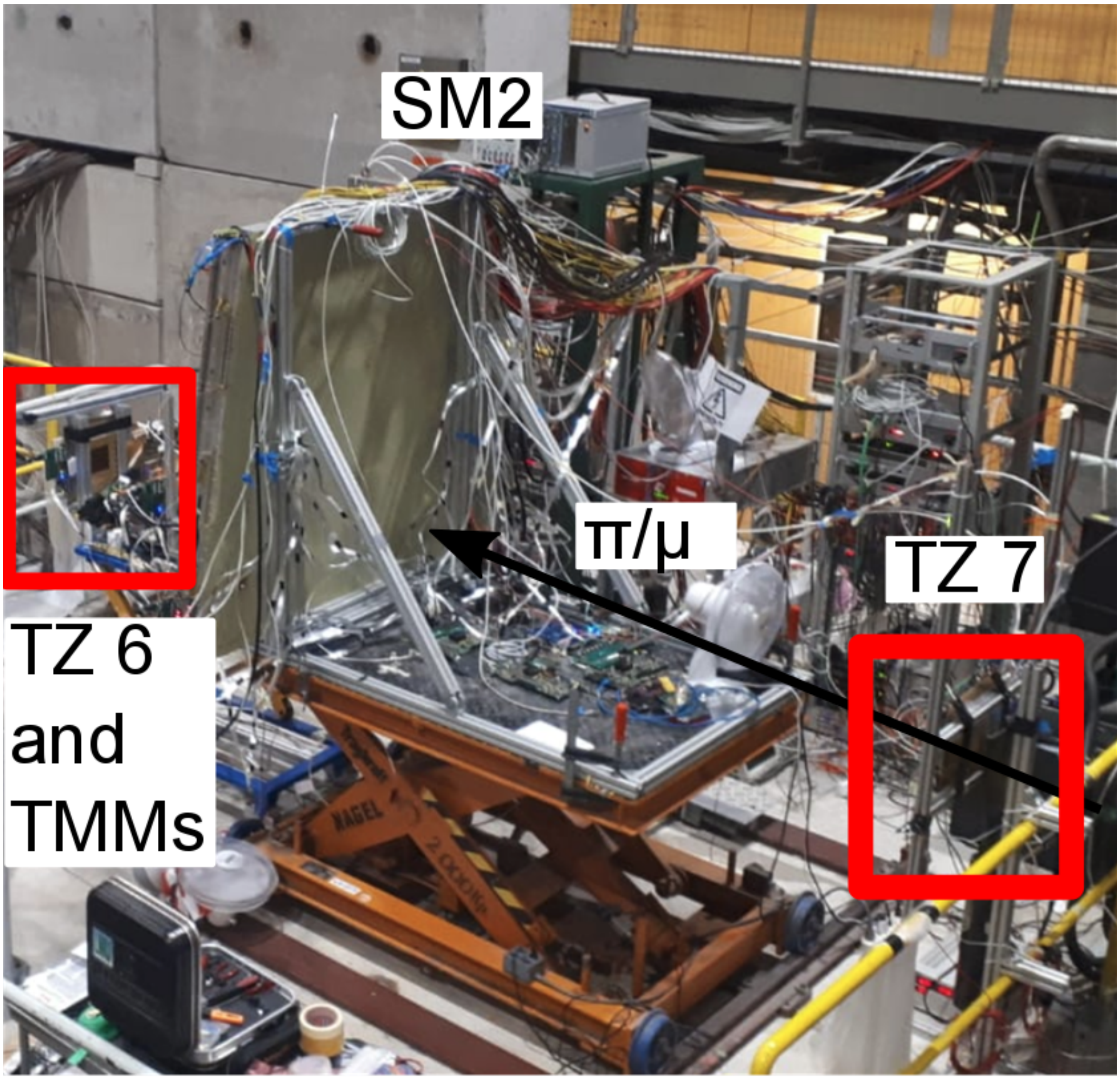

Figure 5.1: Setup of the SPS test beam. The MMFE8 tracking chambers and the SM2 module under test are visible. The TMM tracking telescope is situated behind the SM2 Micromegas module. High energetic muons or pions pass through all the detectors. The whole setup is shown in fig. 5.2.

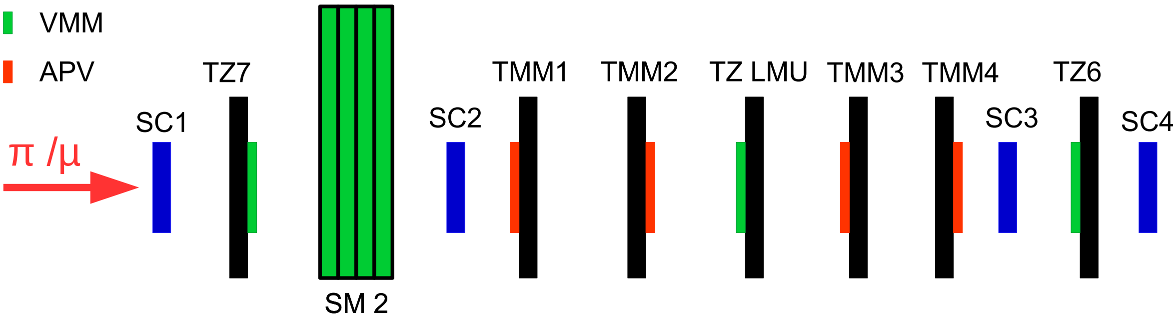

Figure 5.2: Setup of the SPS test beam. The tracking detectors used were the TZ chambers and TMM chambers. For the frontend electronics the VMM was used for all detectors except for the TMMs, which were equipped with APV electronics. The scintillators used fot he trigger signal are indicated in blue.

	TMM 1-4	TZ_{LMU}	$TZ_{6/7}$	SM2 M1
layers	x;y(2)	x(1)	x(1)	x (Eta/ Stereo, 4); y (Stereo, 2)
amp. gap [μm]	100	105	100	120
amp. voltage [V]	550	530	530	varying ($U_{WP} = 580$)
drift gap [mm]	5	5	5	5
drift voltage [V]	300	300	300	300
pitch [mm]	0.25	0.4	0.4	0.425

Table 5.1: Properties of the detectors that were used in the setup. The number in brackets is the amount of detector layers.

The SM2 chamber was positioned perpendiculary as well as at 20° and 30° with respect to the particle beam. The beam hit the module in the largest PCB in the right sector (6) (see fig. 5.3).

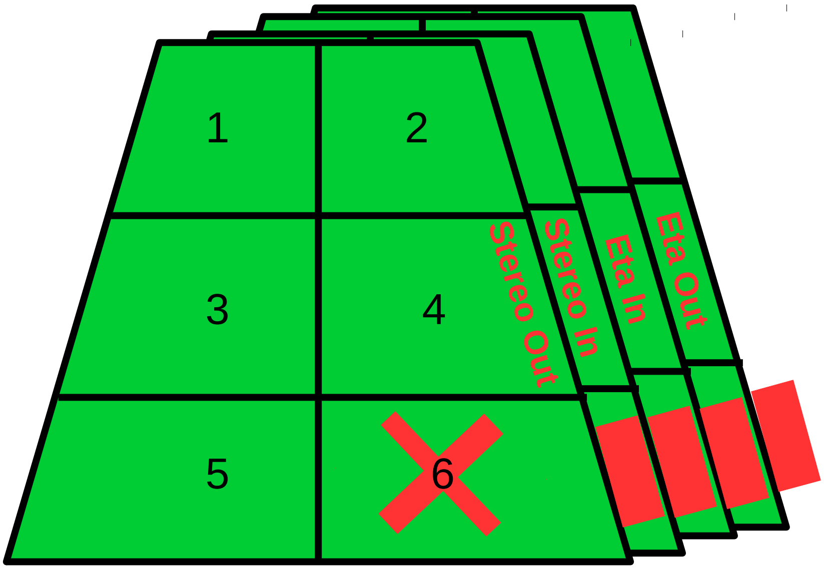

Figure 5.3: Sketch of the SM2 layers including the HV sectors. Only the sector hit by the beam was equipped with the MMFE8 boards (red). The beam incided at the position of sector 6.

The particle beam consisted out of high energy muons from 20 to 150 GeV as well as pions depending on the measurement. The rate was in orders of $\mathcal{O}(50\,\mathrm{kHz/cm^2})$ for pions and for muons $\mathcal{O}(\mathrm{Hz/cm^2})$.

5.2 Readout Chain

As mentioned the TMMs were equipped with APV25 and the TZ chambers with VMM chips. For the VMMs an aggregator card is used to distribute the trigger, synchronize hits and receive a veto from the FEC for the combined VMM/APV readout. About 25% of the events were discarded during the first analysis step due to later on resolved firmware issues. The trigger was derived from the coincidence of two scintillators placed in front and behind the Micromegas detectors.

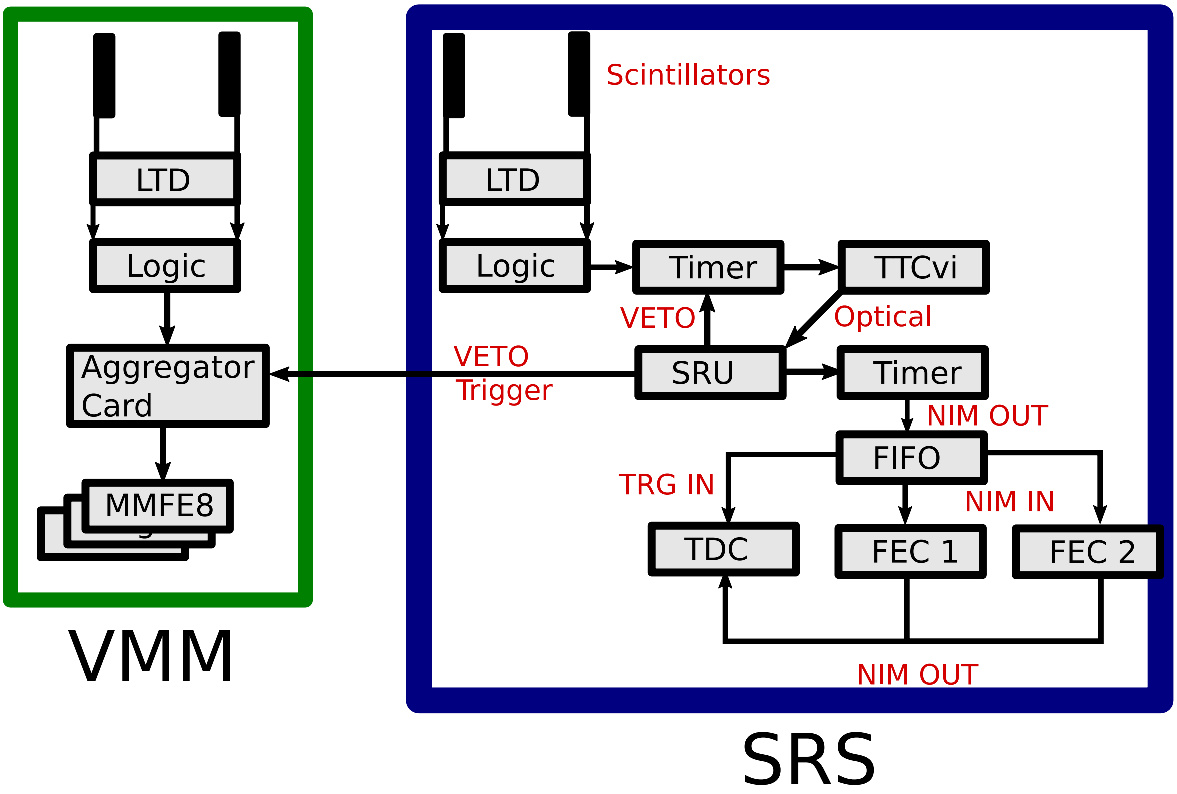

Figure 5.4: The combined SRS (blue) and VMM (green) trigger setup for the SPS test beam. The scintillator signal is sent via a NIM-standard signal to the aggregator card and the timer.

Data was aquired in the L0 mode of the VMM. The gain was chosen at 9 mV/fC and the peak time was 200 ns. The VMM was also operated with a thresholds of 8 times the root mean square of the electronic noise counts, bipolar shape and neighbor logic activated [Koulouris, 2019].

The APV25 trigger setup is shown in figure 5.4. The scintillators send an analog voltage signal, which is converted into a digital signal if the threshold surpasses the trigger threshold. A coincidence unit compares, if two trigger signals arrived at a similar timing and sends the trigger signal to a timing unit. The SRU sends a veto signal to the timer until the FECs have been read out and data taking is finished. The SRU sends the signal via a timer to the FECs activating the readout and sends a signal to the TDC to allow for the offline correction of the 25 ns time jitter inflicted by the SRS.

5.3 Combined VMM/APV Readout

If the SRS vetoes the trigger for the VMMs, a combined measurement can be performed. As the VMM can handle a much higher data rate in comparison to the SRS-APV25 a veto for the readout is necessary. Otherwise the APV and VMM events can not be correlated to each other.

Recorded events have to be combined with respect to their trigger counter, which is stored in the raw data.

Furthermore, in the APV25 raw data, only the peak value and its timing are processed by the custom made script. The APV25 data is then saved in the same format as the VMM data to simplify the analysis.

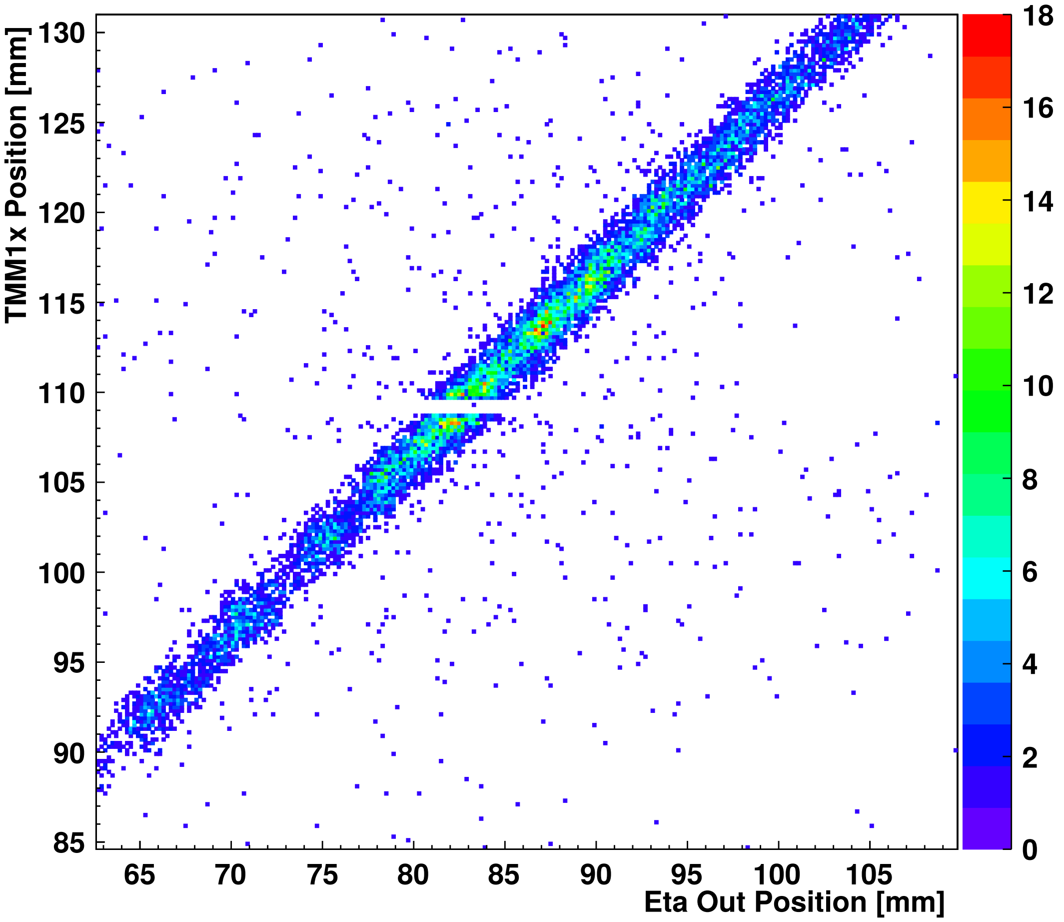

Figure 5.5: Reconstructed hit position in TMM1x as a function of the hit reconstructed in Eta $_{\text{Out}}$. As a linear correlation is observed, the merging between the two data streams was successful.

If the merging between the two data streams has been successful, a linear correlation between the APV25 and VMM readout for the hit position is expected. This is indeed the case as demonstrated in figure 5.5, where it is shown for the Eta$_{\text{Out}}$ layer of SM2 (VMM) and TMM1 (APV25).

5.4 Cluster Charge and Strip Multiplicity Dependence

5.4.1 Comparison of the Tracking Bulk Chambers

The VMM tracking detectors were scanned in regard to the amplification voltage to find the optimal amplification voltage to use during the tests with the SM2 Module 1. Each tracking detector was filled with an Ar:CO$_2$ 93:7 vol% gas mixture. The cluster charge was measured for different amplification voltages (see fig. 5.7). The expected exponential rise is visible.

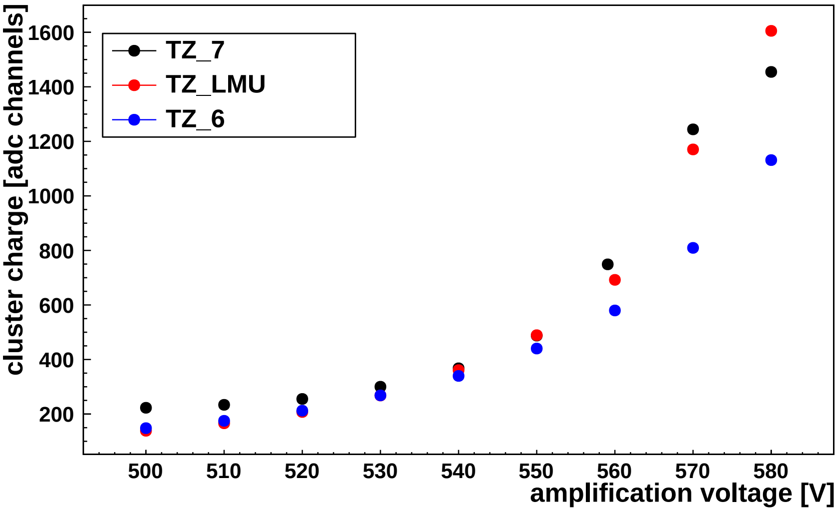

Figure 5.6: The MPV of the cluster charge distribution for the VMM tracking chambers as a function of the amplification voltage. For voltages higher than 550 V the values differ up to 50%.

The readout electronics exhibit saturation beginning at voltages of 550 V (see fig. 5.7). The cluster charges exhibit still a Landau-like shape with a second peak at values of 2200 ADC channels at U$_{\mathrm{amp}}$ = 550 V.
For U$_{\mathrm{amp}}$ = 580 V the shape is completly deformed. In the strip charge for the leading cluster this behavior is visible in form of a high fraction of hits filled into the overflow bin (for U$_{\mathrm{amp}}$ = 550 V 10% and for U$_{\mathrm{amp}}$ = 580 V 23%). For this reason the amplification voltage was set to 540 V.

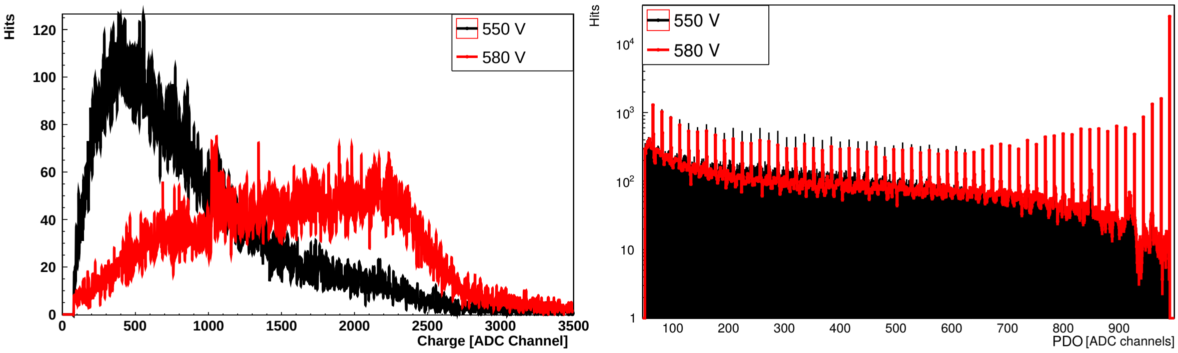

Figure 5.7: Left: Deformed cluster charges due to saturated readout electronics. Right: The strip charge of strips in the leading cluster of the TZ$_{\mathrm{LMU}}$ for U$_{\mathrm{amp}}$=550 V and 580 V for 130000 events. The overflow bin is filled with 10000 events for 550 V and 28000 for 590 V.

The discrepancy for the cluster charges of the TZ chambers can be explained by comparing the strip charge of these chambers (see fig. 5.8). The PDO of the $\mathrm{TZ_{LMU}}$ starts at 0 ADC channels, whereas the other two tracking chamber's PDOs begin at 100 ADC channels. This is a sign, that the threshold was chosen too high for these chambers. The high difference in the cluster charge between the $\mathrm{TZ_6}$ and $\mathrm{TZ_7}$ might be caused by a higher noise level in the $\mathrm{TZ_7}$ chamber thus leading to a higher threshold.

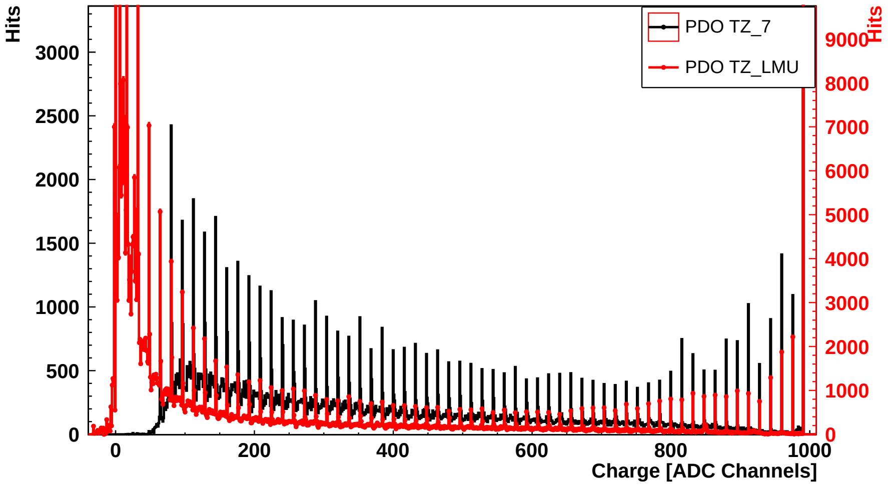

Figure 5.8: Strip charge of $\mathrm{TZ_7}$ and $\mathrm{TZ_{LMU}}$ at an amplification voltage of 570 V. The distribution of $\mathrm{TZ_{LMU}}$ starts at around 0 ADC channels ,whereas the $\mathrm{TZ_7}$ is starting around 50. The strip distribution for TZ_6 looks similar to $\mathrm{TZ_7}$.

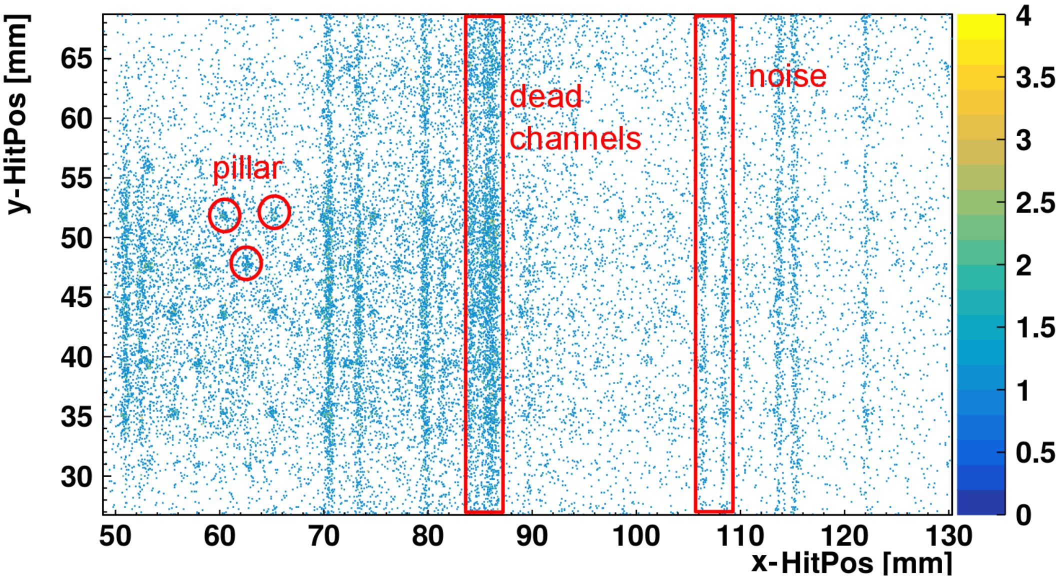

Figure 5.9: Inefficiencies along x- and y-axis for the $\mathrm{TZ_7}$ detector at $\mathrm{U_{amp}} = 530\,\mathrm{V}$. The detector has expected inefficiencies at the pillar and shows additional inefficiencies at certain VMM channels, which lead to worse track reconstruction. The non-precision coordinate is reconstructed by y-layers of the TMM detectors.

This can be seen in the inefficiencies of the TZ_7 chambers (see fig. 5.9). The hit position along the x-axis was directly measured, whereas the hit position along the y-axis has been reconstructed via the APV25 tracking detectors.

In this plot the pillars of the detector, high noise and non-efficient VMM channels are visible.

In the beam spot are about eight not responding channels, which could be caused by a faulty connection to the detector. At the pillars inefficient spots are expected, as here no gas amplification can happen. Because of the not responding channels and the noise exhibited it is possible that the tracking reconstruction is worsened. This is due to the high lever arm, as the TZ$_7$ detector is two meters in front of the SM2 module (see fig. 5.2).

5.4.2 Comparison of the SM2 module and a 10x10 cm^2 Micromegas

The SM2 chamber and a 10x10 cm^2 Micromegas (TZ$_{\mathrm{LMU}}$) have been compared in an amplification scan (see fig. 5.10) with Ar:CO$_2$ 93:7 vol%. For the smaller Micromegas chamber amplification voltages between 500 and 540 V were chosen and for the SM2 the amplification voltage was chosen between 540 and 580 V.

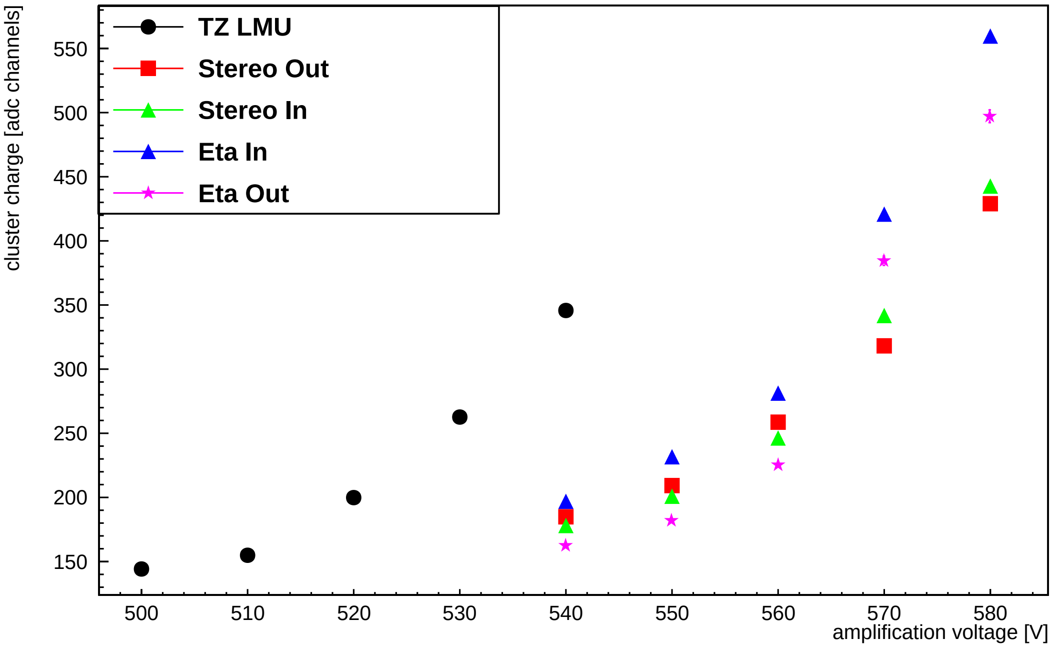

Figure 5.10: Cluster charge for TZ$_{\mathrm{LMU}}$ and the four layers of the SM2 module. A clear difference in cluster charge is visible for these two detectors as well as deviation between the individual layers for higher voltages.

Each layer of SM2 and the 10x10 mm^2 Micromegas shows an exponential-like increase. Due to the smaller pillar height of 105 μm in comparison to the SM2 layers with ca. 120 μm the cluster charge is higher for the bulk Micromegas with the same VMM settings.
Also it is visible that the cluster charge differs for the SM2 layers at higher voltages starting at $U_{\mathrm{amp}} = 570$ V with a maximum difference of 22% at $U_{\mathrm{amp}} = 580$ V for the Eta$_{\mathrm{In}}$ and Stereo$_{\mathrm{Out}}$ layer. To explain this trend the difference in the pillar height was investigated for a correlation with the gain of the individual layers. For $U_{\mathrm{amp}} = 580$ V the pillar height in correlation to the cluster charge is shown for the individual layers of SM2 (see fig.5.11). Here only a dependence is visible for Eta$_{\mathrm{In}}$ and Eta$_{\mathrm{Out}}$ and for Stereo$_{\mathrm{In}}$ and Stereo$_{\mathrm{Out}}$. Between the Eta and Stereo layers a correlation in the pulse height is not visible.
If a correlation between pulse height and pillar height exists, the gain difference caused by the pillar height and pulse height should be the same. The pillar height was determined by quality control measurements at CERN.

The gas gain can be calculated (with α: Townsend coefficient and h: pillar height of the detector) by $G = \exp(\alpha h)$. The dependence of the Townsend coefficient [1] on the amplification field is linear and has been extrapolated to an amplification field of 48-50 kV/cm field from a simulation (see Klitzner [2016]). Thus the Townsend coefficient can be calculated by coefficient α with the slope a, intercept b, amplification voltage $\mathrm{U_{amp}} = 580\,\mathrm{V}$ and the pillar height h_p:

$$\alpha = a \cdot \frac{U_{\mathrm{amp}}}{h_p} + c = 21.9\frac{1}{\mathrm{kV}} \cdot \frac{0.580\,\mathrm{V}}{h_p} - 401.1\,\mathrm{cm}^{-1}.$$

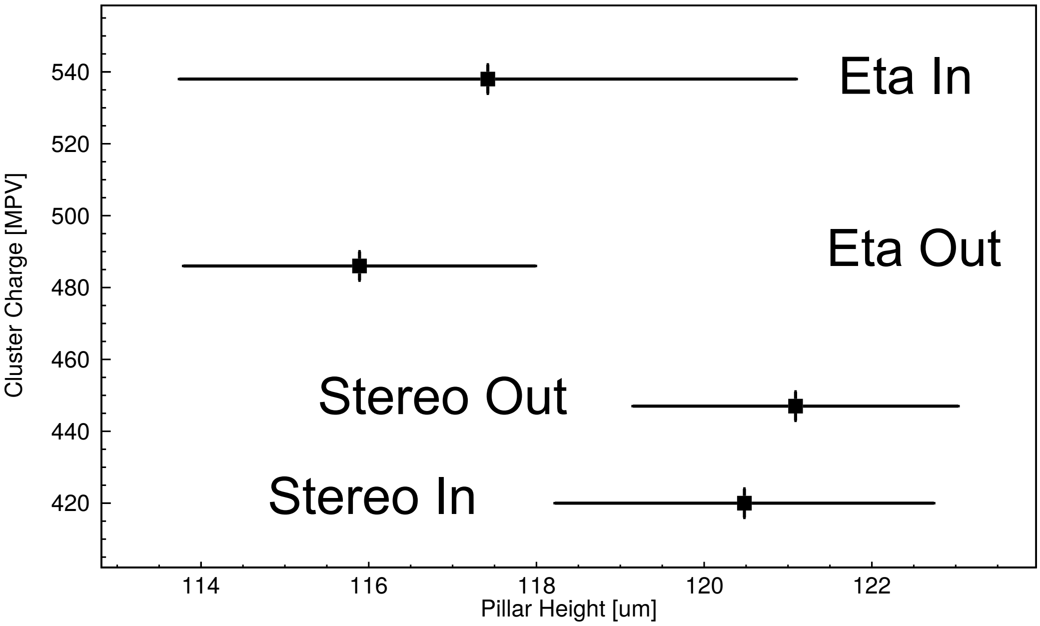

Figure 5.11: The MPV of the cluster charge distribution for all layers of SM2 as a function of the pillar height at a voltage of 580 V. A dependence on the pillar height is visible for $\mathrm{Eta_{In}}$ and the Stereo layers. $\mathrm{Eta_{Out}}$ has a too high cluster charge compared to the pillar height. The pillar heights have been determined by quality control measurements at CERN.

For a voltage of $\mathrm{U_{amp}} = 580\,\mathrm{V}$ the theoretical gain at the measured pillar height and measured pulse height were compared. The pillar heights, calculated Townsend coefficient and calculated gain in comparison to the measured cluster charge are shown in table 5.2.

Layers	$\mathrm{Eta_{In}}$	$\mathrm{Eta_{Out}}$	$\mathrm{St_{Out}}$	$\mathrm{St_{In}}$
h_p [μm]	117 ± 4	116 ± 2	121 ± 2	120±2
α [cm^{-1}]	658.2	694.0	648.0	656.8
$G = e^{\alpha p_h}$	3032	3135	2542	2648
c.c. [ADC counts]	538±4	486±4	447±4	420±4

Table 5.2: The pillar heights h_p, reconstructed cluster charge (c.c.), calculated Townsend coefficient α and calculated gain G for the four layers of SM2. The error was directly calculated for the fraction of the gain and is not shown here.

---

[1] Penning transfer not enabled

ratio	St_{In}/Eta_{In}	St_{Out}/Eta_{In}	St_{In}/Eta_{Out}	St_{Out}/Eta_{Out}	Eta_{In}/Eta_{Out}	St_{In}/St_{Out}
gain	0.811 ± 0.11	0.845 ± 0.14	0.811 ± 0.11	0.811 ± 0.14	0.97 ± 0.10	0.97 ± 0.12
c.c.	0.781±0.01	0.83±0.01	0.86±0.02	0.92±0.02	1.11±0.01	1.06±0.01

Table 5.3: The fraction of the measured pulse height and the calculated gain for the layers of SM2 at a $U_{amp} = 580$ V. The error has been determined via Gaussian error propagation.

The fraction of the cluster charge and for the gain can be compared for the individual layers of SM2. If this fraction is the same, this is likely due to the different pillar heights. For a higher amplification field correlated to a lower pillar height a higher gain is expected. Comparing the fraction of calculated gain and measured cluster charge a similar fraction is extracted for comparing Eta with Stereo layers within the uncertainties. The comparison of two Eta/Stereo layers shows a higher cluster charge for lower pillar height. As the pillar height per Stereo or per Eta layer is very close to each other, 1 μm, the pulse height is expected to be the same. This might be caused by different noise levels of the two MMFE8 board connected to the panels. The difference for the individual layers of SM2 might be due to different noise levels between the layers.

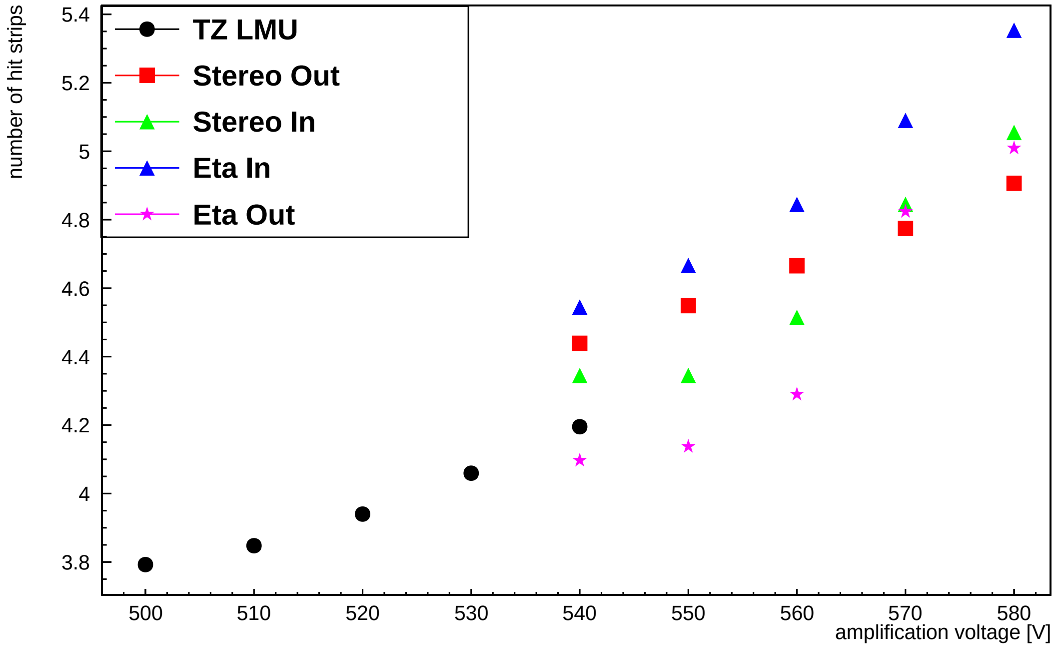

Figure 5.12: The cluster multiplicity for the 10x10 cm^2 Micromegas (TZ_{LMU}) and the layers of SM2. The number of strips for the layers of SM2 is generally higher than for the smaller Micromegas.

The number of hit strips behaves similar to the cluster charge. All of the detectors have a drift gap $d = 5$ mm and $U_{drift} = 300$ V leading to $E_{drift} = 0.6 \frac{V}{cm}$. The TZ_{LMU} has a smaller number of strips in comparison to the SM2 chamber (see fig. 5.12). The individual SM2 layers differ slightly in respect to each other by a maximum difference of 0.6 strips. For Ar:CO$_2$ 93:7 vol% on average three strips in a cluster are expected for perpendicular particle incidence relative to the anode plane. For the TZ chamber this is different by one strip or in the case of the SM2 module two more strips are generally in the cluster. The reason for this might be capacitive coupling. Capacitive coupling is slightly larger for long anode strips (for details see Lösel [2017]).

5.4.3 Comparison of Ar:CO_2 93:7 vol% and 85:15 vol% Gas Mixtures

In the following only the Eta_{In} layer of the SM2 chamber is being discussed. For Ar:CO_2 93:7 vol% data points for 550 V and 580 V are missing due to complications with the data files.

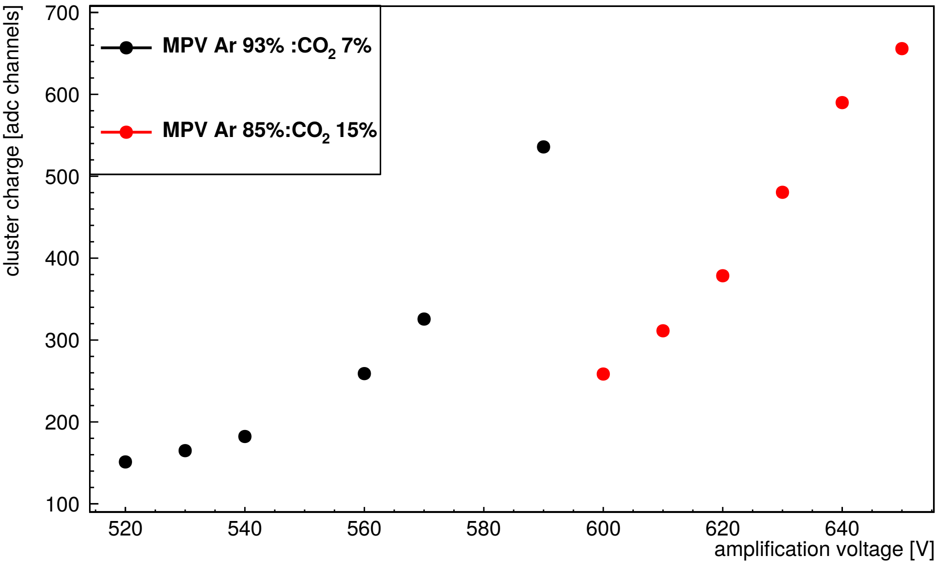

Figure 5.13: The MPV of the cluster charge for gas mixtures of Ar:CO_2 93:7 and 85:15. For a higher admixture of quencher gas, the maximum achievable cluster charge is increased by 15 %.

The MPV of the cluster charge is shown in fig. 5.13. Admixtures of 7% and 15% CO_2 are shown in the plot. For a gas with 15% CO_2 a higher maximum cluster charge is reachable with up to 15% gain in pulse height. For both gases the increase of the cluster charge is exponential.

For a higher amount of quenching gas the detector has to be operated with a higher amplification voltage because of a lower Townsend coefficient due to the higher admixture of quenching gas. Also the maximum achievable cluster charge for the detector is higher for 15 vol.% CO_2. For a maximum reachable voltage $U_{\text{amp}} = 590\,\text{V}$ for Ar:CO_2 93:7 vol.% the maximum reachable cluster charge is 590 ADC counts, whereas for Ar:CO_2 85:15 vol.% the $U_{\text{amp}} = 650\,\text{V}$ a cluster charge of 655 ADC channels could be reached.

This 10% higher gain for the gas mixture with the higher quenching fraction suggests this to be the better gas for the detector when considering the gain.

5.4.4 Comparison of different inclination angles

For the SM2 module also different inclinations (0°, 20° and 30°) with respect to the beam line were investigated (see fig. 5.14). As previously mentioned for perpendicular tracks only up to one hole (missing strip in a cluster), for an angle of 20° up to two holes and for 30° up to three holes are allowed in a cluster (see sec. 3.2).

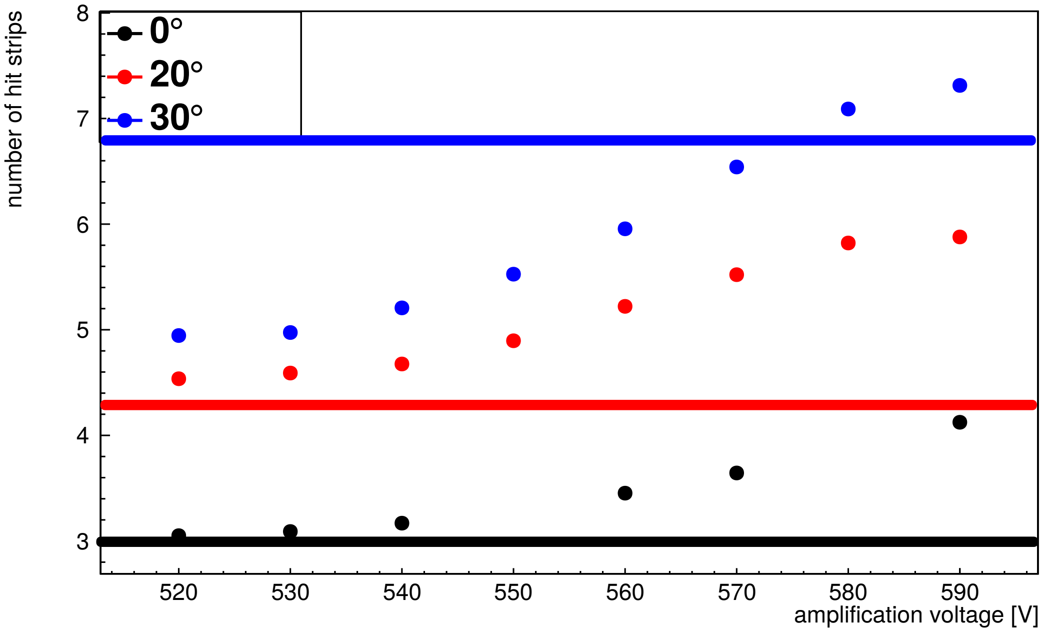

Figure 5.14: The strip multiplicity difference for angles of 0°, 20° and 30° as a function of the amplification voltage for the $\mathrm{Eta_{In}}$ layer of SM2 is shown. The strip multiplicity increases for higher angles. The expected cluster multiplicity 3 (black) at 0°, 4.3±0.4 (red) at for 20° and 6.8±0.5 at 30 ° is indicated. At higher pulse height the capacitive coupling increases.

The cluster multiplicity for different inclination angles of 0°, 20°, 30° increases in a similar manner as in fig. 5.12. The expected multiplicity n_θ is indicated for the different angles and was calculated by the following formula with the incidence angle θ, the pitch p_s and drift gap d:

$$n_\theta = \frac{d}{p_s} \cdot \tan(\theta) = \frac{5\,mm}{0.425\,mm} \cdot \tan(\theta)\,.$$

The cluster multiplicities were determined for $\theta = 20°$ as 4.3±0.4 strips and $\theta = 30°$ as 6.8±0.5 strips. For 0° and 20° the maximum number of strips and reconstructed cluster multiplicity differ by one. The case of $\theta = 0°$ follows from diffusion ($n_\theta = 3\,\text{strips/cluster}$). A higher cluster multiplicity is again reached due to capacitive coupling. This feature is less pronounced for an angle of 30°, as the amount of deposited charge decreases. Thus the borders for a cluster don't contribute as strongly of 30°.

The cluster charge as a function of the amplification voltages is shown in fig. 5.15. For every incidence angle an exponential-like increase in the cluster charge is shown. The cluster charge should increase for the different angle for the same amplification voltage, as the particle traverses a longer path and thus creats more primary electrons in the drift region.

The path length l of the particle in the detector corresponds to the deposited cluster charge $Q \sim \frac{dE}{dx}$ and to the the expected cluster multiplicity (see fig. 5.14) with a driftgap of $d = 5 \pm 0.2\,\mathrm{mm}$ and an incidence angle of $\theta_1 = (0 \pm 1)°$, $\theta_2 = (20 \pm 1)°$ and $\theta_3 = (30 \pm 1)°$

$$\cos\theta = \frac{d}{l} \Rightarrow l = \frac{5\,mm}{\cos\theta}$$

$$l_{0°} = (5.0 \pm 0.2)\,mm,\; l_{20°} = (5.32 \pm 0.31)\,mm,\; l_{30°} = 5.77 \pm 0.34\,mm\,.$$

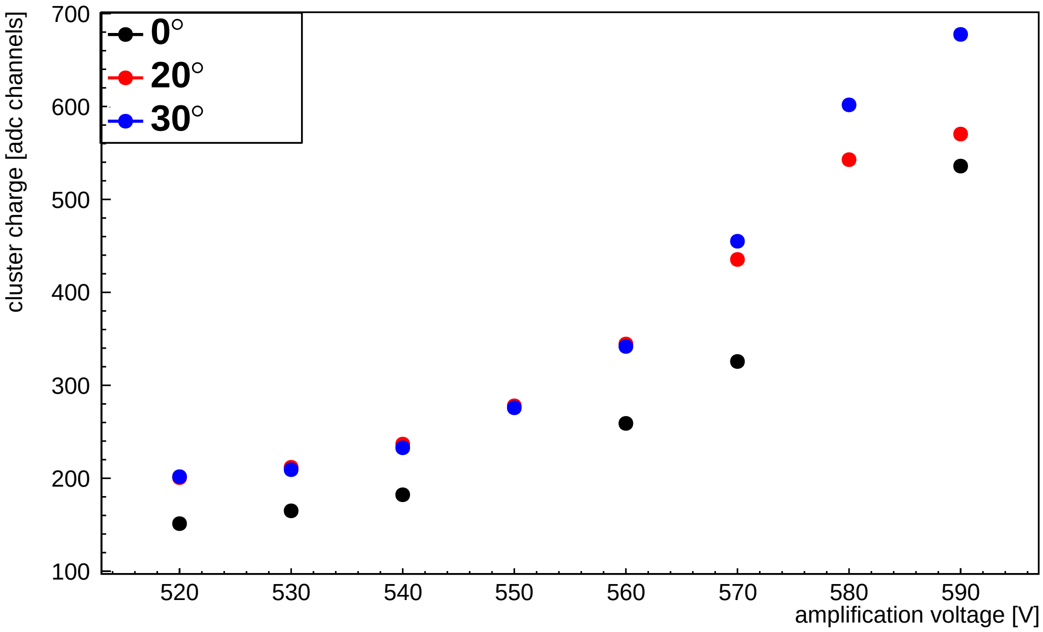

Figure 5.15: The cluster charge of different incidence angle for SM2. For 0° to 20° the difference of cluster charge is higher then for 20° to 30°.

Fraction	0°/20°	20°/30°	0°/30°
path length	0.94 ± 0.03	0.92 ± 0.03	0.87 ± 0.01
cluster charge	0.937±0.011	0.861±0.002	0.807±0.009

Table 5.4: The fraction of the path length of the particle in the drift gap and the cluster pulse height for $U_{\mathrm{amp}} = 590\,\mathrm{V}$.

The fractions for the cluster charge and path length are shown in table 5.4. The measured difference between 0° and 20° is close to the calculated theoretically calculated value. For 20° to 30° there exists a small discrepancy likely because of capacitive coupling between neighboring strips. For the comparison of 0° and 30° this discrepancy is much higher by about than for fraction of 20° and 30°. The strip charge and cluster multiplicity behave close to expectation with possible influences by the neighbor logic leading to a higher number of strips and the cluster charge being likely influenced by capacitive coupling.

5.4.5 Neighbor Logic

The neighbor logic (SNG) allows to acquire the information of strips that collect a signal below a charge threshold, but are adjacent to strips above the threshold.
The cluster multiplicity (see fig. 5.16) exhibits for both VMM settings an increase. For the working point of the deector at U_{amp}=580 V with neighbor logic activated (SNG on) 5.5 strips/cluster and for neighbor logic disabled 3.5 strips/cluster are reached, which is a difference of two strips for each settings.
For the comparison of different inclination angles of the SM2 (see sec. 5.4.4) and the test beam at the Tandem facility in Garching (see 4.2) similar discrepancies were observed in the cluster multiplicity. For both measurements the mean deviated by two strips/cluster from the theoretically calculated value.

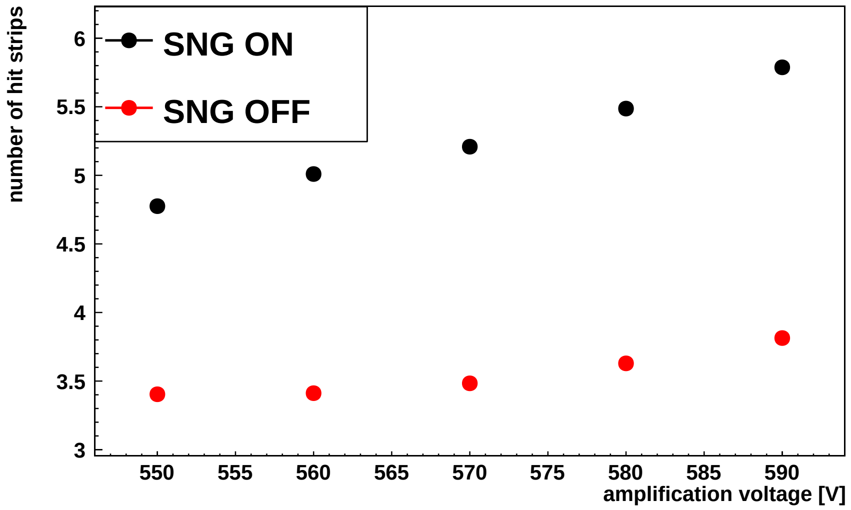

Figure 5.16: The plot shows the cluster multiplicity for neighbor logic (SNG) ON and OFF with a 0° pion measurement. At the working point of the SM2 detector $U_{\mathrm{amp}} = 580\,\mathrm{V}$ a strip difference of two strips/cluster exists.

This behavior can be explained by strips at the border of a cluster activating in total two additional strips. This leads thus to a mean increased by two strips for the cluster multiplicity.

5.4.6 Peaktime Scan

The peak time setting of the VMM defines the integration time over a detector signal. Thus it is expected that for a longer integration time the collected charge increases (see fig. 5.17). For amplification voltages below $U_{\mathrm{amp}} = 540\,\mathrm{V}$ the MPV of the cluster charge for both peak times is the same within the uncertainties.

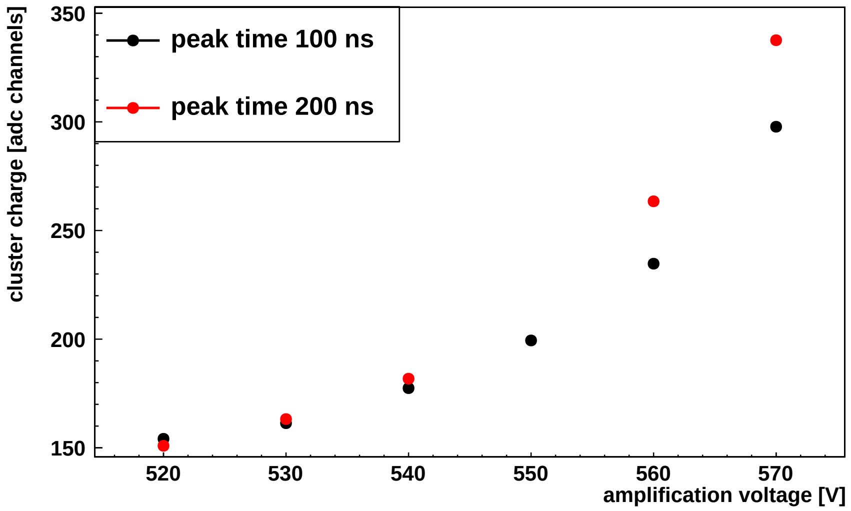

Figure 5.17: Cluster charge for different peak times. For small amplification voltages the cluster charge between the setting does not differ. For voltages above 560 V the cluster charge of peak time 200 ns surpasses the MPV of peak time 100 ns.

For the cluster multiplicity (see 5.18) also a higher cluster multiplicity is visible with the higher peak time. For a longer integration strips that were previously below the threshold reach a charge high enough to be accepted by the VMM/analysis.

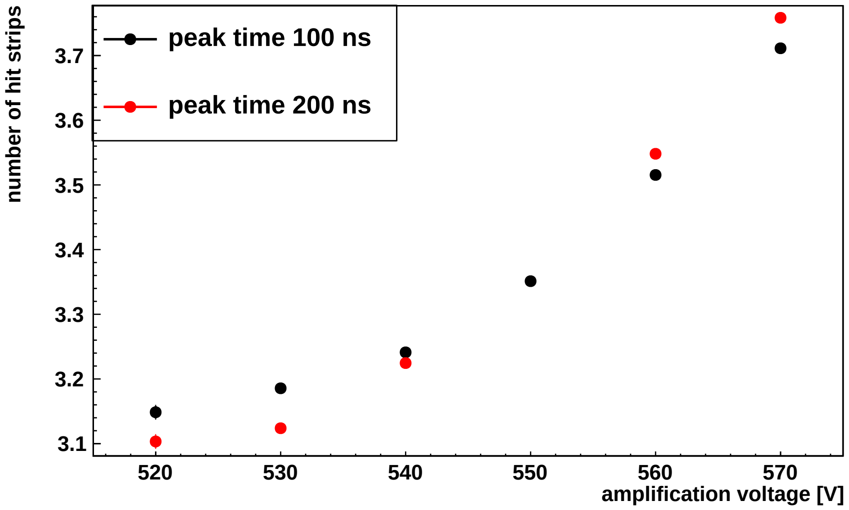

Figure 5.18: Cluster multiplicity with peak times of 100 ns and 200 ns. Only small deviations are visible.

At higher voltages the effect becomes visible, the influence of the peak time is less pronounced. Maximum differences are below 0.1 responding strips and thus neglible.

5.5 Spatial Resolution for combined APV25/VMM measurements

The spatial resolutions for the SM2 Micromegas have been determined with TMMs (APV) and TZ (VMM) tracking detectors. A hit in the non-precision coordinate was available due to a 2D readout of the TMMs. This allows for:

- a track reconstruction, which is independent of the VMM front-end electronics
- alignment along the non-precision coordinate for coordinated runs with APV25 and VMM measurements

The track acuracy of the combined measurments is Δ_{track} = (120±10)μm for the layers of SM2 and Δ_{track} = (55±10)μm for the $\mathrm{TZ_{LMU}}$, when using the spatial resolution calculated via the geometric mean method of σ_{TMM} =78μm and only using the TMM tracking detectors. The unfolded core and total spatial resolutions adjusted with the track acuracy are shown in figure 5.19 for $\mathrm{Eta_{In}}$, $\mathrm{Eta_{Out}}$, Stereo and $\mathrm{TZ_{LMU}}$.

	$\mathrm{TZ_{LMU}}$	Stereo	$\mathrm{Eta_{In}}$	$\mathrm{Eta_{Out}}$
σ_{total} [μm]	92±10	110±12	116±10	111±6
σ_{core} [μm]	59±2	60±4	85±3	68±3

Table 5.5: Core and total spatial resolution for the SM2 and $\mathrm{TZ_{LMU}}$ detectors at a amplification voltage of 560 V (or 520 V for the TZ chamber).

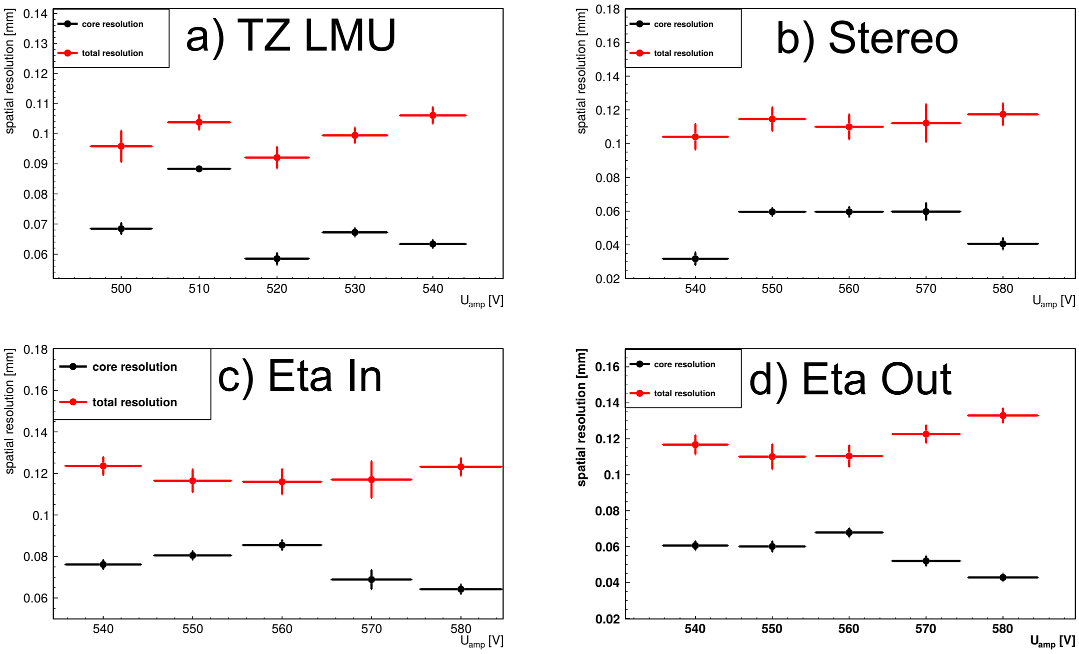

Figure 5.19: Spatial resolution as a function of the amplification voltage for core and combined Gaussian fit to the residual distribution for the small a) and large detector b)-d).

For the small detector the optimal spatial resolution is reached at 520 V, 10 V below the voltage used for tracking (see table 5.5). The spatial resolution for the TZ$_{\mathrm{LMU}}$ with U$_{\mathrm{amp}}$ = 510 V and 520 V varies to a high degree for the core spatial resolution and also the total resolution to a small degree (10μm).
This is likely due to the low amplification voltage creating a too small charge signal as well as due to the loss of events e.g. for cuts to account for the firmware by 25%. For U$_{\mathrm{amp}}$ = 510 V only 5000 entries were used for the fit leading to a jump in core Gaussian. For higher voltages than 520 V the spatial resolution stays constant within a tracking acurarcy error of 10 μm.The resolution of the indvidual SM2 layers demonstrate a similar behavior as a function of the amplification voltage. The total and core residual stays nearly constant within the error bars. The optimum residuals for the detector layers are listed in table 5.5.
For the small 10x10 cm^2 Micromegas detector a total resolution of 92 μm can be reached. For the total spatial resolution of all layers value close to 100 μm have been achieved, whereas for the intrinsic spatial resolutions values well below 100 μ were reached.
For the same measurement with muons also the coarser Stereo information was determined (see fig. 5.20), which has a resolution of σ_{SR} =(4.1±0.1) mm.
This is a similar spatial resolution as shown by Flierl [2018] with APV25 during a test beam with a weighted resolution of σ_{SR} =(3.9±0.1) mm.

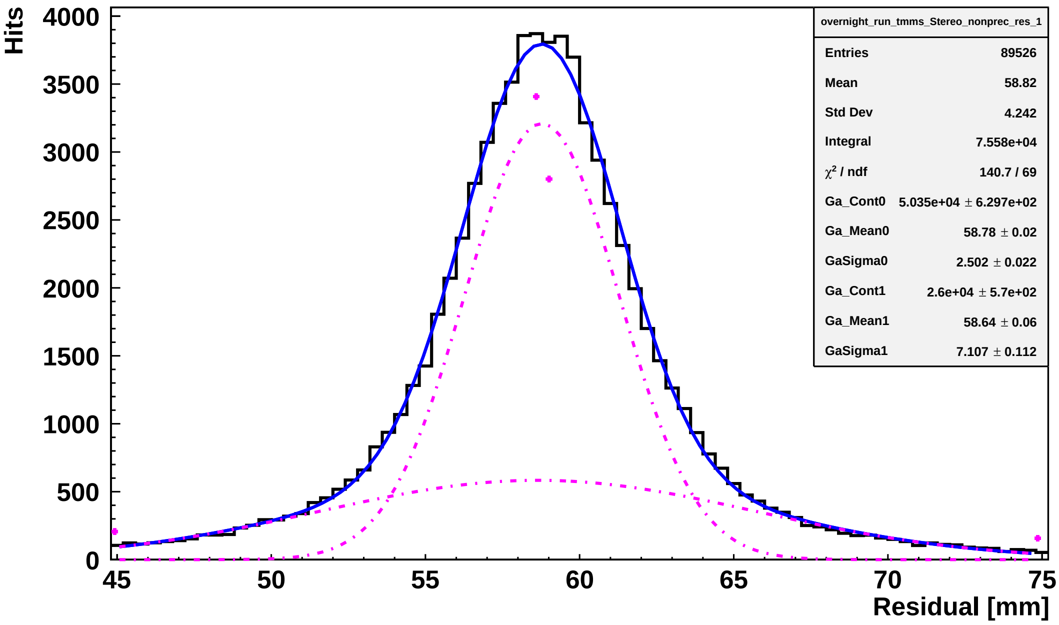

Figure 5.20: The residual for the non-precision coordinate of Stereo hast a tail residual of 7.11 mm and a core residual of 2.50 mm. This results in a spatial resolution of 4.074 mm at 590 V.

5.6 Spatial Resolution and Efficiencies with VMM Standalone Electronics

In this section the spatial resolution and 5σ efficicency is determined for the SM2 layers and for the Eta_{In} layer for different gas mixtures. The calculated spatial resolution of the VMM tracking detectors was $\sigma = 84\mu$m and lead to a track acuarcy of $\Delta_{track} = 42 \pm 2\,\mu$.

5.6.1 Discussion of all Layers

The efficiency and the spatial resolution determined for all the layers of the SM2 detectors for a perpendicular track are shown in fig. 5.21 and fig. 5.22 respectively. It is expected for each layer that the efficiency increases with the amplification voltage, as the signal height increases such that the front-end electronics can record the signals of all anode strips. It is clearly visible that the Eta layers have the highest efficiency in comparison to the combined Stereo layers. For the efficiency of the combined Stereo layer 90% can be expected using the efficiencies for $\mathrm{Stereo_{In}}$ (ϵ_{Stin}) and $\mathrm{Stereo_{Out}}$ (ϵ_{Stout}): $\epsilon_{St} = \epsilon_{Stin} \cdot \epsilon_{Stout}$=0.94·0.95=0.893. For each layer (see fig. 5.22) the change of the spatial resolution with the amplification voltage in the range of 20 μm within the error bars. For points below $\mathrm{U_{amp}} = 560\,\mathrm{V}$ the voltage is likely too low such that created signal height is also too low for the dynamic range of the front-end board. At the maximum voltage of 590 V the efficiencies for the Eta layers are around 94% (see table 5.6).

Comparing the residuals produced by APV and VMM tracker, they differ at most by 10μm. At higher voltages their is higher discrepancy between the two readout electronics e.g. at 590 V (see fig. 5.19).

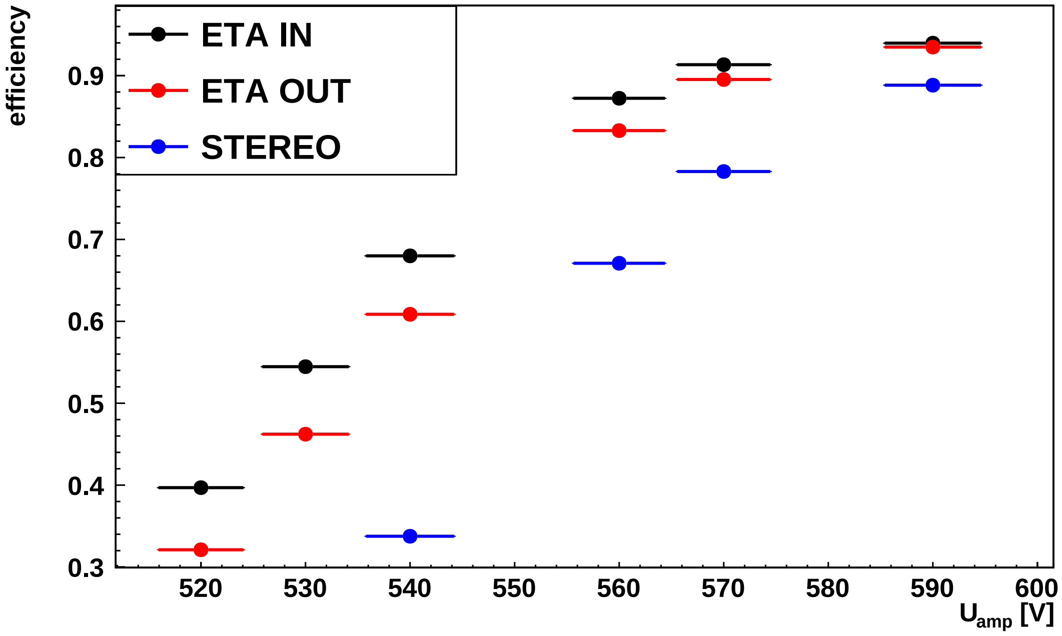

Figure 5.21: Efficiency plot for the layers of SM2 during a pion run. The Stereo layers are significantly lower than both Eta layers because of the combination of individual layers.

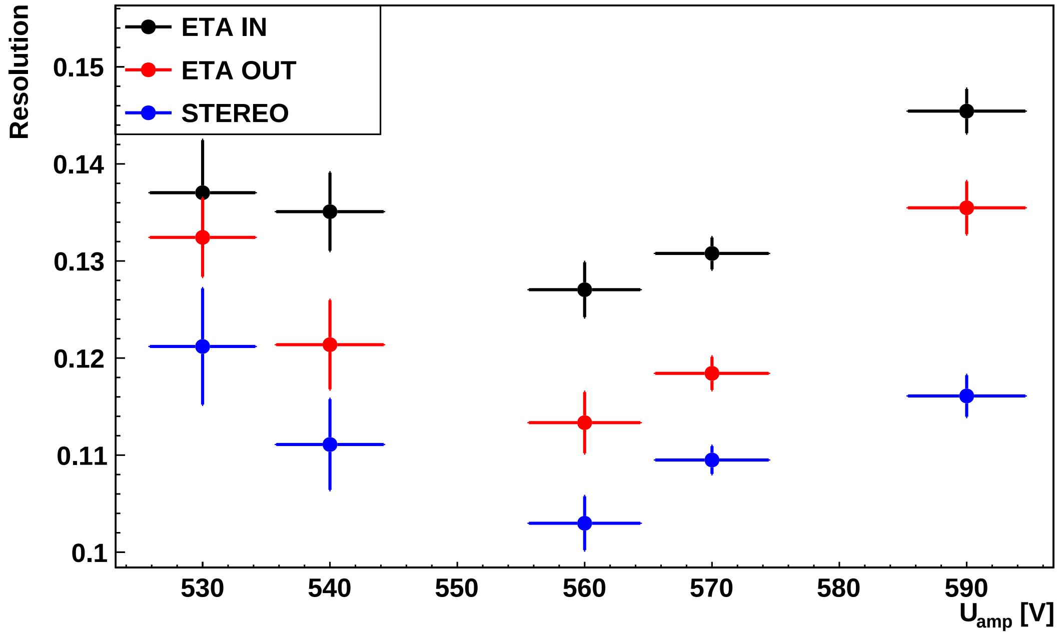

Figure 5.22: The resolution of the Stereo layer is better, due to the combination of two position informations.

	SR (590 V) [μm]	ϵ (590 V) [%]	VMM SR (560 V) [μm]	APV SR (560 V) [μm]
Stereo	116±2	89.4±0.2	103±2	110±12
$\mathrm{Eta_{Out}}$	135±3	93.5±0.1	114±3	(111±6)
$\mathrm{Eta_{In}}$	146±2	94.2±0.1	127±2	(116±10)

Table 5.6: Spatial resolution (SR) and efficiencies (ϵ) of all SM2 layers are listed for an amplification voltage of 560 V and a comparison of APV and VMM residuals for 560 V at the lowest resolution.

5.6.2 Different Ar:CO_2 Gas Mixtures

For the gas tests also efficiencies and spatial resolutions have been determined with the SM2 detector. The gases Ar:CO_2 93:7, 85:15, 70:30 (vol%) were tested for perpendicular incidence. As shown in fig. 5.13 the maximally reachable gain and amplification voltages increase with a higher fraction of quenching gas.

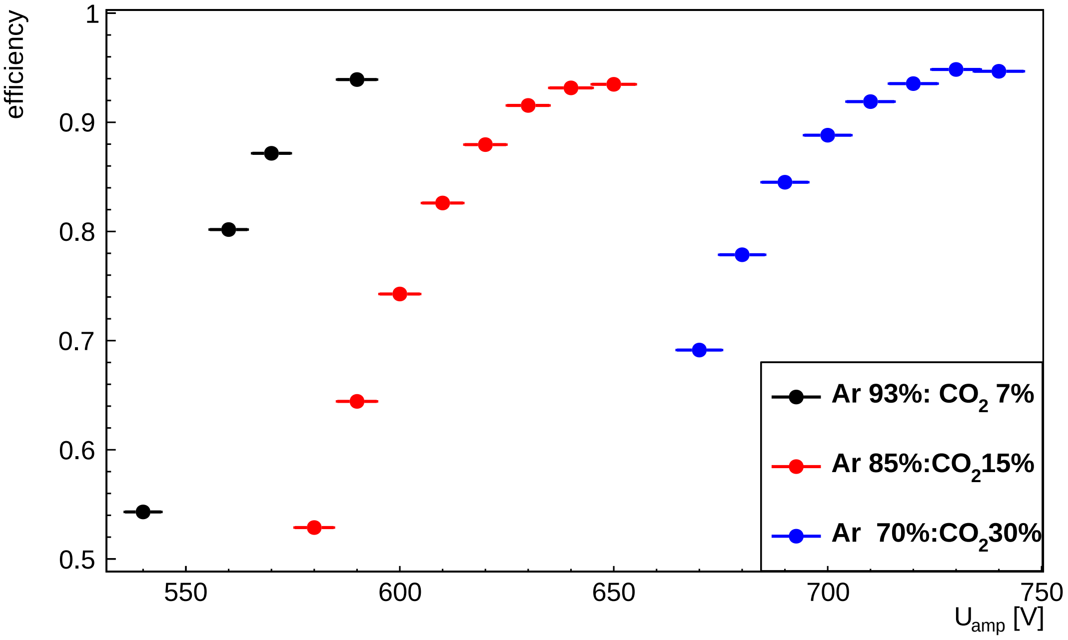

Figure 5.23: Efficiency of $\mathrm{Eta_{In}}$ as a function of U_{amp} for the three different gas mixtures. All of the gas mixtures exhibit a similar trend along increasing amplification voltage.

Ar:CO_2 [vol%]	max. amp. voltage [V]	efficiencies [%]	SR [μm]	ph. [ADC ch.]
93:7	590	93.9±0.1	125±3	515
85:15	650	93.5±0.1	116±2	620
70:30	730	94.7±0.1	134±3	605

Table 5.7: Table for the maximum reachable amplifcation voltage, the spatial resolution (SR), efficiency and maximum pulse height (ph) of different gas mixtures.

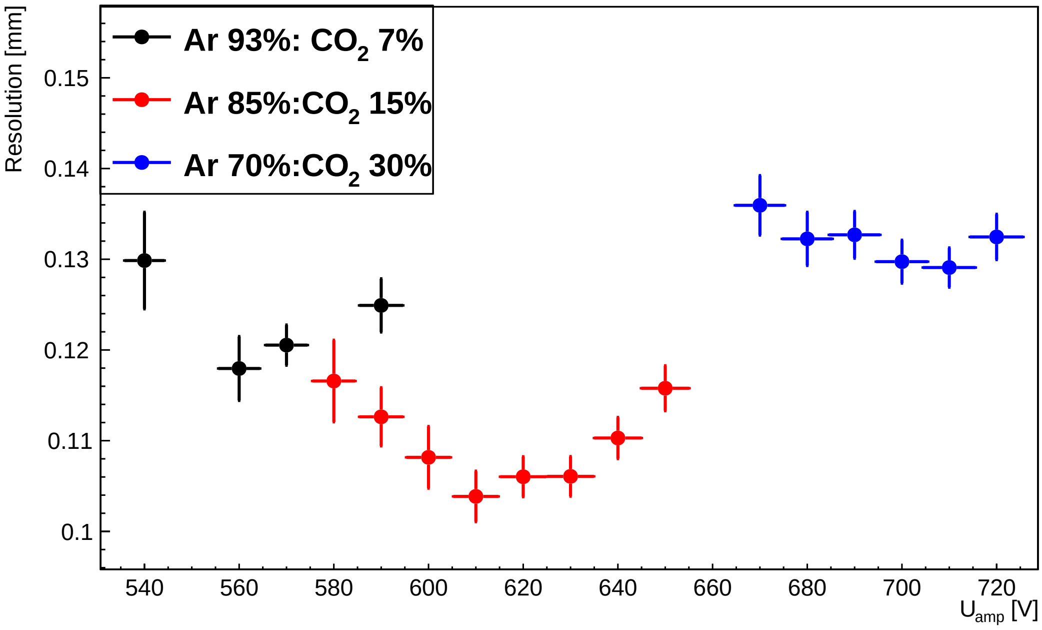

Figure 5.24: The spatial resolution as a function of the amplification voltage for different Ar:CO_2 mixtures for the Eta_{In} layer of SM2. For Ar:CO_2 85:15 vol.% the best spatial resolution of all mixtures is achieved.

For the different gas mixtures the best spatial resolutions scatter in a margin within 25 μm (see fig. 5.24). Ar:CO_2 85:15 vol% shows the best resolution for $U_{\text{amp}} = 610$ V, well below the maximum achievable voltage of 650 V. At 630 V efficiencies above 90% are achievable. For Ar:CO_2 93:7 efficiencies above 90 % seem possible only for the highest achievable voltage with slightly reduced spatial resolution. For 70:30 vol% the efficiency peaks at 730 V, the spatial resolution gets best at 710 V.

In all three cases, the spatial resolution degrades for the best efficiency, probably due to saturation of the charge pulses at the highest amplification voltages. Ar:CO_2 vol% seems to be the best detector gas for the SM2 Micromegas, as efficiency and spatial resolution at 630 V are both good and as the maximum reachable voltage is well above this value, in contradiction to Ar:CO_2 93:7 vol%. For the 70:30 vol% gas mixture the high drift voltages are not supported by the HV-feedthrough.

5.6.3 μTPC Residuals at an Angle of 30°

As the SM2 detector will detect mostly particles at angles $\theta > 20°$ when integrated in the New Small Wheels, the spatial resolution for inclined tracks is of interest. However, a high signal loss and a non-ideal time calibration was present because of the use of the non-final front-end electronics [Koulouris, 2019]. For this reason the inclined cases with centroid and μTPC are only briefly discussed.

As stated in section 3.4, the centroid method gets worse for inclined angles due to non-homogenous charge disposition. For Ar:CO_2 70:30 vol% the core resolution predicted was $\sigma_{SR} = 109\,\mu$m at 0° and $\sigma_{SR} = 360\,\mu$m at 30° (see fig. 5.25).

An exemplarily μTPC residual is shown in fig. 5.26 for a gas mixture of Ar:CO_2 70:30 vol% mentioned the residual width is large in comparison to the 0° case, as expected. The instrinsic

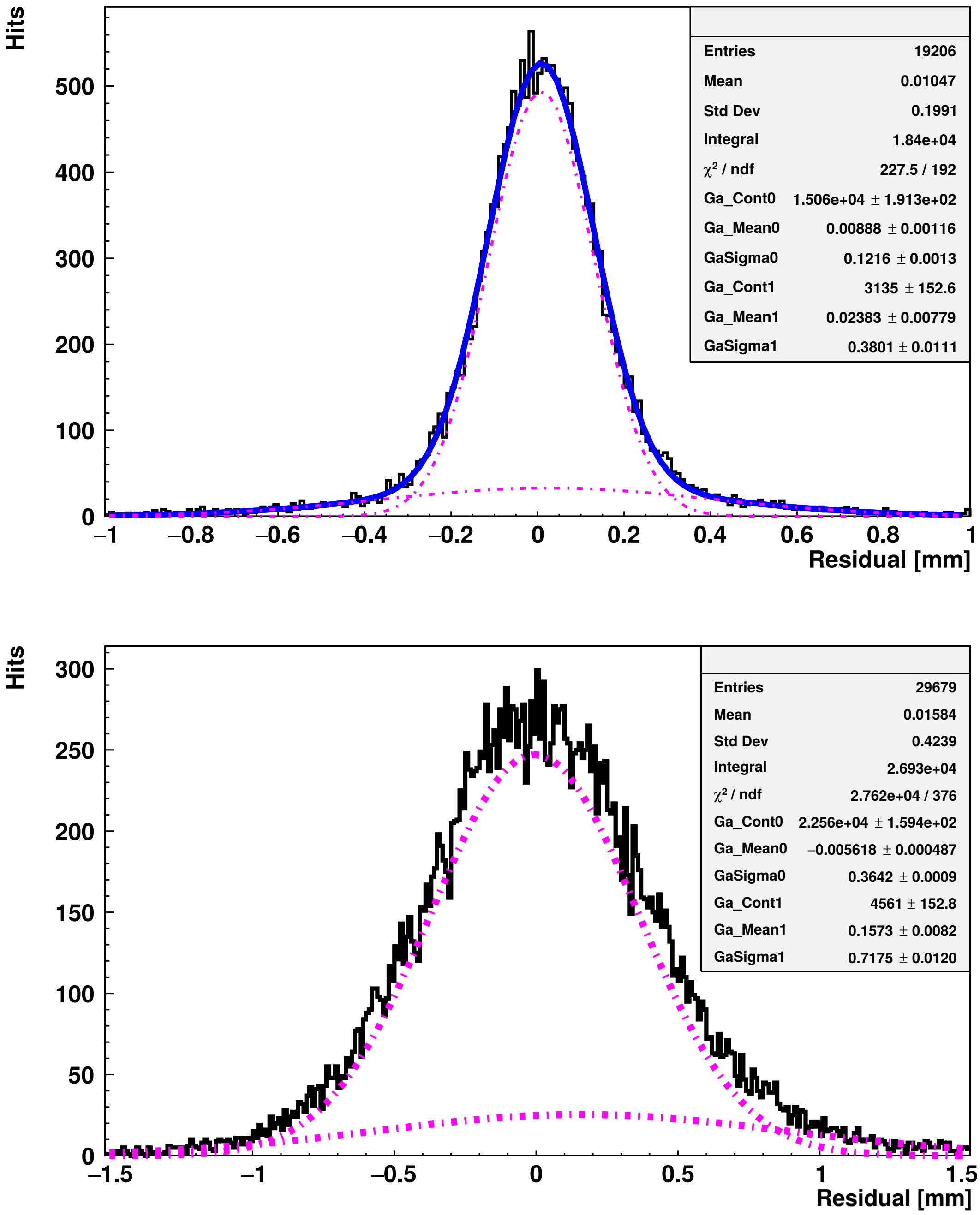

Figure 5.25: The intrinsic centroid spatial resolutions for 0° (top) $\sigma_{core} = 109\,\mu$m and 30° $\sigma_{SR} = 360\,\mu$m (below) for the Eta_{Out} layer for Ar:CO_2 70:30 vol% at $U_{\text{amp}} = 740$ V and $U_{\text{drift}} = 700$ V.

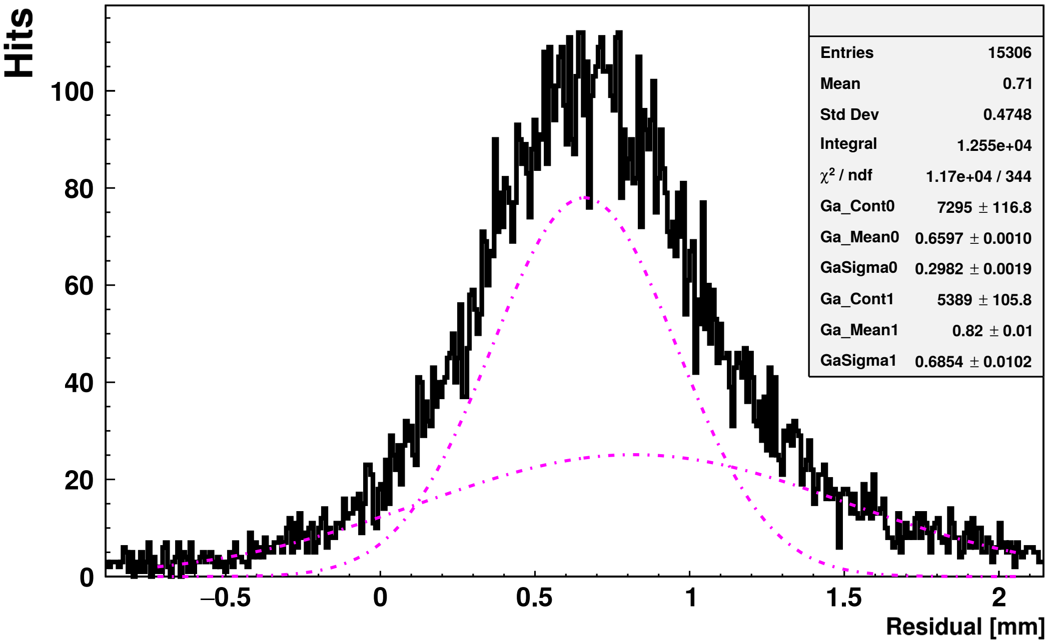

Figure 5.26: Work in progress μTPC residual for $\mathrm{Eta}_{\mathrm{Out}}$ with a core width of $\sigma_{\mu TPC} = 293\,\mu$m for Ar:CO$_2$ 70:30 vol% at $U_{\mathrm{amp}} = 740$ V and $U_{\mathrm{drift}} = 700$ V.

resolution for the μTPC approach is better, however, the fraction of events of the core and tail Gaussian are nearly th same compared to the centroid residuals. Here still corrections are necessary e.g. implementation of a Hough transformation. As mentioned previously, also the non-ideal time calibration i.e. non-final readout electronics contributed to this.

5.7 Summary

The VMM has been tested sucessfully with a 2 m^2 Micromegas detector for perpendicular tracks reproducing spatial resolutions on the order of 100μm and 94% efficiency at 590 V. For 570 V these efficiencies were even above 95 % for Ar:CO$_2$ 93:7 vol% with a different analysis [Koulouris, 2019].

The combined VMM/APV readout show that the spatial resolution is also in a similar range to the VMM only readout.

The cluster charge distribution for each layer compared to each other show dependencies related to the pillar height differences of the PCBs.

Also interesting is that for a higher admixture of quenching gas a higher gain can be reached. From a stand point of the pulse height Ar:CO$_2$ 85:15 vol% is a better detector gas. The quencher of the gases lead to a higher achievable gain of 10%. The cluster multiplicity for the measurments was always increased in comparison to the theoretical value. The neighbor logic feature can be likely attributed to this.

The different gas mixtures, different inclination angles and settings for the VMM show differences in the cluster charge and strip multiplicity mostly as expected.

The spatial resolution for inclined tracks needs to be still improved, both from the analysis as well as from the electronics point of view [Koulouris, 2019].

Chapter 6

Summary and Outlook

In this thesis the new VMM front-end chip for Micromegas detectors of the New Small Wheel (NSW) was tested in two experiments.
At the H8 beamline at SPS/CERN the VMM electronics was tested successfully for the first time together with a full size Micromegas series chamber for the ATLAS New Small Wheel, the first German SM2 module. Spatial resolutions below 100 μm and efficiencies above 90 % were observed with perpendicular beams of 20-150 GeV muons or pions.
At the Tandem accelerator facility in Garching the operational principle of the VMM readout chain and data aquisition was investigated using 22 MeV protons. A VMM front-end board was studied which was attached to a 10x10 cm^2 Micromegas prototype using a gas mixture of Ar:CO_2 93:7 vol% varying either the drift voltage $\mathrm{U}_{\mathrm{drift}}$ for fixed $\mathrm{U}_{\mathrm{amp}} = 480\,\mathrm{V}$ or the amplification voltage $\mathrm{U}_{\mathrm{amp}}$ for fixed $\mathrm{U}_{\mathrm{drift}} = 250\,\mathrm{V}$.
The most probable value of the cluster charge distribution as a function of the amplification voltage exhibited an exponential growth following the Townsend avalanche formalism. The measured cluster multiplicity of 7 strips for $\mathrm{U}_{\mathrm{amp}} = 480\,\mathrm{V}$ is by two strips higher than the theoretically expected 5 strips. This can be attributed to the neighbor logic feature of the VMM chip activating also channels below the configured charge threshold at the borders of an ionization cluster.
The inclination angle of the detector was reconstructed using the μTPC method. The angular resolution for varying drift field was $(^{+6^\circ}_{-4^\circ})$. A comparison of these results to similar measurements recorded independently with the APV25 readout gives $(^{+4^\circ}_{-2^\circ})$. The slightly worse results for the VMM electronics are probably due to a non-optimal time calibration.

First measurements of the μTPC position resolution at the SPS/CERN test beam with 20-150 GeV muons/pions at inclined tracks of 30° gave results well below the spatial resolution measured by the centroid method, where the position of the ionizing particle is determined by the charge average over the responding strips in an ionization cluster. The effect is clearly visible, but still less pronounced than expected. We expect optimized noise conditions (grounding) and optimized final electronics to improve this in future.
The performance of the NSW Micromegas basically followed the expected correlation between the cluster charge and the pillar height. The Eta panels have systematically about 5 μm lower pillar height than the Stereo panels. Accordingly the pulse height at the Eta panels is by 90 ADC channels lower.
The studies for different Ar:CO_2 gas mixtures showed that for 85:15 vol% a $\sim$10% higher gain can be reached as for 93:7 vol%, the standard mixture. Ar:CO_2 85:15 vol% shows the best spatial resolution of $(116 \pm 2)\mu$m.

The detection efficiencies were similar for all investigated Ar:CO_2 gas mixtures. But efficiencies above 90% are easier reachable for 85:15 vol% than for 93:7 vol%. At 93:7 vol% sufficiently high efficiencies are only reachable at voltages close to the break through point of the detector. 85:15 vol% allows here for a margin of 20-30 V between working point and maximum possible voltage. An Ar:CO_2 gas mixture of 70:30 vol% is not usable for our ATLAS micromegas for technical reasons, as the HV feedthrough for a drift cathode can not withstand voltages above 600 V.
Different peaking times of 100 ns and 200 ns show, as expected, changes in the cluster charge and cluster multiplicity distribution. For 200 ns, the result was an increased cluster charge of about 10% due to the longer integration time over the signal. The cluster multiplicity becomes minimally larger for a longer peak time because strips with signals below threshold at 100 ns collect now enough charge to be registered by the VMM chip.

The spatial resolutions and efficiencies for perpendicularly incident muons or pions showed a satisfying result for all layers of SM2:

(135±3) μm at (93.5±0.1)% for the Eta_{Out} layer,
(146±2) μm at (94.2±0.1)% for the Eta_{In} and
(116±2) μm at (89.4±0.2)% for the combined Stereo coordinates.

The lower efficiency for the combined stereo layer is understood and results from the combined efficiencies of $\text{Stereo}_{\text{In}}$ and $\text{Stereo}_{\text{Out}}$s $\epsilon_{Stin} \cdot \epsilon_{Stout} = 0.94 \cdot 0.95 = 0.893$.
Detector resolutions using the old APV25 electronics were for the detectors under test:

$(111 \pm 6)\mu$m for the Eta_{Out} layer,
$(127 \pm 2)\mu$m for the Eta_{In} and
$(110 \pm 12)\mu$m for the combined Stereo coordinates.

The non-precison coordinate exhibited a spatial resolution of $\sigma_{SR} = 4.2\,\text{mm}$, being close to the requirements of the ATLAS New Small Wheel.

The VMM3 front-end readout chip is a promising ASIC for the New Small Wheel. Meanwhile the VMM has also been implemented into the SRS readout package and is thus available for a broader field of applications. Due to zero-suppression and digitization on the chip, it is well suited for the readout of detectors in high rate enviroments or in high rate applications outside of particle physics, e.g. in medical imaging applications.

Appendix A

List of Abbreviations

APV25	Analog Pipeline Voltage readout chip
ADC	Analog-to-Digital Converter
ASIC	Application-Specific Integrated Circuit
BCID	bunch crossing clock counter
CKBC	bunch crossing clock
CTF	Clock and Trigger generator and Fan-out
DAC	Digital-to-Amplitude Converter
FEC	Front End Concentrator cards
FPGA	Field Programmable Gate Array
LHC	Large Hadron Collider
sTGC	small-strip Thin Gap Chambers
Micromegas	Micro Mesh Gaseous Structure Detectors
MDT	Monitored Drift Tube
MMFE8	Micromegas Front-end Board
NSW	New Small Wheel
PCB	Printed Circuit Board
PDO	Peak Detector Output
SAS	a serial point-to-point connection
SM2	$2\,\mathrm{m}^2$ New Small Wheel Micromegas Module
SRS	Scalable Readout System
TAC	Time-to-Analog Converter
TDO	Time Detector Output
VMM	New Small Wheel front-end readout chip

Bibliography

[Adloff et al.(2009)] C. Adloff et al. *MICROMEGAS chambers for hadronic calorimetry at a future linear collider*. JINST, 4:P11023, 2009. doi:10.1088/1748-0221/4/11/P11023.

[Alexopoulos et al.(2011)] T. Alexopoulos, J. Burnens, R. de Oliveira, G. Glonti, O. Pizzirusso, V. Polychronakos, G. Sekhniaidze, G. Tsipolitis, and J. Wotschack. *A spark-resistant bulk-micromegas chamber for high-rate applications*. Nuclear Instruments and Methods in Physics Research Section A: Accelerators, Spectrometers, Detectors and Associated Equipment, 640(1):110 – 118, 2011. ISSN 0168-9002. doi:https://doi.org/10.1016/j.nima.2011.03.025. URL `http://www.sciencedirect.com/science/article/pii/S0168900211005869`.

[ATLAS Collaboration(2008)] ATLAS Collaboration. *The ATLAS Experiment at the CERN Large Hardron Collider*. JINST, 3, 2008.

[ATLAS collaboration(2013)] ATLAS collaboration. *New Small Wheel Technical Design Report*. Technical Report CERN-LHCC-2013-006. ATLAS-TDR-020. ATLAS New Small Wheel Technical Design Report, 2013.

[Bortfeldt(2014)] J. Bortfeldt. *Development of Micro-Pattern Gaseous Detectors - Micromegas*. PhD thesis, Ludwig-Maximilians-Universität München, 2014.

[Carnegie et al.(2005)] R.K. Carnegie, M.S. Dixit, J Dubeau, D. Karlen, J.-P Martin, H. Mes, and K. Sachs. *Resolution studies of cosmic-ray tracks in a TPC with GEM readout*. Nucl. Instrum. Methods Phys. Res., A, 2005.

[CERN(2019)] CERN. *The Super Proton Synchrotron*. Accessed on 7.05.2019, April 2019. URL `https://home.cern/science/accelerators/super-proton-synchrotron`.

[CERN website(2016)] CERN website. *The HL-LHC Project*, 2016. URL `http://hilumilhc.web.cern.ch/about/hl-lhc-project`. Accessed on 7.05.2019.

[De Geronimo et al.(2017)] G. De Geronimo, G. Iakovidis, V Polychronakos, S. Martoiu, and W. Ding. *Test Status of VMM3*. Presentation, April 2017. URL `https://indico.cern.ch/event/631131/contributions/2561765/attachments/1450861/2237123/VMM_Update_Apr_2017_fin.pdf`.

[Flierl(2018)] B.F. Flierl. *Particle Tracking with Micro-Pattern Gaseous Detectors*. PhD thesis, Ludwig-Maximilians-Universität München, 2018.

[Giomataris et al.(1996)] Y. Giomataris, P. Rebourgeard, J. Robert, and G. Charpak. *MICROMEGAS: a high-granularity position-sensitive gaseous detector for high particle-flux environments*. Nuclear Instruments and Methods in Physics Research, Section A , 376:29–35, 1996.

[Grupen and Shwartz(2008)] Claus Grupen and Boris Shwartz. *Particle Detectors.* Cambridge Monographs on Particle Physics, Nuclear Physics and Cosmology. Cambridge University Press, 2 edition, 2008. doi:10.1017/CBO9780511534966.

[Halkiadakis(2011)] Eva Halkiadakis. *Introduction to the LHC Experiments.* In *Physics of the large and the small, TASI 09, proceedings of the Theoretical Advanced Study Institute in Elementary Particle Physics, Boulder, Colorado, USA, 1-26 June 2009*, pages 489–518, 2011. doi:10.1142/9789814327183_0009.

[Herrmann(2016)] M. Herrmann. *Methods and Techniques for Construction of large area Micromegas.* Master's thesis, Ludwig-Maximilians-Universitaet Muenchen, 2016.

[Horvat(2005)] S. Horvat. *Study of the Higgs Discovery Potential in the Process* $pp \rightarrow H \rightarrow 4\mu$. PhD thesis, University of Zagreb, 2005.

[Iakovidis(2014)] G. Iakovidis. *Research and Development in Micromegas Detector for the ATLAS Upgrade.* PhD thesis, National Technical University of Athens, 2014.

[Iakovidis(2017)] G. Iakovidis. *VMM 3 Test beam VMM3a Status.* In *RD51 - MiniWeek*, 2017.

[Iakovidis et al.(2015)] Georgios Iakovidis, Venetios Polychronakos, and Gianluigi De Geronimo. *VMM - An ASIC for micropattern detectors.* Technical Report ATL-MUON-PROC-2015-015, CERN, Geneva, Nov 2015. URL `https://cds.cern.ch/record/2104297`.

[Jones et al.(1999)] L.L. Jones, M.J. French, Q. Morrissey, A. Neviani, M. Raymond, G. Hall, P. Moreira, and P. Cervelli. *The APV25 Deep Submicron Readout Chip for CMS Detectors.* 1999. doi:10.5170/CERN-1999-009.162.

[Kleinknecht(1992)] K. Kleinknecht. *Detektoren fuer Teilchenstrahlung: mit 20 Tabellen.* Teubner-Studienbücher : Physik, 1992.

[Klitzner(2016)] F. Klitzner. *Studies of Floating Strip Micromegas Detectors in Proton and Carbon Ion Beams with a Fast Gas Mixture.* Master's thesis, Ludwig-Maximilians-Universitaet Muenchen, 2016.

[Klitzner(2019)] F. Klitzner. *Development of Novel Two-Dimensional Floating Strip Micromegas Detectors with an In-depth Insight into the Strip Signal Formation.* PhD thesis, Ludwig-Maximilians-Universität München, 2019. Submitted 18.4.2019.

[Koulouris(2019)] Aimilianos Koulouris. *First Production Modules of the ATLAS Micromegas and Performance Studies.* Technical Report ATL-MUON-PROC-2019-001, CERN, Geneva, Mar 2019. URL `https://cds.cern.ch/record/2669445`.

[Lösel(2017)] P. Lösel. *Precision Calibration of Large Area Micro Pattern Gaseous Detectors.* PhD thesis, Ludwig-Maximilians-Universität München, 2017.

[Lösel and Müller(2015)] P. Lösel and R. Müller. *Design and Construction of Large Size Micromegas Chambers for the Upgrade of the ATLAS Muon Spectrometer.* Online, 2015.

[Lupberger et al.(2018)] M Lupberger, L Bartels, F M Brunbauer, M Guth, S Martoiu, H Müller, E Oliveri, D Pfeiffer, L Ropelewski, A Rusu, and P Thuiner. *Implementation of the VMM ASIC in the Scalable Readout System.* Nucl. Instrum. Methods Phys. Res., A, 903:91–98. 8 p, 2018. URL `https://cds.cern.ch/record/2630908`.

[M. Tanabashi et al. (Particle Data Group)(2018)] M. Tanabashi et al. (Particle Data Group). *Review of Particle Physics.* Phys. Rev. D 98, 010001, 2018.

[Nygren(1974)] D.R. Nygren. *The Time-Projection Chamber - A new 4π detector for charged particles*. PEP-144, 1974.

[Polychronakos et al.(2017)] V. Polychronakos, G. Iakovidis, and G. De Geronimo. *ATLAS NSW Electronics Specifications Component: VMM*. Technical report, ATLAS Collaboration, 2017.

[Raether(1964)] H. Raether. *Electron Avalanches and Breakdown in Gases*. Butterworths advanced physics series, 1964.

[Sauli(1997)] F. Sauli. *GEM: A new concept for electron amplification in gas detectors*. Nuclear Instruments and Methods in Physics Research Section A: Accelerators, Spectrometers, Detectors and Associated Equipment, 386(2):531 – 534, 1997. ISSN 0168-9002. doi:https://doi.org/10.1016/S0168-9002(96)01172-2. URL `http://www.sciencedirect.com/science/article/pii/S0168900296011722`.

[Scholer(2018)] P. Scholer. *Private Communication*. 2018.

[Sekhniaidze(2017)] G. Sekhniaidze. *New CTF clock/trigger splitter for SRS*. Presentation, 2017. URL `https://indico.cern.ch/event/676702/contributions/2818995/attachments/1575408/2487615/CTGF.pdf`.

[Townsend(1910)] T.S. Townsend. *The Theory of Ionization of Gases By Collision*. Constable & Company Ltd, 1910.

[Zibell(2014)] A. Zibell. *High-Rate Irradiation of 15mm Muon Drift Tubes and Development of an ATLAS Compatible Readout Driver for Micromegas Detectors*. PhD thesis, Ludwig-Maximilians-Universität München, 2014. URL `https://www.etp.physik.uni-muenchen.de/publications/theses/download/phd_azibell.pdf`.

Acknowledgments

I would like to thank...

- ... Prof. Dr. Otmar Biebel for the opportunity to write my master thesis in the detector physics group about such an exciting electronics and detector physics topic.

- ... Dr. Ralf Hertenberger for the input and valuable discussions during my thesis, which always helped me to comprehend the underlying physics better as well as for his help during the setup at the Tandem test beam.

- ... my supervisor Felix Klitzner, who always had time for my many questions in regards to physics, as well for his support during the test bea,s at Garching and at the SPS, his support with the analysis of the beam time at SPS as well as for being a great office mate.

- ... Patrick Scholer for the support with the calibration routine of the VMM chip.

- ... Prof. Dr. Theodoros Alexopoulos and the test beam team at the SPS in June 2018 for the input about the data acquisition routine with the VMM and the possibility to analyze the beam time data.

- ... the other members of our group Dr. Bernhard Flierl, Christoph Jagfeld, Dr. Chrystomos Valderanis, Maximilian Herrmann, Dr. Philipp Lösel and Dr. Ralph Müller for valuable discussions and a generally nice working environment.

And of course I want to thank my family and friends for there never ending support!

Declaration of academic integrity

Untersuchungen des VMM Auslesechips für Micromegas Detektoren des ATLAS New Small Wheel Upgrades

selbständig verfasst zu haben und keine anderen als die angegebenen Quellen und Hilfsmittel verwendet zu haben.

Maximilian Paul Rinnagel

Munich, April 16, 2019